Altering the wetting properties of FEP films by nano-structuring the surface using reactive ion etching

Nikolai Frøvik

Master's Thesis in Measurement Science

Supervisor: Professor Dr. Lars Egil Helseth
Co-supervisor: Dr. Martin Møller Greve

Department of Physics and Technology
University of Bergen

October 2017

Abstract

Renewable energy sources has become a large field of research, and in the recent years, methods to harvest energy from rain drops have been developed. This technology is based on rain drops rolling or sliding on a polymer surface. Thus, the behavior of drops on such polymer surfaces are of interest. In this thesis work, the surface of fluorinated ethylene propylene (FEP) has been modified by creating nano-structures using reactive ion etching (RIE). Different etch parameters resulted in nano-structures with shapes like granules, hairs and holes. The granules and hairs had a diameter of approximately 100 nm, and the tallest hairs were about 500 - 600 nm tall. The highest measured aspect ratio of hairlike structures were about 5 (height/width).

In order to accurately measure the wetting properties of the nano-structured FEP, a suitable measurement method had to be chosen and optimized. Experiments with a tilted plate enabled reproducible results for the nano-structured FEP of advancing contact angle (ACA), receding contact angle (RCA) and the roll off angle (ROA), i.e. when the drop starts to roll or slide off the sample. By the ROA, the adhesive force between the drop and the surface of the sample could be calculated. An alternative method to estimate the adhesive force using measurements of ACA and RCA has been found to give comparable results to the method using the ROA. Generation of nano-structures altered the wetting properties of FEP significantly. The ACA increased from $118 \pm 2\ ^\circ$ to $144 \pm 5^\circ$ at the most, and the RCA decreased from $102 \pm 2^\circ$ to about 20° for FEP treated by different RIE processes. Drop-surface adhesion increased from 110 ± 10 μN for untreated FEP, to 620 ± 30 μN at most for hairlike nano-structures.

Acknowledgements

First, I would like to express my sincere gratitude to my supervisors, Professor Dr. Lars Egil Helseth and Dr. Martin Møller Greve. Their guidance and support has been invaluable throughout the course of this thesis project. Thanks for all the inspiring discussions and helpful feedback. I also want to thank my fellow students for much fun and valuable discussions.

In addition, I want to thank my family and friends for supporting me and cheering on me. A special thanks goes to my beloved wife Maren, for your continuous support and for always believing in me. Last, I want to thank my daughter Johanne, for always brightening my day and giving me so much joy!

Contents

List of Figures

List of Tables

List of Abbreviations

CA	**C**ontact **A**ngle
ACA	**A**dvancing **C**ontact **A**ngle
RCA	**R**eceding **C**ontact **A**ngle
ARCA	**A**dvancing and **R**eceding **C**ontact **A**ngle
CAH	**C**ontact **A**ngle **H**ysteresis
DBD	**D**rop **B**ase **D**iameter
DI	**De**ionized
ROA	**R**oll **O**ff **A**ngle
px	**Pix**el
RIE	**R**eactive **I**on **E**tcher
SEM	**S**canning **E**lectron **M**icroscope
FEP	**F**luorinated **E**thylene **P**ropylene

Chapter 1

Introduction

1.1 Background

In the recent years, research on different methods for harvesting energy from rain drops have been conducted. Two categories of methods are those based on the piezoelectric effect [1], and another category are those based on triboelectric charging [2]. The methods of harvesting energy by piezoelectric or triboelectric transducers do not require large investments and big available areas like conventional hydropower requiring large and expensive facilities like reservoirs and turbines [3]. Thus, energy harvesting from rain drops could become a favorable source of energy in remote areas, especially on the northern and southern hemisphere with little or no sunlight during winter [4].

Piezoelectric materials are known to set up an electric field when exposed to mechanical stress. Thus, if a piezoelectric material is attached to a flexible cantilever, bending of the cantilever results in squeezing or stretching of the piezoelectric material, which induces an electric field. This can be set up in a way that falling rain drops may hit the flexible cantilever. In the impact from the drops, mechanical energy is transferred to the cantilever, making the cantilever and the piezoelectric material to be bent. Ref. [1] is an example of harvesting energy by means of piezoelectric transducers.

The other method utilizes triboelectric charging. When dissimilar materials get into physical contact, charge of opposite polarity develops in the two materials, which is known as triboelectric charging. The magnitude of the developed charge, depends on the environmental conditions, the process of contact, and the two materials in contact. A material's order in the triboelectric series gives information about the relative polarity developed when contacted by another material [5]. The phenomenon of triboelectric charging has been utilized to harvest energy from droplets coming in contact with polymers [2, 6, 7]. When water drops come in contact with a fluoropolymer like PTFE or FEP, a negative charge develops on the polymer surface. By placing a metal electrode on the back side of the polymer, the alternating charge developed on the polymer surface will develop a charge in the electrode as well (opposite polarity of the polymer).

Behavior of drops on the polymer surface are of interest when studying the energy harvesting method of triboelectric charging. Research has been done on how drop behavior on a polymer surfaces may be altered by modifying the polymer surface. This has been done by creating tiny structures on the surface [7, 8, 9, 10]. Creating structures on the surface of polymers have reduced the adhesion between water drops and the polymer surface. If drops roll off easier, there would be a smaller chance of water forming a continuous film on the surface at less steep inclinations of the polymer or at heavy rainfall. A continuous film of water on the surface is undesired, because this will decrease the energy harvesting rate [7].

1.2 Thesis objectives

The objective of this thesis is to support the rain cell project at the University of Bergen, with focus on the polymer surface of the rain cell. Nano-structures will be created on the surface using reactive ion etching (RIE). Through the nano-structuring, it is desired to gain a better understanding of how different RIE parameters affect the shape and size of the resulting structures. Moreover, how different surface morphology affect the wetting properties of the polymer. In order to study the wetting properties, suitable measurement methods must be researched and developed.

1.3 Thesis outline

Chapter 1 gives a brief introduction to the research field of this thesis. Chapter 2 contains descriptions of the instrumentation and experimental methods, along with some theoretical background. Chapter 3 presents the results of the experimental work, i.e. characterization of morphology and wetting properties of the nano-structured polymer films. A discussion of the results are given in chapter 4, in addition to some suggestions for further work. Ultimately, a conclusion of the thesis project is given in chapter 5.

Chapter 2

Background and experimental methods

The material, instruments, software and experimental methods used during the work of this thesis will be addressed in this chapter. Beginning with the material used, followed by the instrument and methods relevant for the fabrication of the the films. Finally, all parts concerning analysis of the nano-structured films are presented.

2.1 Fluorinated Ethylene Propylene

The material used for this work is fluorinated ethylene propylene (FEP) (figure 2.1), also known as fluoroethylene-propylene copolymer. FEP is a transparent (transmittance $>$ 94% for thin films [7]) thermoplastic film. It is chemically inert to most chemicals, has wide thermal range (-240 to 205°C), low mechanical friction, high resistance to tearing etc., thus being an appropriate choice of material for a variety of applications [12].

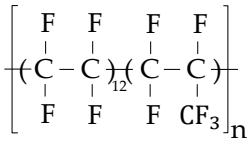

FIGURE 2.1: FEP structure. (Redrawn from Ref. [11])

During the work of this thesis, there are two environments that are of special interest: inside a scanning electron microscope (SEM) and in contact with water. In section 2.3 (about SEM), it is said that the electrical conductivity of the samples to be investigated in the SEM has importance for which settings one should use and the image quality. In this case, the FEP is an electrical insulator with surface resistivity of $R > 10^{16}\ \Omega/\mathrm{sq}$.

As seen in figure 2.1, FEP is formed from strong carbon-carbon and super strong carbon-fluorine interatomic bonds. This structure gives FEP properties such as low surface tension and insolubility, which makes it nonwetting to water among other solvents [13].

The FEP films used for this thesis work is produced by DuPont and have a thickness of 25 μm.

2.2 Nano-structuring by reactive ion etching

Etching is a common method used in micro- and nano-fabrication. Etching can be divided in two categories, wet etching and dry etching. Wet etching is performed with liquid chemicals as etchant. It serves good selectivity of what materials will be etched, and has a highly isotropic etch profile (see figure 2.2b), meaning it etches equally fast in all directions for amorphous materials. Dry etching, also known as plasma etching, offers better control of isotropy. This is a top-down manufacturing method with many fields of application such as fabrication of semiconductors.

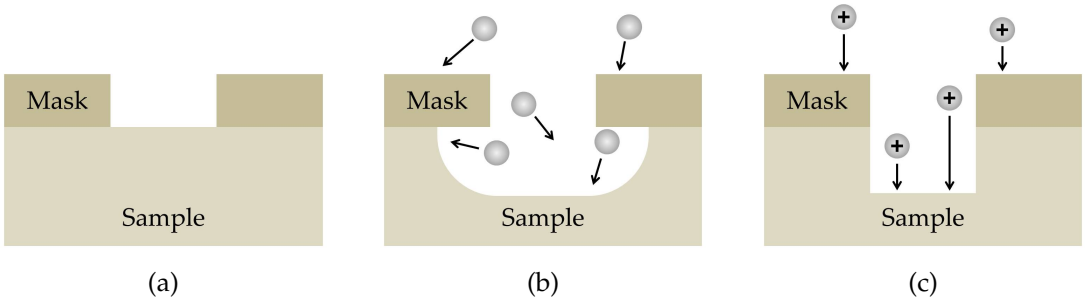

FIGURE 2.2: (a) Substrate prepared for etching with mask. (b) Chemical etching by neutral radicals, this process etches in all directions (isotropic). A chemical etch process is highly selective as the reaction species only react with the sample, not the mask. (c) Physical etching by charged particles, sputtering the substrate surfaces with the same incident angle (anisotropic). A physical etch process is not selective as the sputtering also damages the mask.

2.2.1 Plasma

Most matter on earth is in the solid, liquid or gas state. Yet, some matter is in the plasma state. Plasma is a gas consisting of neutral and charged (electron and ions) particles [14]. Since plasma is such a fundamental part of dry etching processes, a brief introduction will be given.

Atoms are fundamental elements of matter. Consisting of a nucleus and a cloud of electrons, orbiting the nucleus. The nucleus consist of protons and neutrons, protons being positively charged, and neutrons having zero charge. The electron is negatively charged, with the same magnitude as the proton. If an atom has the same amount of protons and electrons, the atom has a net charge of zero. If one or more electrons are removed or added from an atom, the atom is charged and is now known as an ion. A neutral oxygen atom can be seen in figure 2.3

The binding energy of each electron in an atom, is the energy required to remove the electron to an infinite distance from the atom's nucleus, i.e. to a distance where the attractive forces of the positively charged nucleus will not affect the negatively charged electron. This is also known as the ionization energy. For the innermost shell of the atom, the binding energy is of larger magnitude than the shells further from the nucleus.

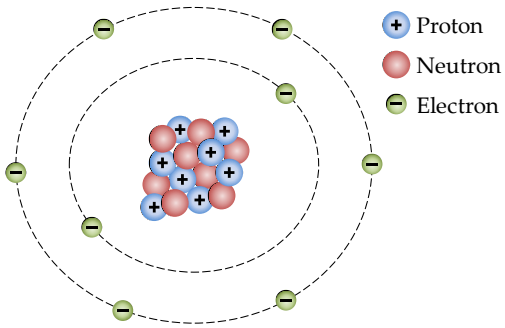

FIGURE 2.3: An oxygen atom consist of 8 electrons orbiting the nucleus. The nucleus consist of 8 neutrons and 8 protons. An equal number of negatively charged particles (electrons) and positively charged particles (protons) makes the atom have a net charge of zero.

Since plasma consists of charged particles, it is electrically conductive. It also interacts with magnetic fields. If a plasma consisted solely of charged particles, it would be fully ionized. Plasma in reactive ion etchers are typically a glow discharge plasma, being a weakly ionized plasma. The ionization degree is typically in the range $10^{-6} - 10^{-4}$ for a glow discharge plasma, which means that 1 out of 10^4 gas molecules/atoms are ionized at most. The plasma density (or ion density and electron density, that is approximately equal) is about $10^9 - 10^{12}$ cm^{-3}. Such a plasma is also known as a low temperature plasma with a gas temperature of approximately 300 K [15].

2.2.2 Particle interactions in a plasma

There are two categories of collisions that may occur between electrons, ions and neutral species in a plasma: elastic and inelastic collisions. During elastic collisions, the total kinetic energy of the incident electron and the atom is conserved, it does not change. On the other hand, during an inelastic collision, the total kinetic energy is not conserved, i.e. some of the energy of the incident electron will be transferred to internal energy of the atom or molecule. Collisions between an electron and an atom may have different outcomes, depending on the energy of the incident electron. Some common interaction mechanisms will now be addressed.

Excitation

When the incident electron has less energy than the atom's or molecule's binding energy, it is not able to remove one of it's electrons. Rather, it can transfer energy to an electron in an inner shell of the atom. Now, the electron will jump to a higher energy shell, exciting the atom to an unstable state. Eventually, the electron will jump back to the vacant spot in the inner shell, releasing energy in the form of a photon. The reaction is described as (A = atom, A^* = excited atom, e = electron, γ = photon):

$$\mathrm{A} + \mathrm{e} \rightarrow \mathrm{A}^* + \mathrm{e} \rightarrow \mathrm{A} + \mathrm{e} + \gamma \tag{2.1}$$

Ionization

If the energy of the incident electron is greater than the binding energy of the atom, it is able to eject an electron from the atom. In this case, the atom is ionized, giving it a positive

charge. The reaction is described as:

$$\mathrm{A} + \mathrm{e} \rightarrow \mathrm{A}^{+} + 2\mathrm{e} \tag{2.2}$$

Dissociation

There is a binding energy associated with a molecule, the energy keeping all the components together. If an incident electron has greater energy than the binding energy of the molecule, the molecule may be split into smaller pieces as a result of the collision with the electron. The reaction is described as:

$$\mathrm{AB} + \mathrm{e} \rightarrow \mathrm{A} + \mathrm{B} + \mathrm{e} \tag{2.3}$$

The byproducts of such a reaction, are often highly reactive and prone to combine with other atoms or molecules.

Electron attachment

An incident electron attaches to an atom or molecule, adding negative charge, resulting in a negative ion. The reaction is described as:

$$\mathrm{A} + \mathrm{e} \rightarrow \mathrm{A}^{-} \tag{2.4}$$

2.2.3 Plasma in the reactive ion etcher

Even though plasma only exist naturally a few place on earth (e.g. in electric discharges and flames), it can be prepared by creating an environment where a gas can be ionized. This is utilized in reactive ion etchers (RIE) by applying an oscillating electric field, $\vec{E}$. As $\vec{E}$ changes direction, the free electrons in the gas will experience a force changing direction with $\vec{E}$. The accelerated electrons might collide and interact with atoms and molecules as described above. As particles are being ionized, more free electrons will be available for new collisions, possibly resulting in more ionized particles. This avalanche of collisions enables the gas to be sufficiently ionized for etching purposes. During such avalanches, the gas may also be radicalized, resulting in neutral molecules that are highly reactive.

In figure 2.4, one can see how a typical instrument set-up looks like. In an instant, $\vec{E}$, will be directed from the bottom electrode to the upper electrode. Shortly after, it will be the other way around, thus accelerating all charged particles up and down. The ions has much larger mass than the electrons, and will barely move, while the light electrons will move far, and even hit the top and bottom electrodes. The top electrode is connected to ground, thus leading impacting electrons away from the surface. The bottom electrode is not grounded, hence negative charge will build up on the surface. Due to the electrical conductive properties of the electrode, the negative charge will be distributed evenly across the surface.

From a macroscopic point of view, the plasma between the electrodes consists mainly of positively charged ions, while the bottom electrode has a negative charge. This results in an electrical potential, V_{dc}, in the order of a few hundred volts between the plasma and the bottom electrode. This electrical potential will accelerate positive ions from the plasma in the direction of the bottom electrode, thus bombarding the surface of the electrode.

In a RIE chamber, excitation, ionization and dissociation, is the most important interaction mechanisms between electrons and atoms/molecules. During operation, excitation of

atoms and molecules, followed by emission of a photon, gives the plasma a glowing light blue appearance. Ionization of atoms and molecules is essential for the generation of plasma from neutrally charged gasses. As the amount of free electrons increase, more free electrons are able to collide with natural atoms and molecules. Also, the increasing V_{dc} is important for the physical etching mechanism (addressed below). Dissociation of molecules results in different reaction species (A and B in equation 2.3). These species are either ions or neutral radicals, the first contributing to physical etching and the latter to chemical etching.

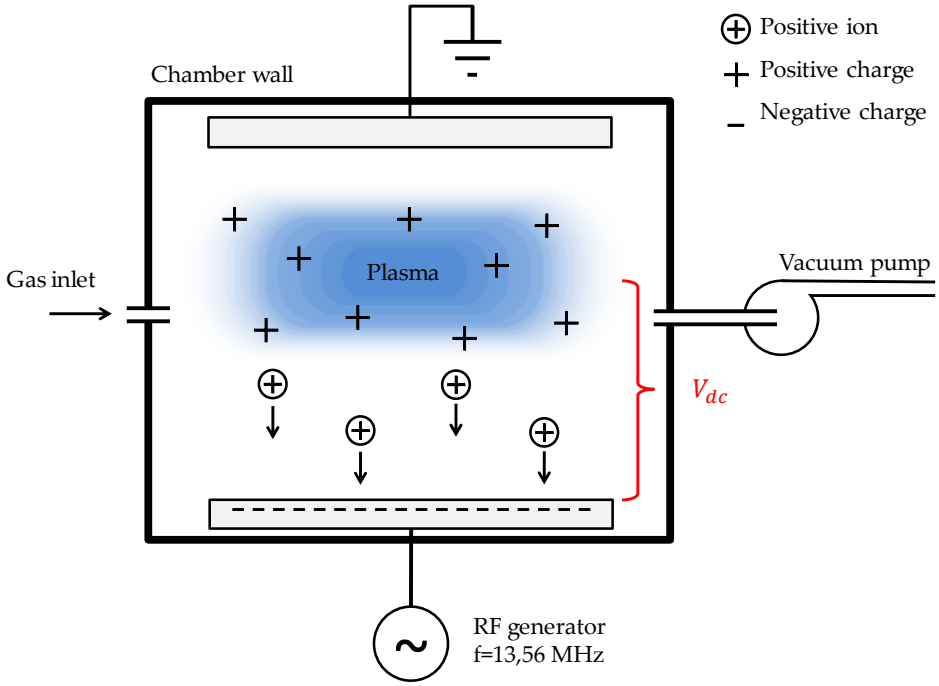

FIGURE 2.4: RIE chamber. An oscillating electric field accelerates electrons inside the chamber. The top electrode is connected to earth, electrons hitting it will be conducted out of the chamber. The bottom electrode is isolated, thus electrons hitting it will accumulate, giving it a negative charge. Ions are heavy compared to electrons, and will not be affected in the same way by the oscillating electric field, leaving them in place. The positively charged plasma and the negatively charged (bottom) electrode gives rise to a constant electric field, or bias voltage, V_{dc}. This electric field will accelerate positive ions from the plasma towards the bottom electrode, where samples can be placed for etching. (Redrawn from Ref. [16] (figure 2.8) and Ref. [15])

2.2.4 Etching of polymers

Physical etching

As V_{dc} arises, the electrical potential will accelerate positively charged particles from the plasma towards the substrate. The direction of the accelerated particles will be straight down toward the substrate, since the positive charge in the plasma is distributed equally in the horizontal plane inside the chamber, and the negative charge is distributed equally on the bottom electrode. These fast moving particles causes physical sputtering of the sample surface, as illustrated in figure 2.2c.

Chemical etching and selectivity

The reaction species generated from dissociation of molecules plays a key role in the mechanism of chemical etching. The reaction species contributing to chemical etching are neutral, not charged like the ions contributing to physical etching. As these reaction species are neutral, they are not accelerated by $\vec{E}$, and will travel in all directions inside the chamber, resulting in an isotropic etch profile (figure 2.2b). When these species travel toward the sample inside the RIE, they may adsorb on the target sample. The specie is then making a chemical bond with atoms on the sample surface, resulting in a volatile by-product that will desorb and get pumped out of the chamber.

As the removal of material by reactive species depend upon chemical reactions taking place, one can control the selectivity of the etch process by carefully choosing the gases used. For instance, a thought substrate consists of multiple layers of different materials. The top layer is used as a masking material for the underlying layer. To get a high etch selectivity, the etch gases can be chosen so that certain reaction species are generated, which are highly reactive with the underlying layer, and has very low etch rate for the top, masking material. In this case, the gas choice provided good selectivity as the bottom layer was etched, and the top masking material was left undamaged.

Etch rate

The etch rate differs quite a lot depending on the process conditions. Physical etching alone is relatively slow, at some hundred angstroms per minute. Chemical etching, and especially ion assisted etching (synergy effect of physical and chemical etching) obtains higher etch rates, at several thousand angstroms per minute [16]. Some parameters that can be varied to control the etch rate are mentioned below.

RF power and ion energy. The self bias, V_{dc} is dependant on the RF power, thus the RF power determines the electrical potential accelerating the ions, i.e. what gives the ions their kinetic energy (E_{k}). This is related to momentum (p) as $E_{\mathrm{k}} = p^2/2m$, where m is the mass of the ion. Physical sputtering is a consequence of momentum transfer, thus the momentum of the ions in the process contributes to the sputter yield. For energies below 3 eV, physical adsorption takes place. Some surface damage takes place at energies between 4 and 10 eV. At about 10 to 5000 eV, ions are most effectively removing material from the substrate. At even higher energies (10-20 keV), ions are implanted into the substrate [16].

Chamber pressure. Considering the ideal gas law:

$$pV = nkT \tag{2.5}$$

where p is the pressure, V is the volume, n is the number of molecules, k is Boltzmann's constant, and T is the temperature of the gas. According to equation 2.5, an increase in pressure also result in an increased number of molecules in the gas if the temperature and volume is kept constant. Thus, varying the pressure in a RIE chamber will affect the mean free path. The mean free path is the average distance a particle travels between two incidents of collision with other particles. If an ion is to reach the substrate without loosing too much energy (required for sputtering), a sufficiently long mean free path, thus low pressure is required. Even though a low pressure makes it easier for the ions to reach the substrate without collisions, however, a very low pressure is not desired. By lowering the pressure, more ions will escape the chamber through the vacuum pump, resulting in a lower plasma

density [16].

Gas composition and flow rate. Different gases turn to different reaction species, which again react differently with the material to be etched. The reaction by-products have different vapor pressure, which is fundamental for how easily it will desorb and be removed from the substrate. E.g. fluorides are more volatile than chlorides when etching Si [15]. This illustrates why it is important to carefully consider what gas, or combination of gases to use, and the amount (flow rate into chamber) used. If the reaction species promote both physical and chemical etching, a synergy effect called ion assisted etching takes place, which increases the etch rate significantly.

Substrate temperature. The reaction rate of two substances rises as the temperature increases [17], thus higher substrate temperatures promote chemical etching. In addition, the vapor pressure of etch by-products rises as the temperature increases, i.e. the by-products become more volatile at higher temperatures [15].

Redeposition from byproducts

If the etch by-products are nonvolatile, they are not easily removed from the substrate surface through the vacuum pump, and may redeposit and polymerize onto the substrate. Redeposition occurs mainly on sloped sidewalls, altering the geometry of the substrate surface. This can work as a protection for sidewalls, promoting a highly anisotropic etching if controlled properly. By introducing reactive species to the etch process, redeposition will be reduced [16].

2.2.5 Preparation and etching of FEP films

Prior to etching the FEP films, they where rinsed carefully in order to remove particles and contamination that may be present on the surface. This was performed by first rinsing the film with isopropanol, then dried with N_2 before rinsing with deionized water, then dried with N_2 once more. After the FEP films were rinsed, they were placed in the Plasmatherm 790+ for etching. To obtain different surface roughness, different etch parameters were used to alter the etch process. As a starting point, the settings used by Helseth and Guo [7] was used, having a gas composition of O_2, Ar and CF_4. The different settings used for etching the FEP are listed in table 2.1, where each set of settings has been named with a letter. When the recipes are mentioned later in this work, the letter is often accompanied by a number describing the etch duration. E.g. A5 means that the settings listed for recipe A has been used to etch for 5 minutes.

After the first few etches, it was adapted from Ref. [18] to weigh the samples before and after RIE treatment. The instrument used for weight measurements is a Kern ABT 220-4M. The scale has reproducibility of 0.1 mg. To estimate the sample weight loss, the following equation is used:

$$\Delta m = m_{\mathrm{b}} - m_{\mathrm{a}} \tag{2.6}$$

m_{b} is the mass before RIE treatment, and m_{a} is the mass after RIE treatment. The weight loss is also presented as percentage weight loss relative to the mass before RIE treatment:

$$\%\Delta m = \frac{\Delta m}{m_{\mathrm{b}}} 100\% \tag{2.7}$$

To determine the etch rate (nm/min), an assumption is made that the weight loss is mainly due to removal of material in the vertical direction, i.e. reduction of the thickness (t) of the FEP film. The etch rate then becomes:

$$\text{Etch rate} = \Delta m \cdot t \tag{2.8}$$

TABLE 2.1: Etch parameters used to etch FEP films in Plasmatherm 790+. Unit of gasses are SCCM. Recipe A uses the same parameters as Ref. [7]. Recipe F was not successfully conducted due to the RIE was not able to maintain such low pressure throughout the process. When a recipe is mentioned with a number behind, the number indicates etch duration in minutes. E.g. A5 means the etch duration is 5 minutes.

Recipe	P [W]	p [mTorr]	O_2	Ar	CF_4
A	400	10	10	15	30
B	400	10	10	15	15
C	400	10	10	15	
C^1	400	10	5	7.5	
C^2	400	10	2.5	3.75	
C^3	400	10	1.25	1.875	
C^4	400	10	0.83	1.25	
D	400	10	10		
E	400	10		15	
F	400	5	10	15	
G	400	100	10	15	
H	400	5	5	7.5	

2.3 Imaging with scanning electron microscope

The scanning electron microscope (SEM) is a much used instrument for imaging and analyzing micro- and nano-structures. These instruments offer resolution of a few nanometers for conductive samples, and a depth of field superior to that of optical microscopes [19]. Such properties make SEM an excellent tool for characterizing nanoscale structures.

2.3.1 Principle of SEM

A schematic drawing of a SEM's electron column is found in figure 2.5. At the top, there is an electron gun consisting of a filament working as a cathode. Below the filament is another electrode, having a positive potential relative to the cathode, thus accelerating electrodes released from the cathode. The electrons are typically accelerated to an energy of 0.1 - 30 keV.

By increasing the acceleration voltage, the electrons will gain more energy, and the electron range into the sample increases. Thus, high acceleration voltages make the signals give information from deeper within the sample, which reduce the contrast for surface features [20]. Depending on the sample density and the acceleration voltage of the electrons, the electron range is typically in the range 10 nm - 10 μm [20].

As the electrons are accelerated past the anode, the beam of electrons is too wide to obtain any useful image resolution. Because of this, two or more magnetic lenses (B in figure 2.5) are used to focus the electron beam [19]. Scan coils are powerful lenses, able to control the width and direction of the electron beam with high accuracy (D in figure 2.5). When an image is generated, the electron beam is focused on one small spot on the sample. Secondary electrons generated by the primary electron's interaction with the sample are detected by an electron detector (F in figure 2.5) The electron detector is a positively charged electrode, attracting scattered electrons. The magnitude of the current, induced by the electrons collected, determines the intensity of the pixel drawn for that specific position on the sample. Next, the beam is moved a small distance on the sample, and the intensity of the next pixel is acquired. This is repeated until enough pixels are drawn to make a full image [19].

2.3.2 Image quality

Image quality is related to the electrons hitting the sample being imaged. More electrons bombarding the sample, increase the amount of electrons that scatters off the sample. More scattered electrons result in an increased amount of electrons detected, thus resulting in stronger signal. This increases the signal to noise ratio and promotes image contrast (ability to distinguish image features) [19].

The electrical conductivity of the sample is also important for the image quality. If the sample is not able to conduct electrical charge to ground (through the sample holder), charge will accumulate on the surface of the sample. This charge will then deflect the path of the incoming electrons, and introduce image drift and distortions [21]. Less charge accumulation can be obtained by reducing the amount of electrons incident on the sample. This can be done by reducing the aperture diameter, which will reduce the overall beam current. Also, by reducing the acceleration voltage of the electrons, the electrons are more likely to interact close to the surface. This makes the electrons more likely to scatter off the surface

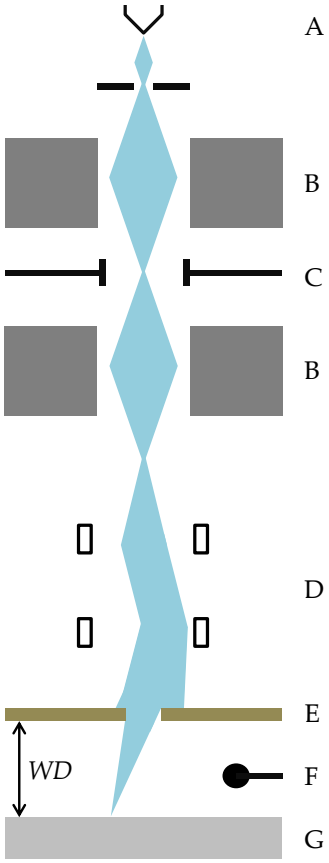

FIGURE 2.5: Electron column inside SEM. The column contains an electron gun (A), electron lenses (condensers) (B), electron beam blanker (C), scan coils (D), final lens aperture (E), detector (F) and sample (G). The distance between the final lens aperture and the sample is known as the working distance (*WD*). (Redrawn from Ref. [19])

instead of being trapped in the sample. Image drift may be reduced by eliminating electron beam stigmation [21], which also promotes image sharpness.

Samples that are electrical insulators can be difficult to image with adequate image quality. One way of improving the image quality is by coating the sample with a thin film of conductive material. However, one needs to be aware of the magnitude of the features to be imaged compared to the thickness of the coating, as the coating may modify the shape and size of the features. An FEP film etched by recipe A3 was sputter coated by a thin layer of gold (Au) and palladium (Pd) (can be seen in figure F.5 in appendix F). It was obvious that the coating altered the sample surface, leaving it impossible to conduct precise measurements. After testing different SEM settings, adequate image quality was obtained, minimizing any charging effects and simultaneously allowing good measurements of the insulating sample to be carried out. Therefore non-coated samples were investigated in the SEM at the cost of some image resolution and contrast.

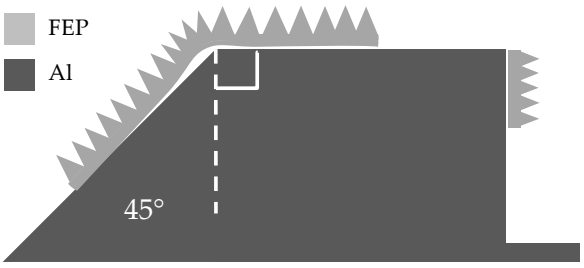

FIGURE 2.6: Conceptual drawing of the sample holder used for imaging the FEP structures with a scanning electron microscope. Aspect ratio of the FEP and its structures are highly exaggerated. Sample holder enables imaging of the FEP structures at $45°$ on the left diagonal, from above on the flat area in the middle, and the FEP's crossection ($90°$) on the right vertical side.

2.3.3 Analysis of SEM images in ImageJ

ImageJ [22] has been used to analyze SEM images of nano-structures, and has been implemented on images covering an area of 11.4x8.6 μm^2 of the sample imaged. This however, is only a small fraction of the whole sample, being about 1.5x1.5 cm^2. This corresponds to a 10k magnification setting in the Raith eLine (SEM) software. The samples imaged and investigated using ImageJ are captured perpendicular to the nano-structured FEP films. To ensure a correct analysis of the SEM images, the ImageJ settings need to be set correctly. The procedure to do this is described below.

Calibrating scale. After an image has been opened, it is desired to make sure the scale (length per pixel) fits to the image being analyzed. By clicking *Analyze* followed by *Set Scale*, a pop-up window allows you to set the scale in a few different ways. The image files from the SEM contain information about the scale in nanometer per pixel. The scale can be found by opening the image file using e.g. Notepad. For the example in figure 2.7, 11.16 nm/pixel is chosen. When multiple images to be analyzed have the same magnification (scale), the *Global*-checkbox can be checked to let the scale apply for all images analyzed until ImageJ is closed.

Smoothing. In a perfect world, an image of a spike or cone-looking object, should be represented by a continuous grey scale gradient from its root to its top. This is not the case for the SEM images obtained for this thesis. To make an image more applicable for conversion to binary color, the image can be made smoother by clicking *Process* in the menu bar, followed by pressing *Smooth*. If not applying the *Smooth*-function, one structure will appear as one black dot of pixels a little bit smaller than the actual structure, surrounded by individual black "satellite" pixels, which ImageJ in turn will interpret as individual structures. This is avoided by applying the *Smooth*-function prior to further preparations in advance of analyzing the image.

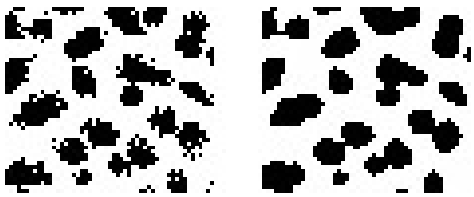

FIGURE 2.8: Smooth function in ImageJ. The right image has been applied smoothing.

Converting to binary. In order to determine what areas in the image should be interpreted as a spike or structure, ImageJ is dependent on having a binary image (1 bit), where one pixel color represents a spike top, and another pixel color represents a valley around the same spike. By clicking on *Image* in the menu bar, then *Adjust* and *Threshold*, a window

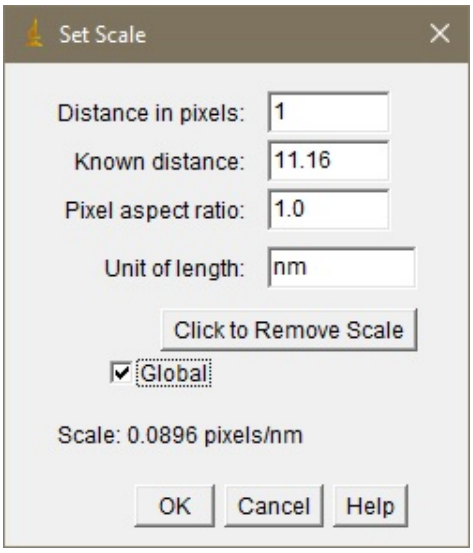

FIGURE 2.7: Setting the scale in ImageJ. The length of the image pixels may be found by opening the image file in e.g. Notepad (Windows). In this example, one pixel correspond to 11.16 nm.

pops up (figure 2.9). Different options are available for how one want the resulting image to look like. *Default* and *B&W* (black and white) are chosen in the drop down menus. *Dark background* is selected before clicking *Apply*. Now the original 8 bit image has been converted to a 1 bit image. In figure 2.9, all the pixels with a grey scale color above 92 (0=black, 255=white) will turn out black in the binary image, and be interpreted as a spike top by ImageJ.

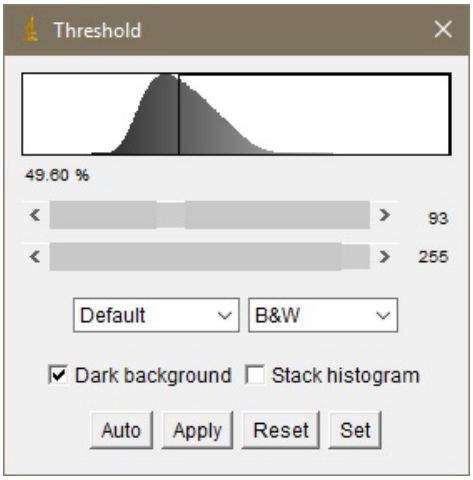

FIGURE 2.9: Pop-up window in ImageJ with options for converting an image to binary color scale.

Splitting merged spikes. Due to inadequate resolution of the SEM images analyzed, multiple spikes may be so close in the image, that ImageJ will not recognize the trench between them. E.g. three spikes may be interpreted as one big spike instead of three small ones. ImageJ has a function where it can detect spots that look like they consist of multiple circular dots, and split them by drawing a 1 pixel wide line between them. This can be done to the whole image by clicking *Process*, then *Binary* followed by *Watershed*. How this works is

illustrated in figure 2.10.

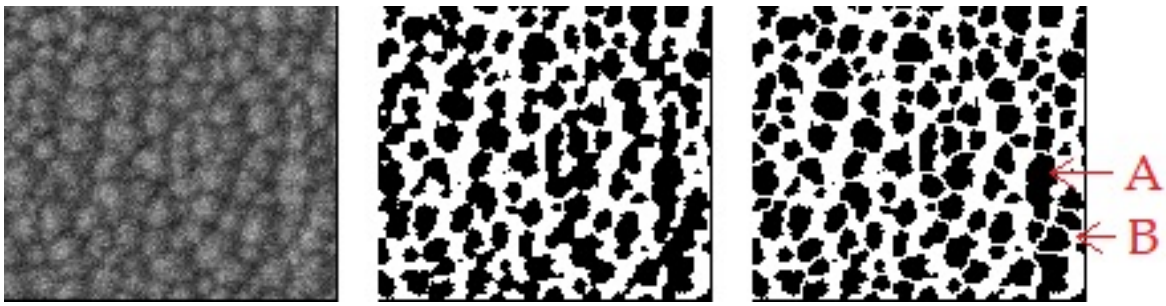

FIGURE 2.10: Watershed-function in ImageJ. All images are from the exact same place in the original image (left). In the middle, the image is converted to binary scale. The right image has the watershed function applied. Arrow A points at a big black dot where the watershed function failed. Arrow B points at an area where the watershed function split multiple spikes successfully.

Analysis of prepared image. The image is now prepared for analysis, which is done by clicking *Analyze* in the menu bar, then click *Analyze particles*. A window pops up with options for the analysis (figure 2.11). For the analysis of all samples, all sizes of black dots are counted as a structure. By checking *Display results*, each and its area is displayed in a table. This can be saved in a file for further usage. By checking *Summarize*, some data for the whole image is displayed. This includes the average dot size, percent coverage of dots in the image and number of dots in the image. The image dimensions are known from the image file, thus the number of structures (referred to as structure density in chapter 3) per unit area can be calculated.

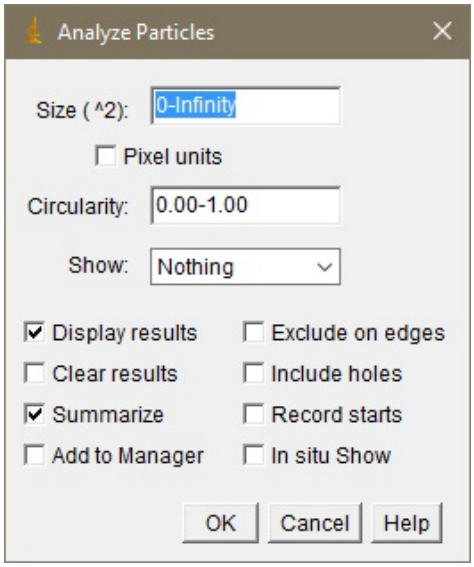

FIGURE 2.11: Options for analyzing particles in ImageJ.

For this thesis work, files have been saved for plotting histograms in Matlab. The areas will typically be in the range $10^3 - 10^4$ nm^2 or $10^{-3} - 10^{-2}$ µm^2, which are either relatively large or relatively small numbers. In addition, when speaking of the size of a cone, using the

area of its cross section is a bit inconvenient, height and diameter is therefore used instead. The area (A) counted by ImageJ is therefore converted to diameter (d) by

$$d = \sqrt{\frac{4A}{\pi}} \tag{2.9}$$

This conversion assumes the dots are perfect circles, which they are not. Taking the uncertainty into account of choosing the threshold for converting to binary color scale, the circularity of the dots are assumed to be of little significance. Thus, the conversion by equation 2.9 should be adequate for this case.

Verification of diameter-estimate

To verify the accuracy of the main method for estimating the diameter (described above), a C5 sample is used. The main method is later applied for all samples presented in the results section.

The C5 sample with two extreme (high and low) thresholds are compared to measurements of an image of the cross section of a sample etched with the same settings. The diameter of 50 spikes was measured. This was done by drawing a line across the width of the spikes, about 50 - 100 nm below the tip in ImageJ. In figure 2.12, one can see how the measurement lines were drawn, each line with an individual number corresponding to the order they where drawn. The length of the lines are presented in a separate result window in ImageJ. The results are saved to a file for further calculations of mean and standard deviation by equation A.3 and A.4. The results of this comparison is presented in table 2.2.

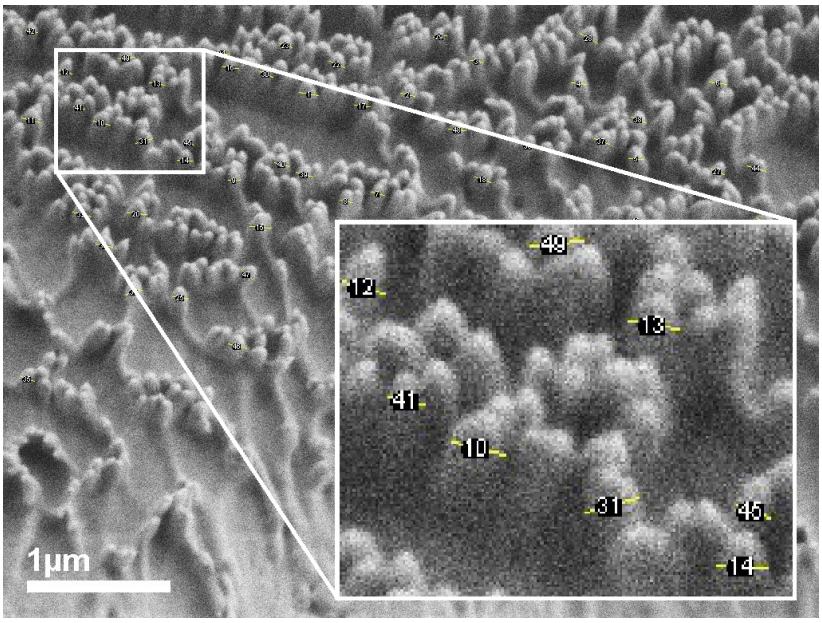

FIGURE 2.12: Diameter measurements in cross sectional image of FEP etched by recipe C5. The structures are bent toward the lens by the scalpel cutting through the film. 50 measuring lines are drawn about 50-100 nm below the tip of the spikes. The lines measure the diameter of the spikes. The number on each line indicates in which order the line was drawn (it is not the diameter). The length (diameter) of each line is presented in a separate window.

TABLE 2.2: Comparison of extreme threshold for C5 sample. These data are obtained from the same analysis as presented in figure 2.13. Equation 2.10 is a proposed method for determining a threshold to use for the image analysis.

Threshold/data	50-255	95-255	Cross section	Eq. 2.10
# structures	4122	6416		5397
% area coverage	71%	27%		52%
Diameter (mean)	140 nm	70 nm	110 nm	110 nm
Diameter (std.)	40 nm	20 nm	20 nm	20 nm

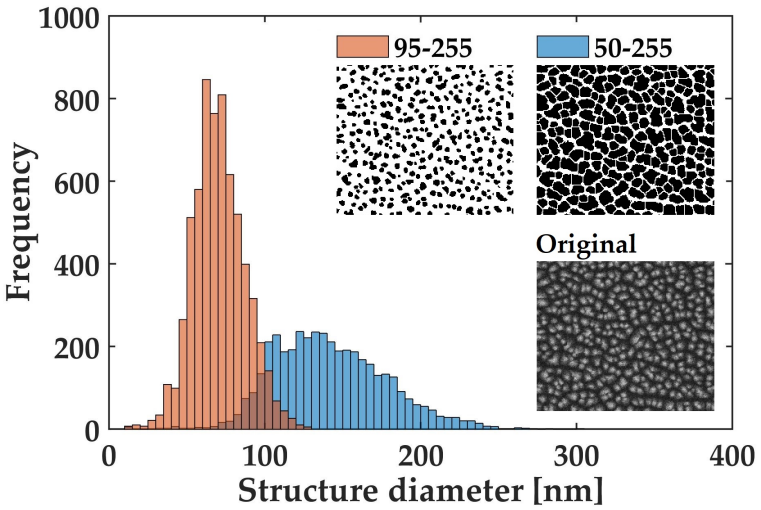

FIGURE 2.13: C5 diameter distribution with low and high threshold.

The measurements of the cross sectional image turns out to be in between the results of the high and low extremes of the threshold, which illustrates the importance of choosing threshold for the binary conversion, and the need to be consistent when analyzing different images of different samples. How the spike diameter was affected by using two extreme thresholds is illustrated in figure 2.13. The calculated diameter for the low extreme threshold results in a mean value twice as big as for the high extreme threshold. It also results in counting about 35% less individual spots (structures). Thus, a method to determine an optimum threshold is needed to optimize the repeatability of the ImageJ analysis. The method proposed below is used for the measurements presented in chapter 3.

Other sources of error lies in the limitation of the watershed-function illustrated in the right image in figure 2.10. I.e. some structures are merged and appear as one big spike instead of multiple small ones in the binary image used for analyzing the size of the structures. This results in counting less individual spots then what is present in the image. Also, the diameter distribution will be shifted towards a larger magnitude. Both the choice of threshold and the performance of the watershed-function is affected by the image contrast and sharpness. In addition, if different surfaces are to be compared through ImageJ analysis, sharp images with similar contrast will result in less systematic error in the results.

Determining the optimum threshold

Above, several sources of error and an investigation of setting the threshold was presented for an image of a sample etched by recipe C5 (used as an example). During the investigations, one approach resulted in a fairly comparable diameter as estimated from the cross sectional image. The approach was as follows, find a maximum threshold value when the smallest structures are about to disappear (like 95 in figure 2.13). Find a minimum threshold value when the structures are merged quite a lot, but the structures can still be distinguished (like 50 in figure 2.13). Then, the threshold (T) was chosen to be 10% less then the mean value of T_{max} and T_{min}:

$$T = \left(\frac{T_{max} + T_{min}}{2} \right) \cdot 0,9 \tag{2.10}$$

From equation 2.10 for the example above, the threshold was chosen to be 65 - 255. This resulted in a diameter of 110 $\pm$ 20 nm, which is the same value as calculated from the 50 measurements in the cross sectional image.

2.4 Surface wetting and wetting property measurements

When studying the wettability of surfaces, this is often done by the means of contact angle (CA) measurements of liquid droplets laying on a surface. The CA is the angle of a tangent line (θ in figure 2.14b), formed by the liquid-vapor interface, passing through the liquid-solid-vapor interface (also known as the three phase contact line).

The CA indicates if a surface favors wetting or not. A small CA ($\ll 90°$) means the surface favors wetting, and a large CA ($\gg 90°$) means the surface do not favor wetting [23]. A surface favoring wetting is also known as being hydrophilic, and a surface not favoring wetting is also known as being hydrophobic.

Surface tension is the result of cohesive forces between neighboring molecules within a material (illustrated in figure 2.14a). For an H_2O molecule in the middle of a drop of water, cohesive forces attracts the molecule to surrounding molecules in all directions, resulting in a net force of zero. For the molecules at the surface of a drop, there are not neighboring molecules in all directions with associated cohesive forces. Thus, molecules at the surface will have a net force in the direction of the center of the drop. These intermolecular forces contracts the drop's surface, and is known as surface tension (γ). If no other forces were present, the drop would form a perfect sphere. However, external forces such as gravitation are present, resulting in deformation of the drop [23].

In figure 2.14a, three interfacial tensions and the CA can be seen for a drop resting on a solid surface. The relationship between the interfacial tension of the liquid-vapor (γ_{lv}), solid-vapor (γ_{sv}) and solid-liquid (γ_{sl}) interfaces, and the contact angle for a drop on a smooth, ideal surface, can be described by Young's equation [24]:

$$\gamma_{\mathrm{lv}}\, cos(\theta_{\mathrm{Y}}) = \gamma_{\mathrm{sv}} - \gamma_{\mathrm{sl}} \tag{2.11}$$

where θ_{Y} is Young's CA. θ_{Y} however, is often not equal the observed static CA [23]. For practical purposes, no surface is physically and chemically homogeneous. Surface roughness and chemical heterogeneity results in a different CA when a drop advances (θ_{a}) or

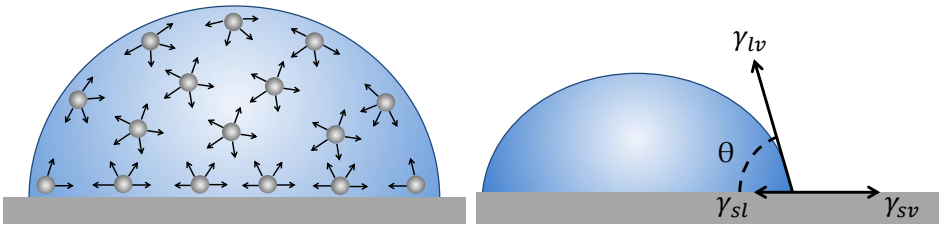

(a) (b)

FIGURE 2.14: (a) Intermolecular forces (illustrated by arrows) are acting on neighboring H_2O molecules (grey spheres) inside a drop of water. (b) Liquid drop on a solid surface. Young's equation (see equation 2.11) describes the relationship between the contact angle (θ) and the interfacial tension of liquid-vapor (γ_{lv}), solid-liquid (γ_{sl}) and solid-vapor (γ_{sv}).

recedes (θ_r) on a surface [25]. The difference between the advancing CA (ACA) and the receding CA (RCA) is also known as the CA hysteresis (CAH), $\Delta\theta$ [23].

$$\Delta\theta = \theta_a - \theta_r \tag{2.12}$$

Due to the hysteresis in the CA, the static CA alone is not adequate to describe the wetting properties of a surface [23]. Dynamic CA (ACA and RCA) measurements should be done, e.g. for a drop with an increasing and decreasing volume [26] or for a drop on a tilted plate [23]. The ACA may also be a good approximation for Young's CA in Young's equation (equation 2.11)[27].

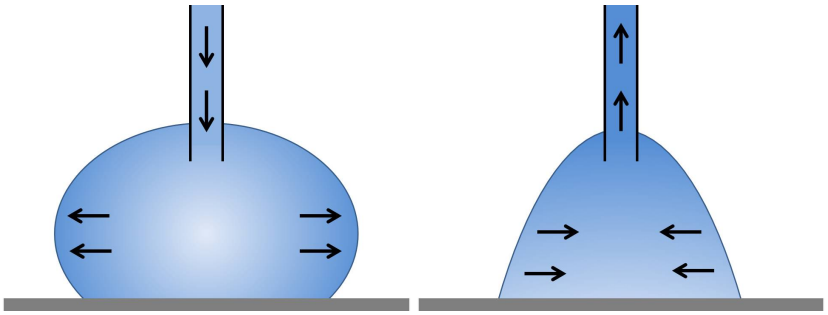

(a) Drop advancing on surface (b) Drop receding on surface

FIGURE 2.15: Dynamic contact angles as the drop volume is increasing (ACA) and decreasing (RCA).

2.4.1 Contact angle and adhesion force measurements by the tilted plate method

Since the sessile drop (needle in) method was found to be insufficient for CA measurements in this work (discussed in subsection 3.1.3), another method for measuring the CA was used, namely the tilted plate method. This section begins by explaining the general principle of the tilted plate method. This is followed by some considerations on a suitable drop volume to use in the experiments. Then, the approach of the experiments are described. Details on setup and functionality of the software (SCA20) are found in appendix B.

The tilted plat method is based on placing a drop on the sample of interest and then observing the droplet as the plate holding the sample is tilted. The plate is tilted until the

droplet rolls off the sample. At the maximum tilt angle before the drop rolls off, the critical tilt angle (α_c) is reached, also known as the roll off angle (ROA). At the critical tilt angle, the CA of the lower edge of the drop equals the ACA (θ_a), and the CA of the upper edge equals the RCA (θ_r) (see figure 2.16a) [28].

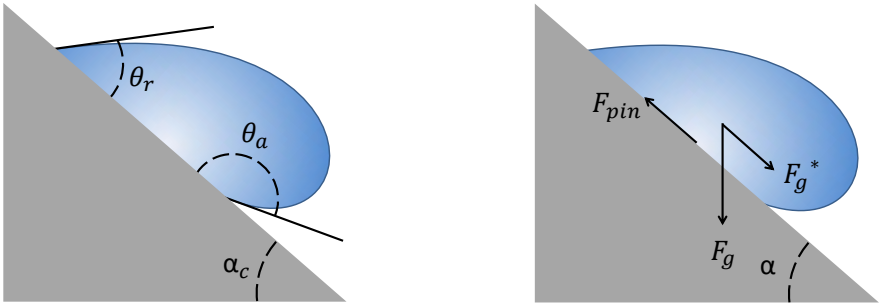

(a) (b)

FIGURE 2.16: Drop on a tilted plate. (a) θ_a and θ_r corresponds to ACA and RCA respectively when the surface is at its maximum tilt angle (α_c), before the drop rolls off. (b) When the drop is pinned to a tilted surface, F_{pin} is the adhesive force pinning the drop to the surface.

In figure 2.16b, forces acting on a drop on a tilted plate is illustrated. The magnitude of F_{pin} depends on the tilt angle, α, the mass of the drop, m, and of the gravitational acceleration, g [29]:

$$F_{pin} = -F_g \, sin(\alpha) = -mg \, sin(\alpha) \tag{2.13}$$

Determine a suitable drop volume

In order to determine ACA and RCA during experiments by the tilted plate method, the drop must roll off the sample at $\alpha < 90°$, which is the maximum tilt angle for the tilting unit for DataPhysics OCA 20L. To achieve this, a sufficient amount of water must be used. If not, $mg \, sin(\alpha)$ will not be greater than F_{pin} for $\alpha < 90°$, so that the drop will remain on the sample.

A few tests where done for a sample etched using recipe C5, where drop volumes in the range 40-80 µl were used and three experiments were done for each volume. The results are shown in table 2.3. For 40 and 50 µl, the drops were still pinned at $\alpha = 90°$ (maximum tilt angle for OCA 20L), thus more water was required.

For practical purposes, it is desirable that the drops are not unnecessary big. As the drop volume increases, the drop covers a bigger area of the sample, which means that more experiments can be done on the same film for smaller drops. To make comparison of different samples easier, the same drop volume is used for all further measurements by the tilted plate method. In case other samples etched by other recipes would show even stronger adhesion than the sample used in table 2.3, 70 µl was chosen, which is 10 µl more than the smallest drops that rolled off.

TABLE 2.3: Test of different drop volumes on FEP etched by recipe C5. Three experiments were done for each drop volume, mean and standard deviation are calculated by equation A.3 and A.4. All of the drops of 40 µl and 50 µl were still pinned to the sample at maximum tilt angle (90°), therefore no values of ROA (α_c), ACA (θ_a) and RCA (θ_r) are obtained for these volumes.

V [µl]	α_c [°]	θ_a [°]	θ_r [°]
40	-	-	-
50	-	-	-
60	62 ± 3	130 ± 2	34 ± 2
70	54 ± 6	134 ± 5	43 ± 3
80	52 ± 3	123 ± 2	34 ± 1

Preliminary preparations for tilted plate method

First, the tilting unit should be installed on the OCA 20L. Then, the camera's magnification should be adjusted for the drop size used, in order to reduce errors by the software's interpretation of the drops. E.g. if the software interpret the edge of the drop with an error of $\pm$ 1 pixel (px), the % error of the drop base diameter (*DBD*, the diameter of the drop in the liquid-solid interface) will be much larger if the *DBD* is represented by 20 pixels in the image instead of e.g. 400 pixels ($\pm$ 1 px / 20 px = $\pm$ 0.05 = $\pm$ 5 % and $\pm$ 1 px / 400 px = $\pm$ 0.0025 = $\pm$ 0.25 %). There should be some open space on the right side of the drop, since the drop will lean to the right when the FEP film is tilted. To further minimize error from the image quality, the focus should be placed on the center of the drop.

The camera's magnification and focus should be adjusted like mentioned for the sessile drop (needle in) method. As the only parameter of interest during these experiments are angles, calibration of magnification is not necessary. Still, in case *DBD* should be of interest later on, this calibration was done for all experiments. Prior to the tilted plate method, the diameter of the needle was measured by a micrometer with better resolution than the vernier caliper (details are found in appendix B). 0.505 mm was entered in the *Ref. - Size* field in the *M-Info* tab in the *Result* window (see figure B.4).

Parameters of interest are the right and left CA (θ_a and θ_r at the critical tilt angle, α_c), the tilt angle and the *DBD*. These parameters are exported (how this is done is explained in appendix B) to a file, and later used for plotting of data in Matlab.

Execution of experiments

The sample is first rinsed in deionized water, then shaken carefully until no drops remain on the surface. Since relatively big drops are used, that pin to the surface at steep inclinations, the sample is attached by a clip to a piece of glass. The piece of glass is attached by adhesive tape to the instrument. This way, the sample will not move as the plate is tilted.

When the sample is placed on the instrument, 70 µl of deionized water is dispensed onto the sample at a rate of 0.5 µl/s. The needle is placed close to the surface, so that the drop grows around the needle. Once finished dispensing, the syringe is carefully removed out of the image.

Next, an image of the drop resting on the surface is captured, and the CA on both edges of the drop is measured. This is done manually by clicking *Calculation* (button C in figure

B.3). Afterwards, the instrument is tilted 10° at a rate of 0.3°/s. This is done through the *TBU90e* control window. When finished tilting the instrument, another image is captured and the left and right CA is measured. This is repeated until the drop rolls off.

When the operator is expecting the drop to roll off in about 10-20°, a video of the drop should be recorded while tilting. This way, an image of the drop a few frames before it starts to roll off can be captured. The image may then be used to measure the CAs. The ACA is the CA on the lower edge of the drop, the RCA is the CA on the upper edge of the drop.

2.4.2 Calculation of solid-liquid adhesion by CA measurements

Furmidge [30] has presented a method for calculating the solid-liquid adhesion by means of CA measurements in a tilted plate setup like explained in subsection 2.4.1. The proposed relation between the adhesion force and the ACA, RCA, drop width (w) and the liquid surface tension (γ_{lv}) is:

$$F_{\mathrm{pin}} = -mg\ sin(\alpha) = w\gamma_{\mathrm{lv}}(cos(\theta_{\mathrm{a}}) - cos(\theta_{\mathrm{r}})) \tag{2.14}$$

This relation indicates that the difference between ACA and RCA (CAH) is the most important factor for the surface adhesion, and not the specific values of ACA and RCA itself [31].

For practical purposes, the actual width of the three-phase contact line is not possible to measure in the experimental setup of DataPhysics OCA 20L. For the calculations performed with equation 2.14, the *DBD* of the drop at α = 0° is used as w.

Chapter 3

Results

In this chapter, the results of the experimental work are presented. The results presented include analysis of SEM images, weight loss from etching, contact angle (CA) measurements, calculated adhesion forces and certain optical observations visible for a photo camera. The first section (section 3.1) will describe alternative CA measurement methods along with some results. These results show why these methods were insufficient for measuring CAs on the nano-structured FEP fabricated for this thesis work.

Multiple etch parameters have been used to create nano-structures on the surface of FEP films, each named by a letter (A-H). The etch parameters for all the recipes are listed in table 2.1. Recipe A to E, and C^x are presented in section 3.2 to 3.8. Finally, a comparison of all the recipes will be displayed.

SEM images presented in this chapter are captured either from above, at 45° or 90° (see figure 2.6). If an image is captured at 45° or 90°, this will be stated in the figure's caption. If the image is capture from above, this is not stated in the caption. The images presented in this chapter are captured with EHT = 1.5 kV and aperture of 7.5 μm. Settings like contrast, brightness, stigmation and stage height varies in all images.

CA measurements by the tilted plate method has been conducted with a drop volume of 70 μl for all samples. All experiments have been conducted in the same room, with ambient temperature in the range 20.3 to 23.0 °C, and relative humidity in the range 17 to 57 %. All weight measurements are performed with a Kern, ABT 220-4M scale with reproducibility of 0.1 mg.

3.1 Contact angle measurements by sessile drop (needle in) method

Finding and developing a suitable method to measure CAs on FEP with different surface morphology has required some research and testing. The first two methods tested (sessile drop (needle in) with small and big drops) and some results will be displayed in this section. The sessile drop (needle in) method turned out to be unsuitable for the RIE treated FEP prepared for this work. For this reason, measurements by the sessile drop (needle in) method is not included in the results for all the different etch recipes (section 3.2 to 3.9).

First, some preliminary preparations for the experiments will be addressed. Secondly, the execution of the experiments will be explained. Details on setup and functionality of the software (SCA20) are found in appendix B.

To determine advancing and receding contact angles (ACA and RCA), DataPhysics OCA 20L was used. The measurement set up can be seen in the simple sketch in figure 3.1a. A camera is pointed at a drop laying on a surface. The drop is illuminated from behind in order to obtain good contrast between the drop and the surroundings. Figure 3.1b shows a typical water drop on top of an FEP film.

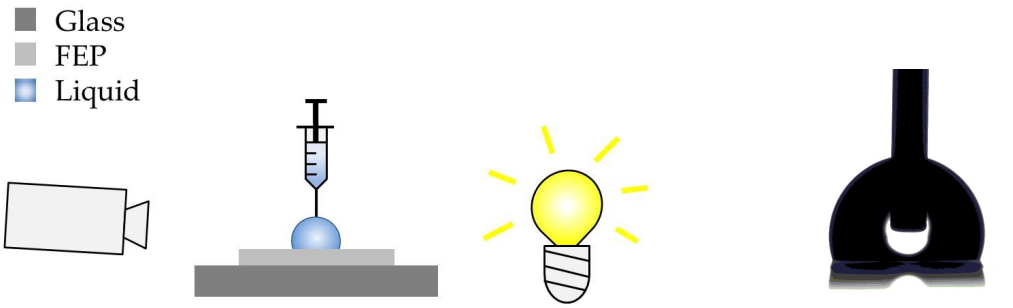

(a) Experimental set up for sessile drop (needle in). (b) Typical image.

FIGURE 3.1: Contact angle measurements with DataPhysics OCA 20L. The syringe is mounted to a stand, with an electrical motor driving the plunger for high precision injections.

At the surface-drop interface, a tangent (see figure 2.14b) is drawn on both sides of the drop. From the right CA and left CA, the mean value of the two is calculated and plotted by the software.

3.1.1 Preliminary preparations

In the *Live Video* window, *Sessile drop (needle in)* was selected in the drop down menu in the upper left corner. For positioning the horizontal lines, see figure B.3.

The magnification of the camera should be adjusted for the drop size used, in order to reduce errors by the software's interpretation of the drops. It is also desired to avoid too high magnification, as the drop may expand outside the field of view during measurements of an expanding drop. To further minimize error from the image quality, the focus should be placed on the center of the drop (where the diameter of the drop's cross section is largest). The parameters of interest are CA, *DBD*, drop volume (V) and drop age (T). These parameters are exported (how this is done is explained in appendix B) to file, then plotted

in Matlab.

At the time of working with small drops (and a few of the first measurements with big drops), the author was not aware of the need for entering the diameter of the needle manually, for the calibration of the magnification to work correctly. When this was discovered, a vernier caliper was used to measure the diameter of the needle, $d = 0.49 \pm 0.02$ mm (details are found in appendix D). 0.49 mm was entered as *Ref. - Size* in the *M-Info* tab in the *Result* window. All measurements presented after section 3.1 (section 3.2 to 3.9) are done with correct calibration.

3.1.2 Execution of the experiments - small drops

The user manual provided by DataPhysics does not present a complete strategy for performing ARCA measurements. Initially, several experiments was conducted to acquire reasonable parameters (initial drop volume, amount of water injected/withdrawn to/from the initial drop, and dosage rate) and criterion for choosing which data to be used for calculating mean of ACA and RCA. During these attempts, it was discovered that the nanostructured FEP films had high adhesion to water drops. This results in great CA hysteresis, i.e. great difference between ACA and RCA. An example of these experiments was as follows.

1. 4 µl of deionized water was placed carefully on the FEP surface. The needle was left inside the drop, close to the surface of the FEP.
2. 2 µl water injected into the drop at 0.5 µl/s.
3. Wait 2 seconds.
4. 2 µl water withdrawn from the drop at 0.5 µl/s.
5. Step 2-4 repeated 6 times, last time a video recording of step 2-4 was made.
6. The video was analyzed in the DataPhysics software, estimating the mean of the left and right contact angle of the drop throughout the injection and withdrawal.

The steps above was conducted four times on untreated FEP, rinsed with isopropanol and deionized water prior to the experiments. The results are plotted in figure 3.2. The CA fails to reach an equilibrium before the instrument is finished withdrawing water from the drop. So the question remains, would the CA continue to decrease if more water had been withdrawn? And how much? These questions proves that the method is inadequate of determining the RCA. This might also be the case for the ACA, but is most severe for the RCA.

Some experiments were carried out to see if the CA would reach an equilibrium at some other volumes. The initial volume, and the amount injected/withdrawn are listed in table 3.1 along with calculated ARCA mean and error (equation A.3 and A.4). Plots of the CA and the *DBD* as a function of time are plotted in figure 3.3. The grey areas show what time interval is used to calculate mean and error of ACA and RCA. Satisfying equilibrium in the CA is still not obtained, hence other approaches are investigated.

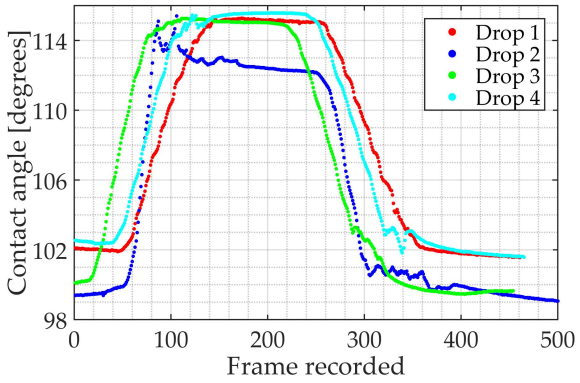

FIGURE 3.2: CA measurements on untreated FEP. Initial drop volume was 4µl, then 2µl was injected. 2 seconds later, 2µl was withdrawn. The moment when the CA stops decreasing in the area of frame 300-400, is the same time the withdrawal of water is finished.

TABLE 3.1: Small drops on untreated FEP. ARCA (mean and error) is calculated from the grey areas in the plots in figure 3.3, which is when the diameter of the drop-surface-interface is increasing or reducing.

Drop volume	$\overline{ACA}$	s_{ACA}	$\overline{RCA}$	s_{RCA}
$4\mu l + 1\mu l - 1\mu l$	$117.6°$	$0.7°$	-	-
$4\mu l + 2\mu l - 2\mu l$	$116.4°$	$0.2°$	$102.4°$	$0.5°$
$4\mu l + 3\mu l - 3\mu l$	$115°$	$1°$	$101.5°$	$0.5°$
$4\mu l + 4\mu l - 4\mu l$	$114°$	$2°$	$101.1°$	$0.4°$
$5\mu l + 2\mu l - 2\mu l$	$113.8°$	$0.7°$	$99.5°$	$0.6°$
$5\mu l + 3\mu l - 3\mu l$	$112.7°$	$0.5°$	$99.8°$	$0.4°$
$5\mu l + 4\mu l - 4\mu l$	$110.4°$	$0.8°$	$97.3°$	$0.7°$
$6\mu l + 2\mu l - 2\mu l$	-	-	-	-

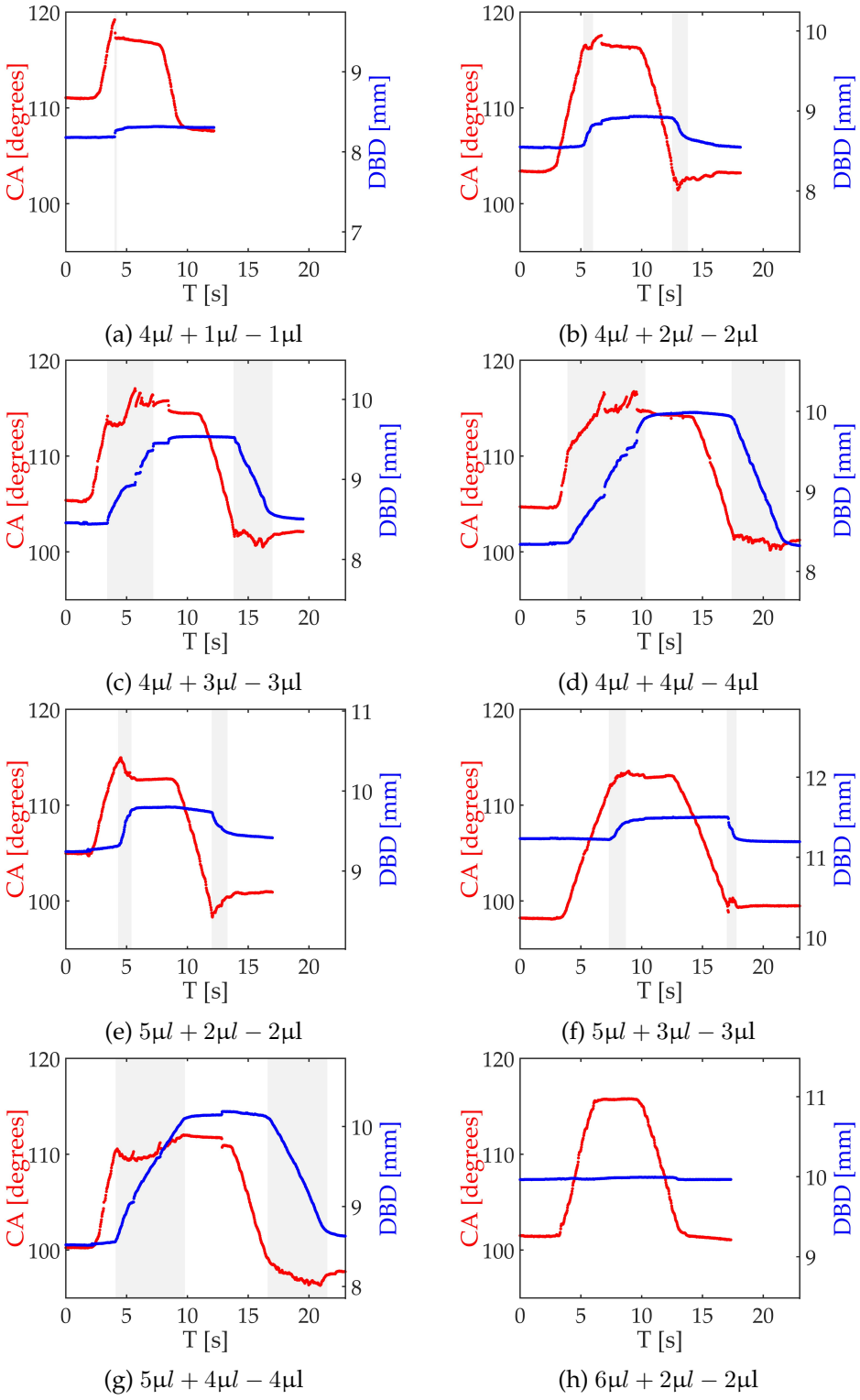

(a) $4\mu l + 1\mu l - 1\mu l$

(b) $4\mu l + 2\mu l - 2\mu l$

(c) $4\mu l + 3\mu l - 3\mu l$

(d) $4\mu l + 4\mu l - 4\mu l$

(e) $5\mu l + 2\mu l - 2\mu l$

(f) $5\mu l + 3\mu l - 3\mu l$

(g) $5\mu l + 4\mu l - 4\mu l$

(h) $6\mu l + 2\mu l - 2\mu l$

FIGURE 3.3: CA measurements by sessile drop with needle in for untreated FEP. Different drop volumes of small size used for estimating ACA and RCA. The shaded areas are when the DBD is changing, thus when the drop is advancing or receding, i.e. the time of interest when reading off the CA. At the time when these measurements were performed, the instrument was not calibrated correctly. The exact DBD value is therefore incorrect. Still, it is useful since the interesting part is in what time period the DBD is changing, which is not affected by the lack of calibration.

3.1.3 Execution of experiments - big drops

After further investigations of methods for measuring the CA of hydrophobic surfaces, the work by Korhonen et al. was discovered, also dealing with surfaces with high CAH [26]. According to their model, one crucial parameter to get right is the volume injected and withdrawn from the drop. If one know the magnitude of ACA and RCA, they have proposed a model for finding the adequate amount of water to use. If the ARCA is not known, some test experiments should be performed to figure this out.

Two models are presented to estimate how much water is required when the drop is at it's largest, in order to reach the RCA before the drop is less than 5 µl. One model, named spherical cap approximation performs well for $CA < 120^\circ$ or small CA hysteresis. This is not the case for the nano-structure FEP. The other model, Laplace-Young model, is therefore a better choice. It is solved by integrating the Laplace-Young equation [26].

A few experiments were conducted where injected and withdrawn water was 50 µl to 100 µl. Now the ACA seemed to be about 120° and the RCA about 20°. Using these values in the model proposed by Korhonen et al., the amount of water that should be injected and withdrawn, is about 100 µl or even greater. Some volumes were tested, in the range 60-180 µl. The result of these experiments are presented in figure 3.4.

Interpreting the Young-Laplace model (figure 4c in Ref. [26]) with these values implies a drop volume in excess of 100 µl should be used. To verify the choice of drop size, an experiment was conducted, where seven measurements was performed, each with different drop size. The result shown in figure 3.4 illustrates the importance of a big enough drop. In figure 3.4d, the 60 µl-drop never reaches a maximum and stable CA, while the volume still increases. Moreover, the minimum reached CA for the 60 µl-drop only reached 33°, which is very far from the larger drops. For the drops of volume 120 - 180 µl, they all reach a minimum CA within $10 \pm 2^\circ$, hence the RCA appears not to decrease significantly by increasing the volume above 120 µl. The minimum CA for all drop volumes in figure 3.4 are listed in table 3.2.

Another detail to notice about the experiment is the stability of the estimated volume in figure 3.4. For the drops in the range 60 - 100 µl, the plot of volume as a function of time, is smooth and linear during the injection, the 30 second break in the middle, and during the withdrawal of water in the end. As the volume increases above 100 µl, the plotted estimate of the volume deviates increasingly from a smooth and linear plot.

The requirements for obtaining reliable measurements (stable CA while drop expands and contracts on surface) of the RCA was not fulfilled for the experiments conducted on FEP etched by recipe C5 (figure 3.4). Other recipes had shown similar wetting properties with great drop-surface adhesion, hence this method was not suited for the samples fabricated for this work.

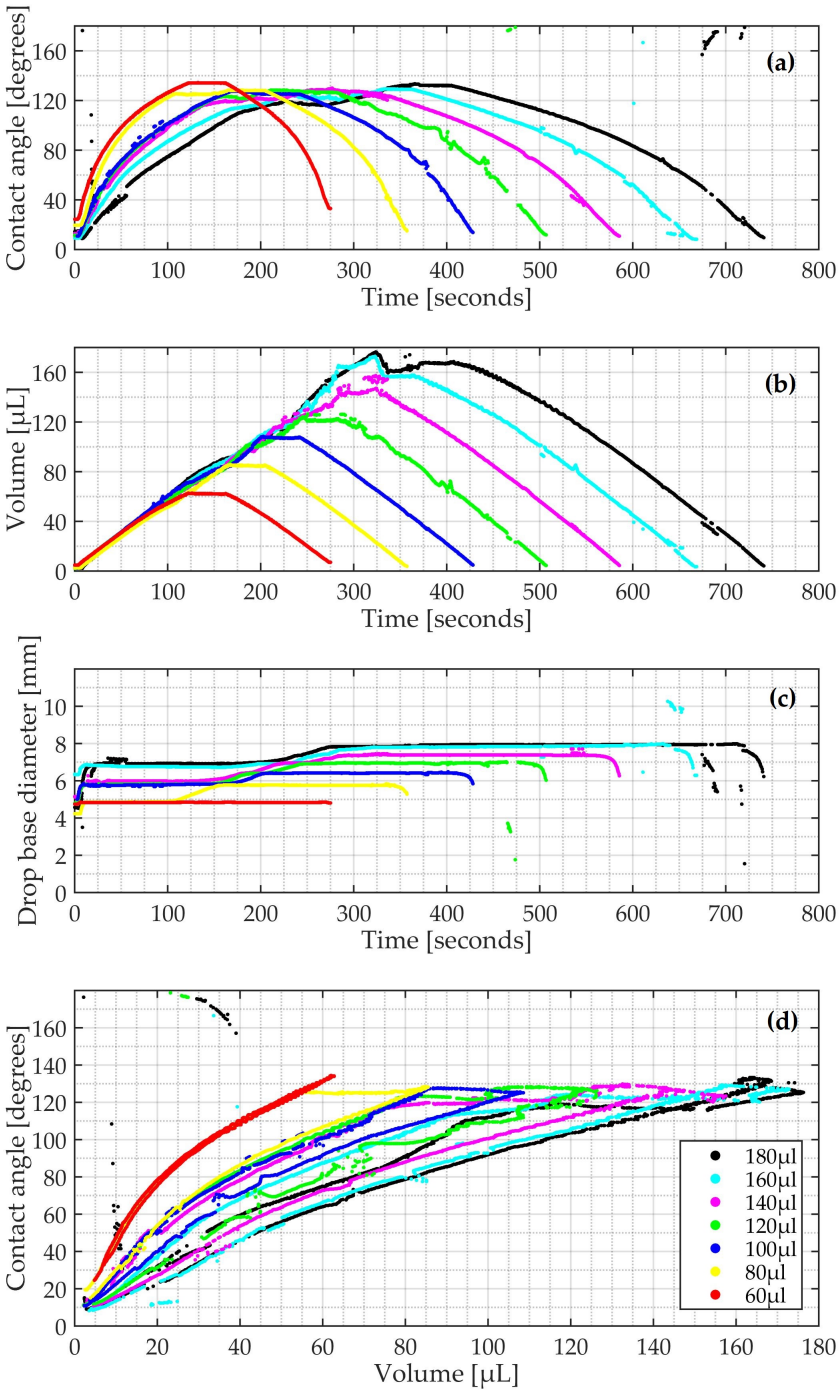

FIGURE 3.4: CA measurements performed on FEP etched with recipe C5. DI water injected/withdrawn at 0.5 µl/s. After injection, there is a 30 second break before withdrawal of water begins. Color with corresponding volume in the legend in (d) is the same for (a), (b) and (c).

TABLE 3.2: Minimum CA in figure 3.4b after withdrawing water from the drop.

V_{max}	60µl	80µl	100µl	120µl	140µl	160µl	180µl
CA_{min}	33°	15°	14°	12°	11°	8°	10°

3.2 Untreated FEP

Wetting properties has been analyzed on untreated FEP. When preparing FEP films of suitable size, the FEP has been rinsed in isopropanol and deionized water like the samples being etched. A sample was imaged by SEM, and can be seen in figure 3.5. When conducting the CA experiments, the film was rinsed in deionized water one more time.

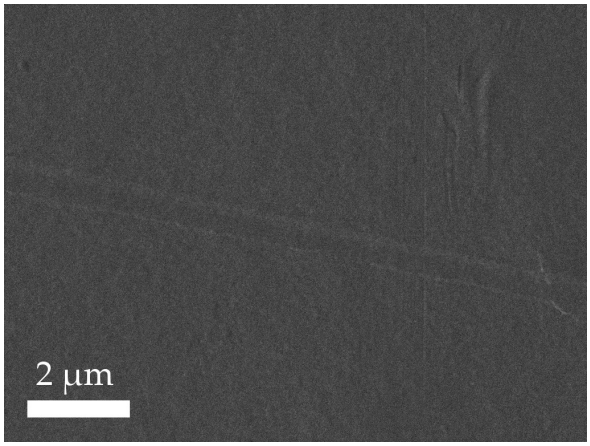

FIGURE 3.5: SEM image of untreated FEP.

3.2.1 Wetting properties

Five experiments were conducted on untreated FEP. The drops rolled off at α_c = 9 $\pm$ 1°, which comply with ROA reported in Ref. [7]. Both ACA and RCA where measured to be slightly larger than Helseth and Guo reported in Ref. [32] (θ_a = 111 $\pm$ 2°, θ_r = 95 $\pm$ 2°). This difference is of the same order of magnitude as the difference in CA that the two algorithms, Ellipse fitting and Polynom fitting, gives in SCA20, hence being a likely explanation for this difference.

TABLE 3.3: Measured and calculated properties of untreated FEP. [1]F_{pin} is calculated by equation 2.14 presented in subsection 2.4.2.

α_c [°]	9 ± 1
θ_a [°]	118 ± 2
θ_r [°]	102 ± 2
$\Delta\theta$ [°]	16 ± 3
F_{pin} [μN]	110 ± 10
F_{pin} [μN][1]	114 ± 19

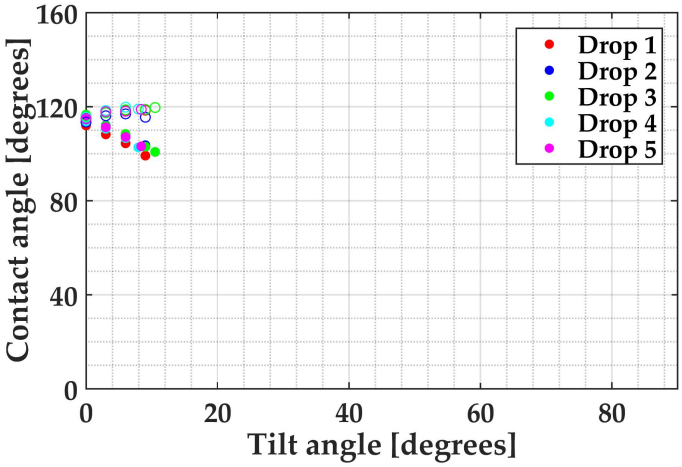

FIGURE 3.6: ARCA measurements by tilted plate method for untreated FEP. As the sample holder is tilted, measurements of the CA on both edges of the drop is done for every 3° the sample is tilted. Eventually, the drop will roll off, and a last measurement of the CAs are done. At the most extreme tilt just before the drop starts to roll, the CAs correspond to ACA (empty circle) and RCA (filled circle). A more thorough explanation of ACA and RCA in a tilted plate setup is given in conjunction with figure 2.16a. Drop volume: 70 µl.

3.3 Etch recipe A

The parameters used for this recipe is found in table 2.1. This is the same parameters as Helseth and Guo used in Ref. [7].

3.3.1 SEM images and structure characterization

In figure 3.7, one can see how the structures develop as the etch time increases. The structure geometry is easier to interpret when imaged at an angle. In figure 3.7f, a sample etched for 5 minutes is imaged at $45°$. The shape of the structures are looking like granules or spheres.

Analysis of the structures and their size distribution is presented in figure 3.9. Calculated mean and standard deviation of the structure diameter (by equation A.3 and A.4) is presented in table 3.4. The structure density is presented in the same table. The image used for this analysis contains no irregular structures like that in figure 3.8. Only a few granules having a diameter approximately 2-3 times as large as the majority of the structures are present in the image.

3.3.2 Wetting properties

CA measurements by the tilted plate method was conducted on two A5 samples with different appearance after etching. In the inset images in figure 3.10, one can see the difference in how the two films reflect light. The plots show the CA for both sides of the drop as it is tilted. The empty circles are the CA at the lower edge of the drop, the filled circles are the upper edge of the drop. At the critical tilt angle (α_c, the measurement at the highest tilt angle in figure 3.10), just before the drop starts to roll, the empty circle correspond to θ_a, and the filled circle correspond to θ_r (for details on this, see figure 2.16a with explanation). This experiment was repeated five times in order to highlight the repeatability of the measurements by calculating mean and error.

TABLE 3.4: Measured and calculated properties of FEP etched by recipe A5. Weight measurements are missing for this recipe. The diameter refers to the diameter of the granules on the surface. The density refers to the number of granules per square micro meter. Wetting properties are represented by calculated mean and standard deviation from five experiments by the tilted plate method, all with 70 µl drops of deionized water.

	Fig. 3.10a (clear)	Fig. 3.10b (spots)
$\%\Delta m$	-	-
Etch rate [nm/min]	-	-
Diameter [nm]	100 ± 40	-
Density [µm^{-2}]	63	-
α_c [°]	44 ± 4	37 ± 9
θ_a [°]	131 ± 1	133 ± 10
θ_r [°]	51 ± 2	68 ± 4
$\Delta\theta$ [°]	80 ± 3	65 ± 10
F_{pin} [µN]	480 ± 30	410 ± 90

From more thorough investigations of areas with spots for recipe C (see section 3.5.1), the results indicate that these areas consists of structures of irregular geometry and generally greater size than the areas that do not reflect light in the same way. If structures of greater size is to be the reason of the reflections observed, this comply with the phenomena of structural reflections due to structures of similar size, or somewhat smaller, than the wavelength of visible light [33] [34]. The order of magnitude of the wavelength of visible light is 400 nm $\leq \lambda \leq$ 700 nm, while the regular, fine granules resulting from recipe A5 has a diameter of d = 100 $\pm$ 40 nm. The cone shaped structures in figure 3.8a has a diameter of approximately 400-500 nm, being in the lower range of the wavelength of visible light, and possibly being the cause of blue light reflected from some spots.

The presence of spots reflecting light, is the only observed difference between the two samples in figure 3.8. Hence, this physical difference is probably one cause of the deviating wetting properties observed for the two samples (displayed in table 3.4).

The most obvious difference when looking at the plots in figure 3.10, is the repeatability of the measurements. All three parameters measured, CA on both sides and the angle of which the drop roll off the sample, is deviating between the five drops to a higher degree for the sample with spots, thus resulting in a greater error in the mean values calculated for ACA and ROA, and to some degree for RCA. One reason for the big error is due to the large ROA for drop 3, which deviates significantly from the 4 other drops which rolls off at 10° to 20° less. Such big deviations in one measurement in a small set of experiments makes a quite big impact on the mean and error. If more experiments had been conducted, it would be confirmed if drop 3 was only one exception, thus resulting in a smaller error, or if there really is a big span in the sample's performance.

The ACA is fairly similar for both samples, even though the sample with spots has an error of approximately 8% of the calculated mean. The RCA at the other hand is evidently larger for the sample with spots, hence resulting in a smaller CAH.

A quite steep inclination ($44 \pm 4^\circ$) was needed for the drops to roll off the sample. When the drops still stick to the sample until a split second before it rolls off, a significant pinning force (illustrated in figure 2.16b) between the FEP and drop is present, F_{pin} = 480 $\pm$ 30 µN (calculated by equation 2.13).

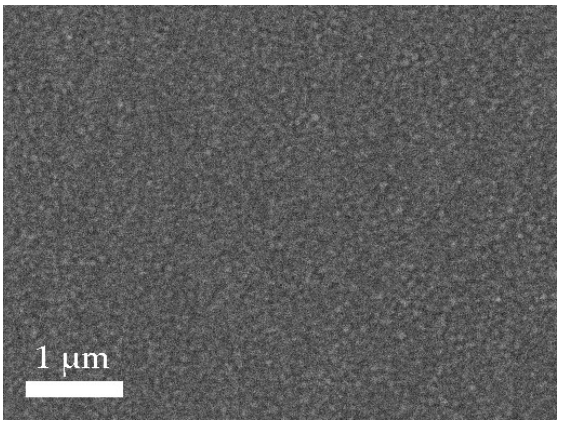

(a) Etch time: 1 minutes.

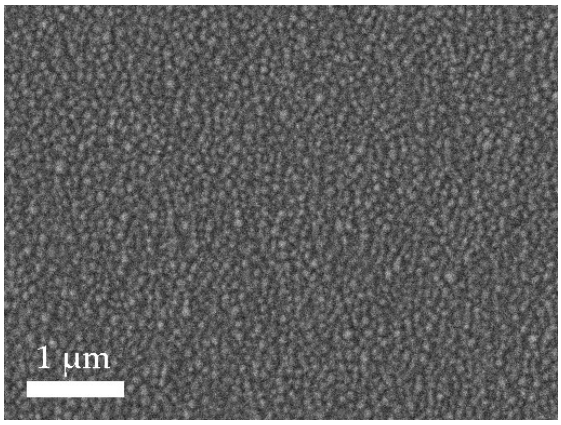

(b) Etch time: 2 minutes.

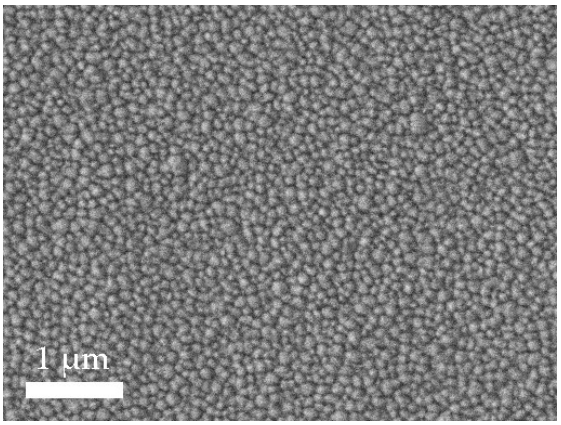

(c) Etch time: 3 minutes.

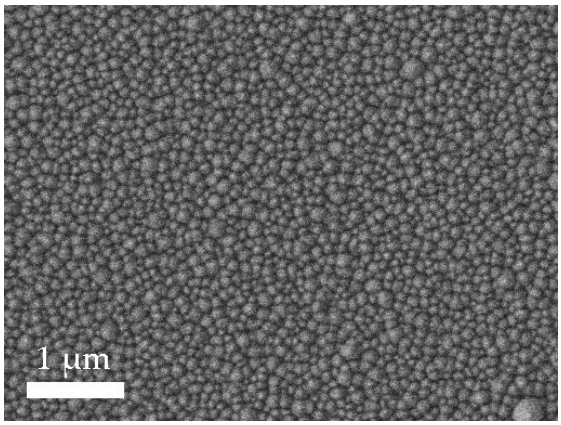

(d) Etch time: 4 minutes.

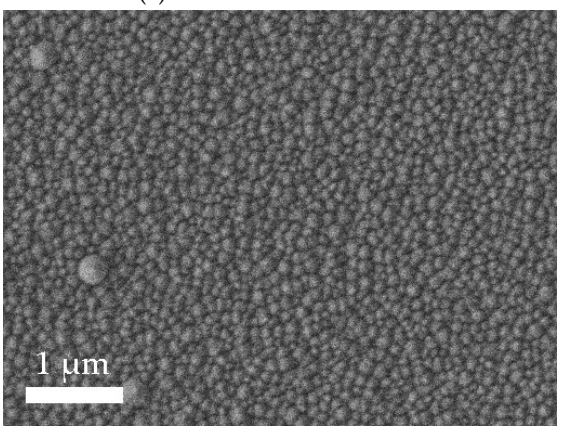

(e) Etch time: 5 minutes.

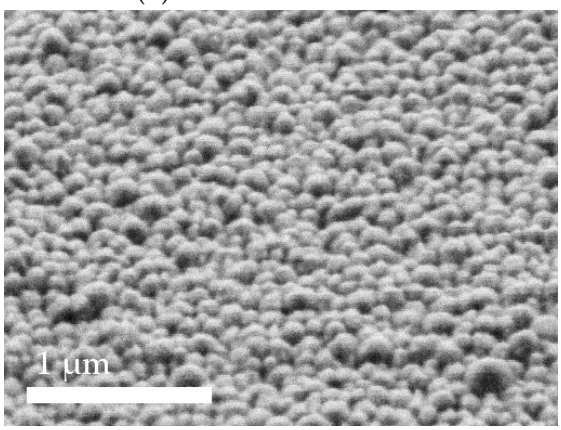

(f) Etch time: 5 minutes. Imaged at 45°.

FIGURE 3.7: SEM image of FEP etched by recipe A. The difference in brightness of the images (especially (c)) is not due to the differences in the sample, but rather inconsistency of the SEM operator capturing the images.

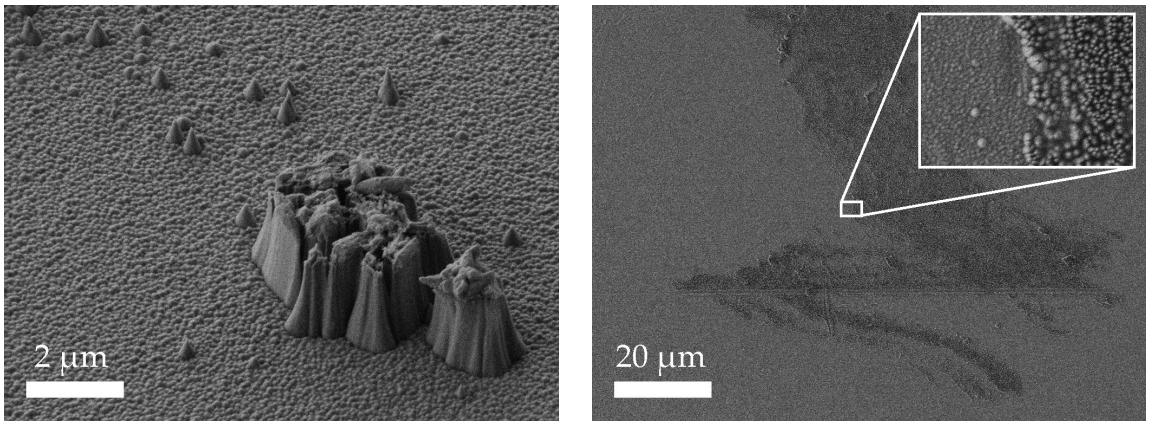

(a) Irregular structures imaged at $45°$. Recipe A5. (b) Irregular structures. Recipe A2.

FIGURE 3.8: SEM image of irregular structures resulting from recipe A. The majority of the surface looks like the small bumps/granules in figure 3.7f

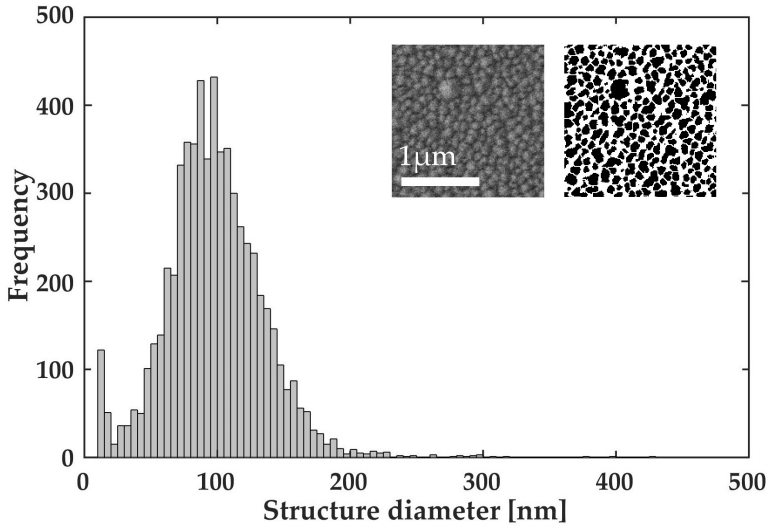

FIGURE 3.9: Diameter distribution of structures on A5 sample. The inset is part of the analyzed image, both the original and the 1 bit converted version. $d = 100 \pm 40$ nm.

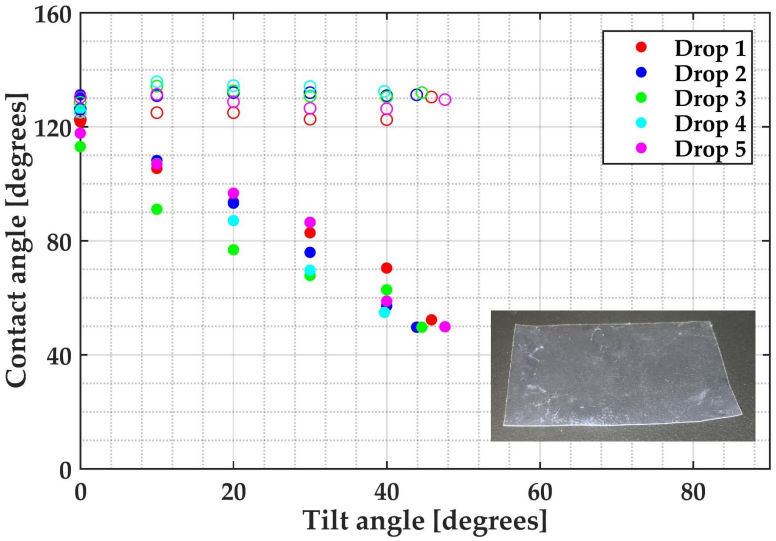

(a) Little light reflected in the sample.

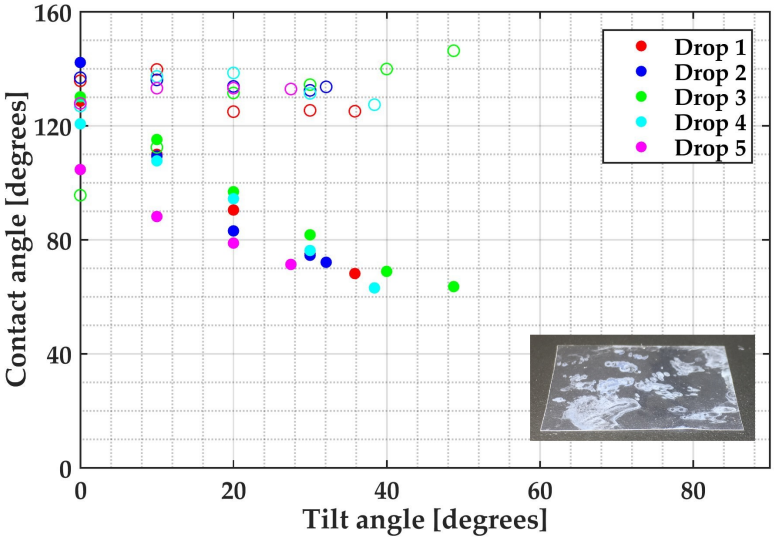

(b) Spots on the sample reflecting light.

FIGURE 3.10: ARCA measurements by tilted plate method for A5 sample. Inset images is of the sample used for the experiments. As the sample holder is tilted, measurements of the CA on both edges of the drop is done for every 10° the sample is tilted. Eventually, the drop will roll off, and a last measurement of the CAs are done. At the most extreme tilt just before the drop starts to roll, the CAs correspond to ACA (empty circle) and RCA (filled circle). A more thorough explanation of ACA and RCA in a tilted plate setup is given in conjunction with figure 2.16a. Notice drop 4 rolls off earlier than the other drops in figure (a). Drop volume: 70 µl.

3.4 Etch recipe B

Recipe A resulted in granule looking structures. It was desired to obtain structures with geometry of hairs or cones. The effect of CF_4 was then investigated by reducing the amount of CF_4 in the chamber by a half. This altered gas composition was named recipe B. Detailed settings are found in table 2.1. One sample was weighed before and after it was treated by RIE. The results are displayed in table 3.5.

TABLE 3.5: Weight measurements of a B5 sample. The scale used for the measurements has reproducibility of 0.1 mg.

Before RIE [mg]	13.0
After RIE [mg]	12.0
Δm [mg]	1.0
$\%\Delta$m	7.7
Etch rate [nm/min]	385

3.4.1 SEM images and structure characterization

The structures, both shape (figure 3.11), size (figure 3.12) and density, are quite similar to the structures resulting from recipe A5 (figure 3.7f). Calculated mean and standard deviation of the structure diameter (by equation A.3 and A.4) is presented in table 3.6. The structure density is presented in the same table.

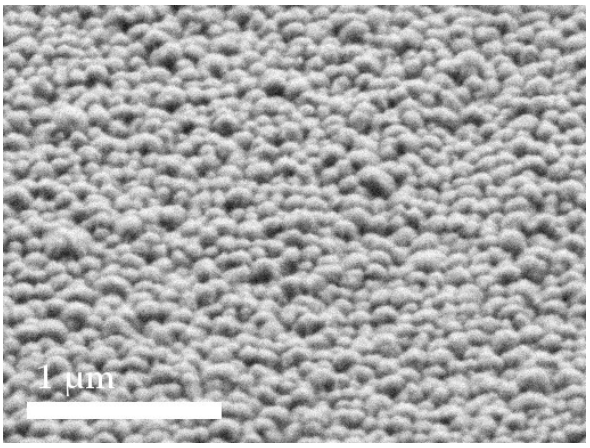

FIGURE 3.11: SEM image of FEP etched by recipe B5, imaged at 45°.

3.4.2 Wetting properties

Wetting properties (figure 2.15) resulting from recipe B5 are also quite similar to that of recipe A5. This indicates that changing the gas flow of CF_4 from 30 SCCM to 15 SCCM, did not change the etch process of FEP by a significant amount.

TABLE 3.6: Measured and calculated properties of FEP etched by recipe B5. The diameter refers to the diameter of the granules on the surface. The density refers to the number of granules per square micro meter. Wetting properties are represented by calculated mean and standard deviation from five experiments by the tilted plate method, all with 70 µl drops of deionized water.

%Δm	7.7
Etch rate [nm/min]	385
Diameter [nm]	100 ± 30
Density [μm^{-2}]	68
α_c [°]	46 ± 4
θ_a [°]	127 ± 2
θ_r [°]	52 ± 8
$\Delta\theta$ [°]	75 ± 8
F_{pin} [µN]	490 ± 40

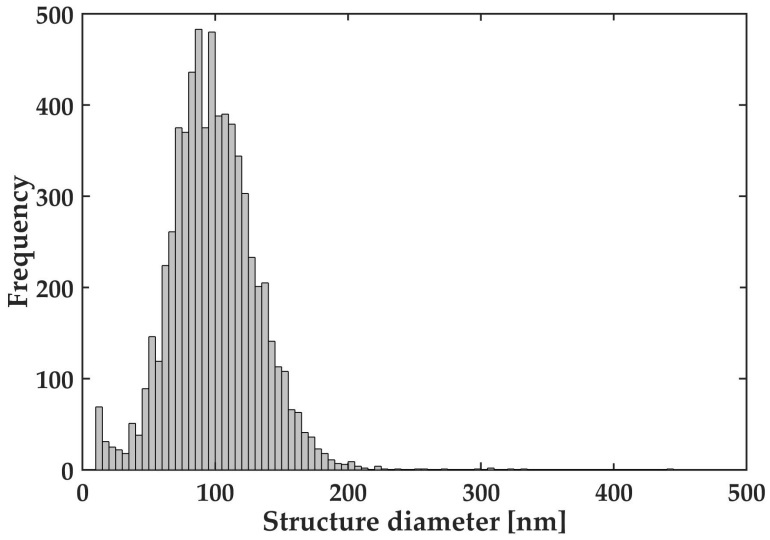

FIGURE 3.12: Diameter distribution of structures on B5 sample. d = 100 $\pm$ 30 nm.

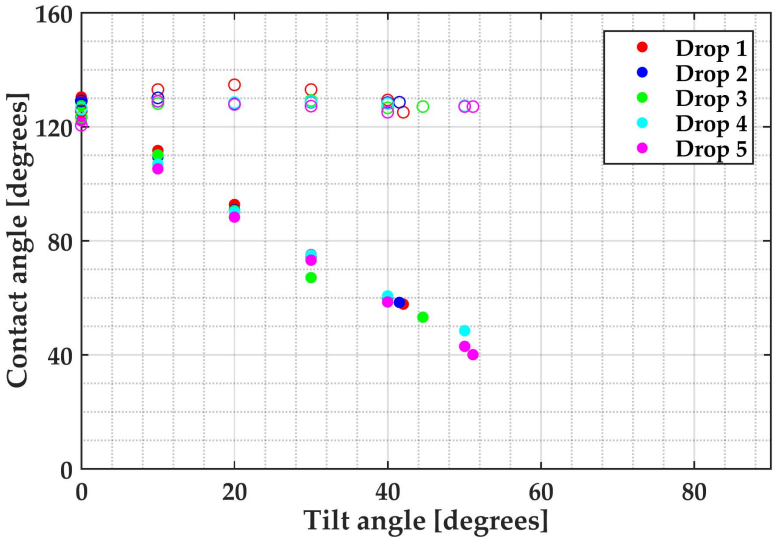

FIGURE 3.13: ARCA measurements by tilted plate method for B5 sample. Inset images is of the sample used for the experiments. As the sample holder is tilted, measurements of the CA on both edges of the drop is done for every 10° the sample is tilted. Eventually, the drop will roll off, and a last measurement of the CAs are done. At the most extreme tilt just before the drop starts to roll, the CAs correspond to ACA (empty circle) and RCA (filled circle). A more thorough explanation of ACA and RCA in a tilted plate setup is given in conjunction with figure 2.16a. Drop volume: 70 µl.

3.5 Etch recipe C

Reducing the amount of CF_4 let into the chamber did not make any significant change (recipe B), and was therefore removed completely in recipe C, to investigate if CF_4 had any influence on the etch process at all. When first looking at the results of recipe C5 in the SEM, the structures was so interesting that this recipe was investigated more in depth than the other recipes. This resulted in samples etched from 1 minute at the least, and up to 20 minutes at the most.

TABLE 3.7: Weight measurements of 4 samples etched by recipe C. The scale used for the measurements has reproducibility of 0.1 mg.

	C5	C10	C15	C20
Before RIE [mg]	12.4	11.8	11.5	16.1
After RIE [mg]	11.8	10.0	8.9	12.2
Δm [mg]	0.6	1.8	2.6	3.9
%Δm	4.8	15.3	22.6	24.2
Etch rate [nm/min]	242	381	377	303

3.5.1 SEM images and structure characterization

As seen in figure 3.15, the structures resulting from recipe C has a shape of cones, pillars or hair. Analysis of the structures and their size distribution is found in figure 3.16c and 3.16d. Calculated mean and standard deviation of the structure diameter (by equation A.3 and A.4) is presented in table 3.8. The structure density is presented in the same table.

As the etch time increases, the diameter of the structures stays relatively constant, while the height of the hairs increase (see figure 3.16). From 5 to 20 minutes, there is a clear decrease in structure density. Still, from the measurements that has been done, it seems like the structure density is higher for C15 than it is for C10 (see table 3.8). One would expect a somewhat linear relationship between structure density and etch time, and there might be multiple reasons for the results obtained from the measurements done here. As discussed for recipe A and in the following paragraph, the structures resulting from RIE treatment in this thesis work, is not uniformly spread over the surface with identical shape and size. Because of this, there might be local variations in structure density in the areas that the images are captured, thus not representing the mean structure density and size for the specific recipe and etch duration. Another explanation could be the method of counting structures. Both how a suitable threshold for binary conversion is determined, and the fact that the software is not always able to distinguish two close structures with the watershed function (details on the watershed function and determination of threshold are found in section 2.3.3).

After the FEP films have been etched, some films have areas with white spots, like the film in the inset in figure 3.14a. The clear area (A) and the white spotted area (B) was investigated in the SEM. It seemed like the general appearance of the surface in the clear area of the film, was uniform with only small deviations (see figure 3.14a). The white spotted area had generally a lot of patched areas of larger structures (see figure 3.14b). For more detailed images of deviating structures, the reader is referred to appendix F.

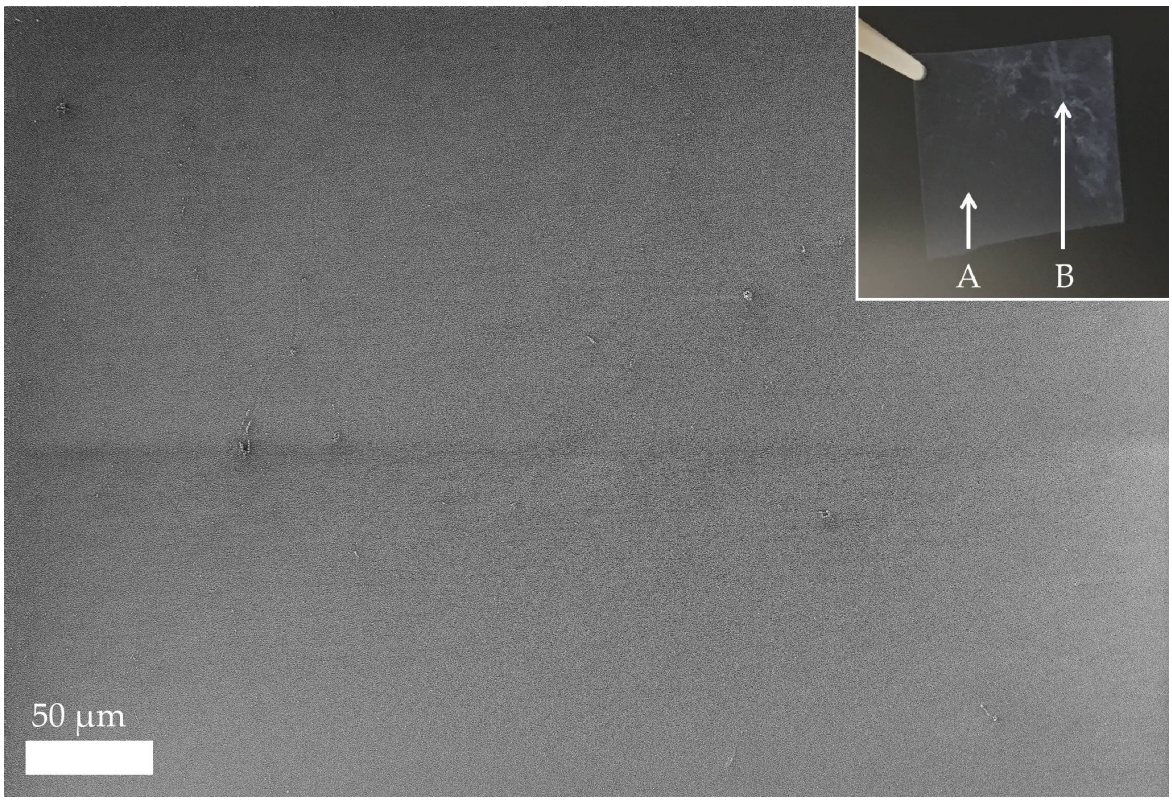

(a) SEM image from clear area (A in inset).

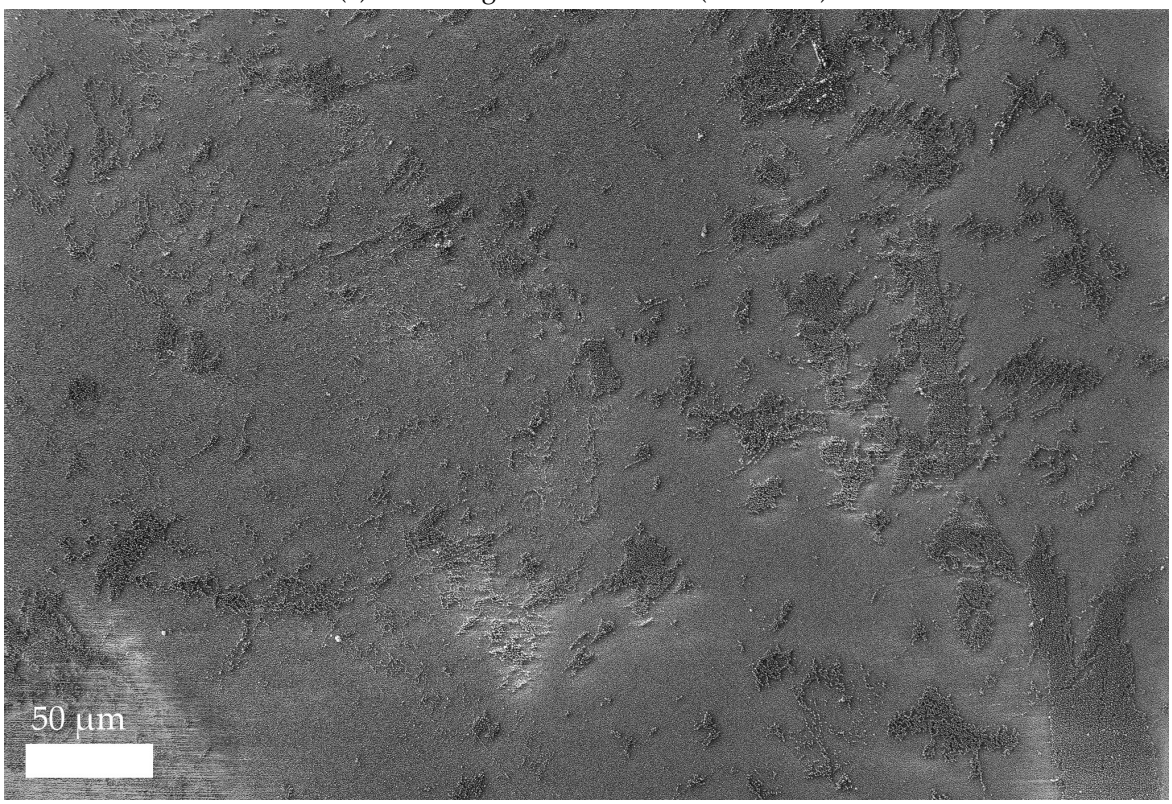

(b) SEM image from area with white spots (B in inset).

FIGURE 3.14: FEP etched with recipe C20. Like seen in the inset in (a), part of the film is clear, while another part appears with white spots. Area B (inset) has a lot of patches with larger structures (see (b)) than the fine structures (see (a)) that appears to be most common after RIE treatment.

TABLE 3.8: Measured and calculated properties of FEP etched by recipe C. The diameter refers to the diameter of the structures on the surface. The density refers to the number of structures per square micro meter. Wetting properties are represented by calculated mean and standard deviation from five experiments by the tilted plate method, all with 70 µl drops of deionized water.

	C5	C10	C15	C20
$\%\Delta m$	4.8	15.3	22.6	24.2
Etch rate [nm/min]	242	381	377	303
Diameter [nm]	110 ± 20	100 ± 30	110 ± 30	110 ± 30
Density [μm^{-2}]	55	30	35	27
α_c [°]	62 ± 3	61 ± 4	56 ± 5	65 ± 5
θ_a [°]	132 ± 3	133 ± 2	129 ± 7	144 ± 5
θ_r [°]	19 ± 4	28 ± 5	24 ± 2	20 ± 7
$\Delta\theta$ [°]	113 ± 5	105 ± 6	105 ± 8	124 ± 9
F_{pin} [µN]	600 ± 20	600 ± 20	570 ± 30	620 ± 30

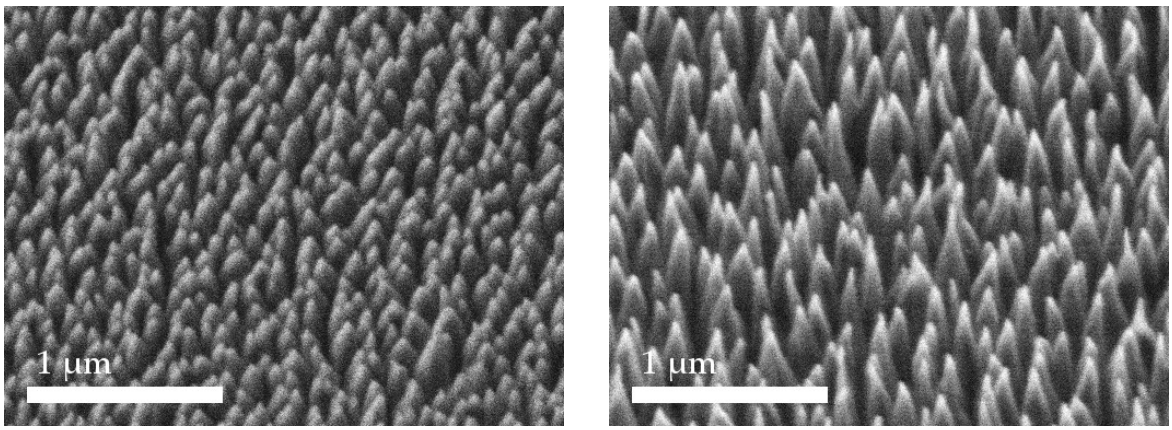

(a) Etch time: 5 minutes.

(b) Etch time: 10 minutes.

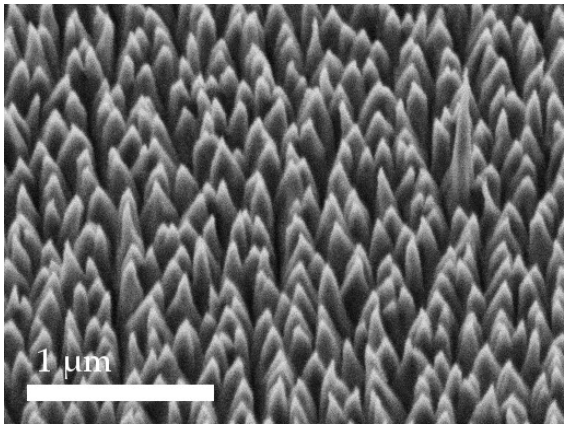

(c) Etch time: 15 minutes.

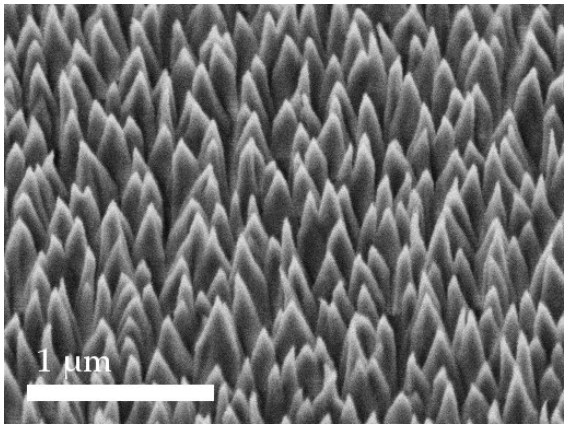

(d) Etch time: 20 minutes.

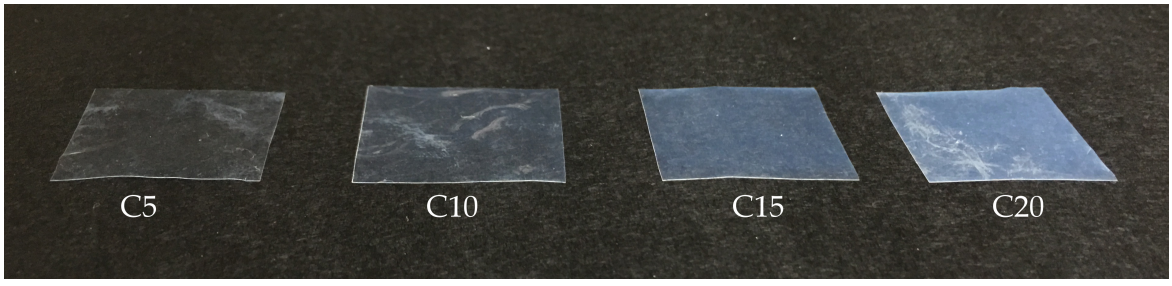

(e) Photograph.

FIGURE 3.15: Etch recipe C. SEM images (a-d) captured at 45°. Photograph (e) captured with natural light from behind the camera. Samples are placed on a piece of black paper to minimize light reflections in the surface. The appearance of the samples change as the etch time increases, where an increasing amount of light is reflected by the film.

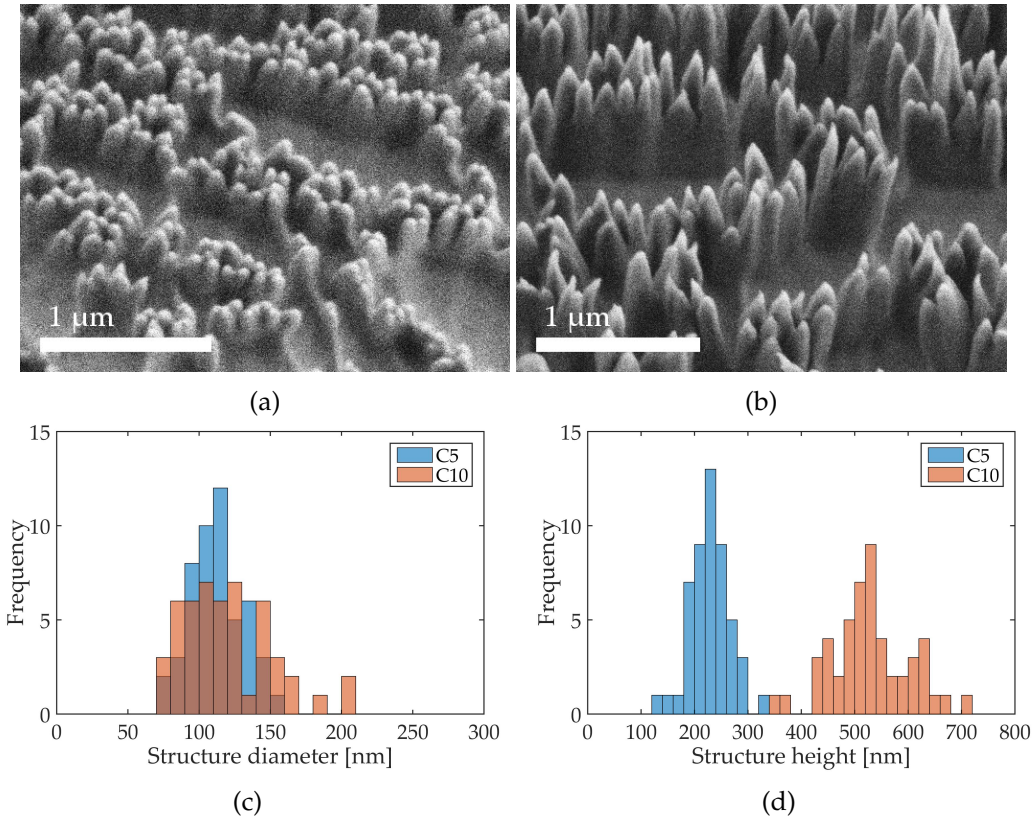

FIGURE 3.16: Structures resulting from recipe C. Imaged at 90°. (a) is etched for 5 minutes (C5), (b) is etched for 10 minutes (C10). Distribution of diameter (c) and height (d). 50 structures were measured in a cross sectional image for a C5 and C10 sample. How the structures were measured can be seen in appendix E. d_{C5} = 110 $\pm$ 20 nm, h_{C5} = 230 $\pm$ 40 nm, d_{C10} = 120 $\pm$ 30 nm and h_{C10} = 530 $\pm$ 70 nm.

3.5.2 Wetting properties

Even though the size changes of the structures for recipe C for 5 to 20 minutes, the wetting properties (see table 3.8 and figure 3.17, 3.18, 3.19 and 3.20) varies less. Except for ACA and ROA for the C20 sample, the four different samples with different etch duration performed quite similar for the experiments by the tilted plate method. Compared to untreated FEP, ACA has increased slightly and RCA has been reduced significantly. ROA is much larger due to the high F_{pin}.

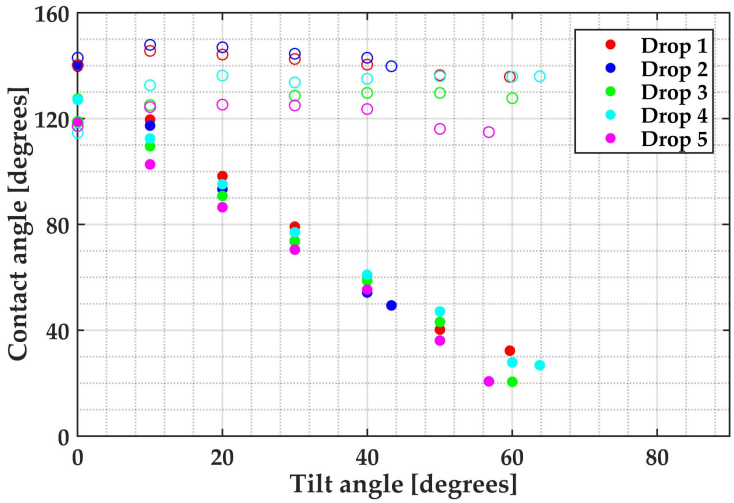

FIGURE 3.17: ARCA measurements by tilted plate method for C5 sample. Inset images is of the sample used for the experiments. As the sample holder is tilted, measurements of the CA on both edges of the drop is done for every 10° the sample is tilted. Eventually, the drop will roll off, and a last measurement of the CAs are done. At the most extreme tilt just before the drop starts to roll, the CAs correspond to ACA (empty circle) and RCA (filled circle). A more thorough explanation of ACA and RCA in a tilted plate setup is given in conjunction with figure 2.16a. Drop volume: 70 µl.

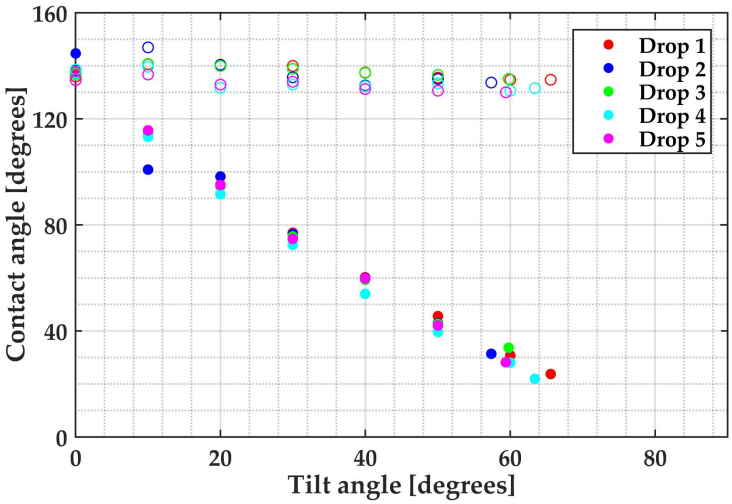

FIGURE 3.18: C10 sample. See figure 3.17 for more details.

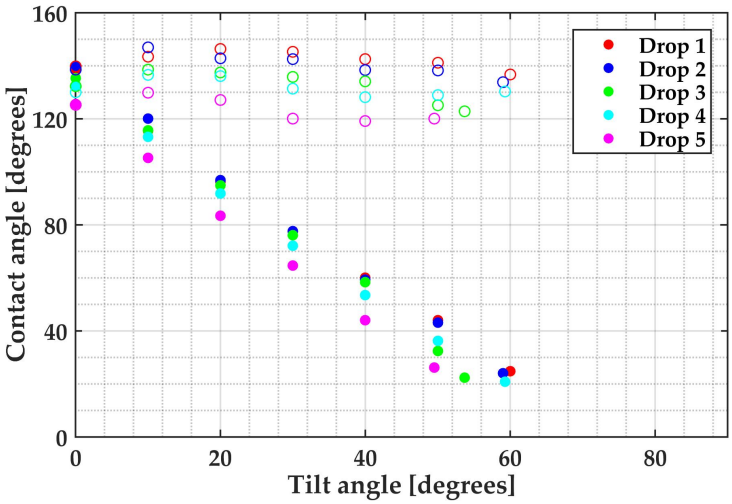

FIGURE 3.19: C15 sample. See figure 3.17 for more details.

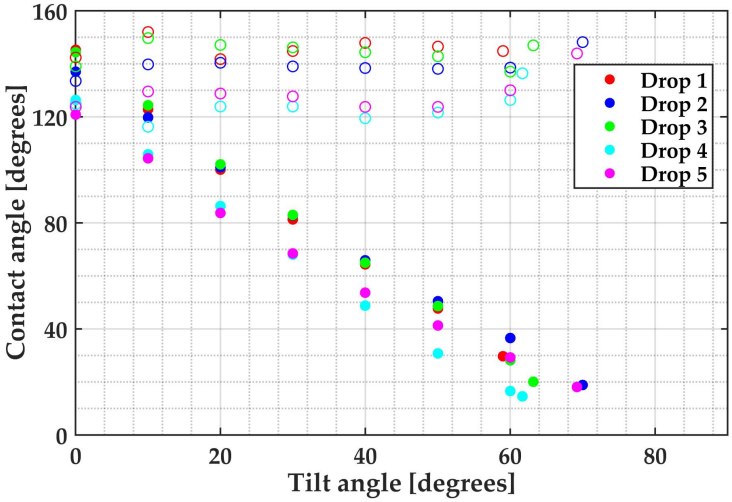

FIGURE 3.20: C20 sample. See figure 3.17 for more details.

3.6 Etch recipe D

Removing CF_4 clearly changed the etch process of FEP as seen in the results for recipe C. In recipe D, Ar is removed from the gas composition, and O_2 is now the only gas let into the chamber.

3.6.1 SEM images and structure characterization

The resulting structures (see figure 3.21) from etching with recipe D5 are somewhat similar to the structures resulting from recipe C5 (figure 3.15a), only a bit smaller. This is confirmed by the analysis in ImageJ, as the structure diameter of the D5 sample analyzed is smaller than the C5 sample analyzed ($d_{\mathrm{D5}} = 80 \pm 20$ nm, $d_{\mathrm{C5}} = 110 \pm 20$ nm). Also, D5 has more structures per area than C5 (74 μm^{-2} and 55 μm^{-2} respectively). The size distribution of the structures are illustrated in figure 3.22. Density and diameter of the structures are presented in table 3.9 along with wetting properties of FEP etched by recipe D5.

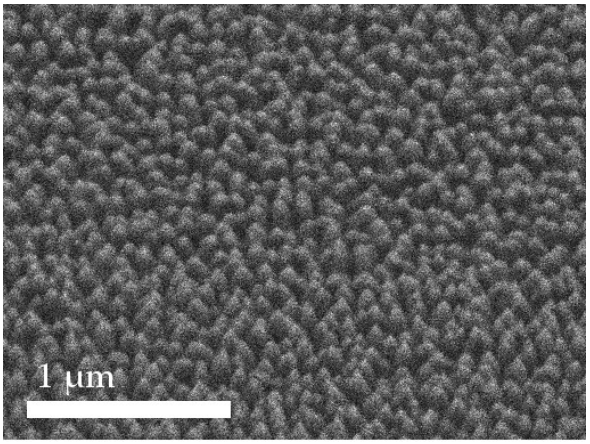

FIGURE 3.21: SEM image of FEP etched by recipe D5, imaged at 45°.

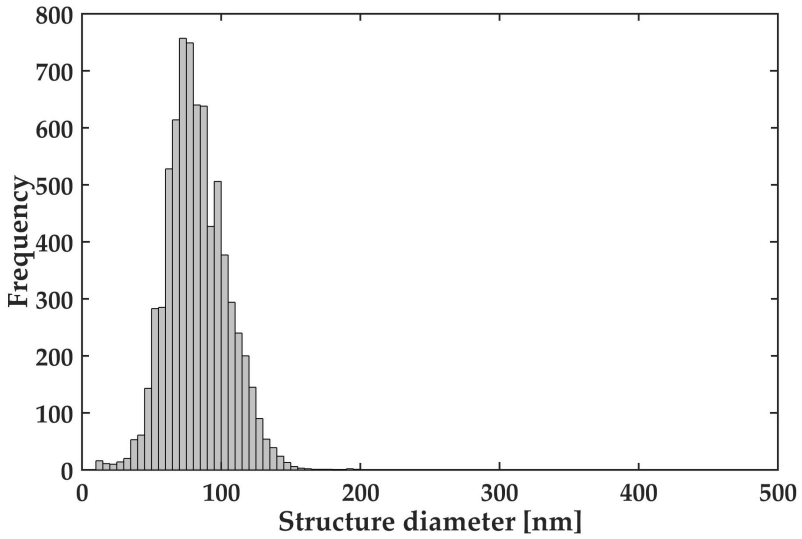

FIGURE 3.22: Diameter distribution of structures on D5 sample. d = 80 $\pm$ 20 nm.

TABLE 3.9: Measured and calculated properties of FEP etched by recipe D5. Weight measurements are missing for this recipe. The diameter refers to the diameter of the structures on the surface. The density refers to the number of structures per square micro meter. Wetting properties are represented by calculated mean and standard deviation from five experiments by the tilted plate method, all with 70 µl drops of deionized water.

$\%\Delta m$	-
Etch rate [nm/min]	-
Diameter [nm]	80 ± 20
Density [μm^{-2}]	74
α_c [°]	60 ± 2
θ_a [°]	129 ± 1
θ_r [°]	17 ± 2
$\Delta\theta$ [°]	112 ± 3
F_{pin} [µN]	600 ± 10

3.6.2 Wetting properties

The structure shape of FEP etched by recipe D5 appeared quite similar to the results of C5, just being a bit smaller in size. This is also the case for the wetting properties. All wetting properties with uncertainty presented in table 3.9 and 3.8 (for C5) overlap. Thus, the size difference for structures of recipe D5 and C5 does not affect the wetting properties of the surface.

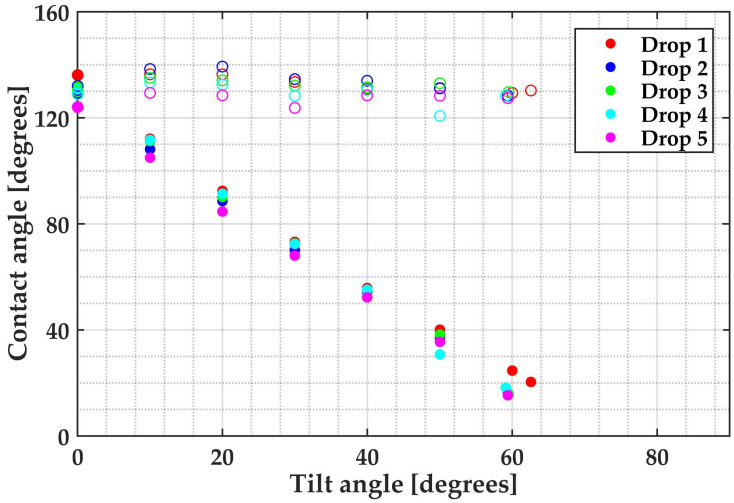

FIGURE 3.23: ARCA measurements by tilted plate method for D5 sample. As the sample holder is tilted, measurements of the CA on both edges of the drop is done for every 10° the sample is tilted. Eventually, the drop will roll off, and a last measurement of the CAs are done. At the most extreme tilt just before the drop starts to roll, the CAs correspond to ACA (empty circle) and RCA (filled circle). A more thorough explanation of ACA and RCA in a tilted plate setup is given in conjunction with figure 2.16a. Drop volume: 70µl.

3.7 Etch recipe E

Because of the similar results of recipe C (Ar and O_2) and D (O_2), the effect of Ar was investigated in recipe E, where Ar was the only gas used in the chamber during etching.

TABLE 3.10: Weight measurements of an E5 sample. The scale used for the measurements has reproducibility of 0.1 mg.

Before RIE [mg]	11.7
After RIE [mg]	10.8
Δm [mg]	0.9
%Δm	7.7
Etch rate [nm/min]	385

3.7.1 SEM images and structure characterization

The surface structures resulting from an argon plasma was fundamentally different from the structures resulting from recipe A-D. Like seen in figure 3.24, there are not bumps or hairs pointing out of the surface like the structures obtained with recipe A-D. The structures on the E5 sample in figure 3.24 looks more like elongated holes or ditches into the bulk material.

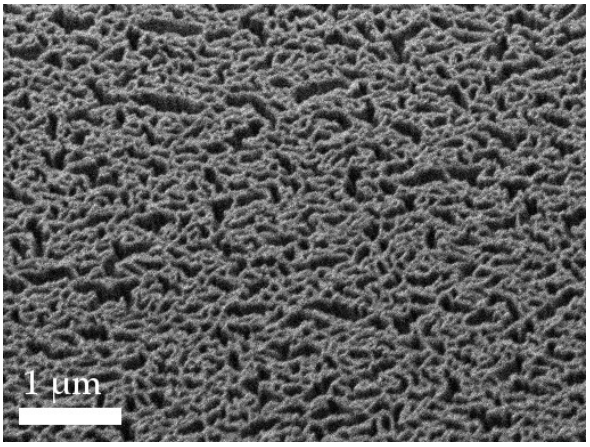

FIGURE 3.24: SEM image of FEP etched by recipe E5, imaged at 45°.

3.7.2 Wetting properties

Not only the surface geometry resulting from recipe E5 was very different from recipe A-D, also how water wetted the surface on E5 samples was also fundamentally different. This was first discovered when preparing an E5 sample for tilted plate experiments. When rinsing samples etched by recipe A-D, the water rolled off the sample when sufficient amounts of water accumulated on the surface. When the rinsing was stopped, multiple droplets where pinned individually to the surface. After shaking the sample a few times, most of the drops had fallen off. The E5 samples at the other hand, was totally covered with a thin film of water, even after shaking, the samples were still covered in water.

TABLE 3.11: Measured and calculated properties of FEP etched by recipe E5. Wetting properties are represented by calculated mean and standard deviation from five experiments by the tilted plate method, all with 70 µl drops of deionized water. *E5 samples wetted the surface differently from FEP etched by recipe A-D, and the films could not be rinsed short time in advance of the experiments. This is described in more detail in the text of subsection 3.7.2.

$\%\Delta m$	7.7
Etch rate [nm/min]	385
Diameter [nm]	-
Density [μm^{-2}]	-
α_c [°]	$47 \pm 9^*$
θ_a [°]	$90 \pm 14^*$
θ_r [°]	$13 \pm 5^*$
$\Delta\theta$ [°]	$77 \pm 15^*$
F_{pin} [µN]	$500 \pm 70^*$

If a drop was dispensed onto the surface while the thin film of water still covered the sample, the drop would just disperse all over the surface. Therefore, the film was carefully touched with a lab napkin to absorb water off the sample. It was not desired to wipe the samples to avoid mechanical damage to the surface structures, the samples was thus resting for a few minutes so the rest of the water could evaporate off the surface before conducting the experiment.

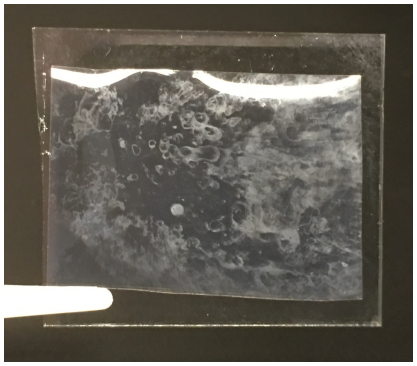

FIGURE 3.25: Photo of FEP etched by recipe E5, laying on glass.

All the FEP films etched by recipe E had white spots like the sample in figure 3.25. The tilted plate experiments was therefore conducted on an area with such spots. The results can be seen in figure 3.26. Like the experiments conducted on an A5 sample with spots (figure 3.10b), the measured values from each experiment varies, resulting in high standard deviation for the parameters measured. ACA is the parameter sticking out the most, having a mean of about 40° less than recipe A-D.

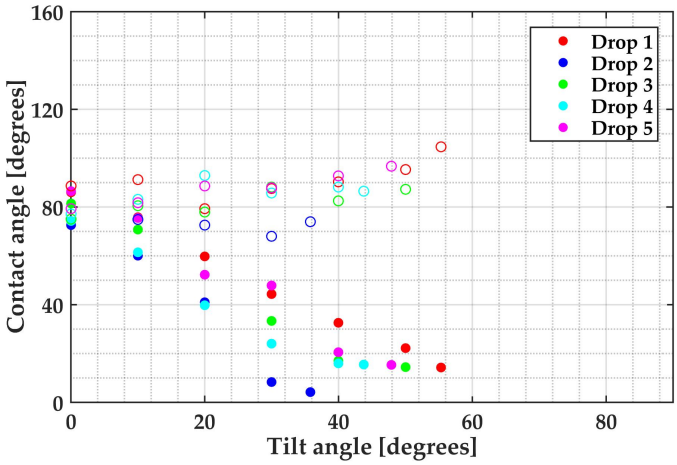

FIGURE 3.26: ARCA measurements by tilted plate method for E5 sample. As the sample holder is tilted, measurements of the CA on both edges of the drop is done for every 10° the sample is tilted. Eventually, the drop will roll off, and a last measurement of the CAs are done. At the most extreme tilt just before the drop starts to roll, the CAs correspond to ACA (empty circle) and RCA (filled circle). A more thorough explanation of ACA and RCA in a tilted plate setup is given in conjunction with figure 2.16a. Drop volume: 70µl.

3.8 Etch recipe C^x

Wohlfart et al. has reported etching of PET where the effect of chamber pressure was shown to have high significance for the size of the resulting nano-structures. At approximately 750 mTorr, one can barely catch the sight of any structure. As the pressure is lowered in steps, all the way to about 38 mTorr at the least, structures with increasing aspect ratio (*height*/*width*) develop on the surface [18].

It was investigated if lowering the chamber pressure would increase the aspect ratio for the resulting structures on FEP as well. This was first attempted with the same gas composition as recipe C, but changing the pressure from 10 to 1 mTorr. However, the Plasmatherm (RIE) was not able to obtain 1 mTorr for the gas flow rates used. The pressure was raised to 5 mTorr (recipe F, overview of recipes are found in figure 2.1), which the Plasmatherm managed to obtain without any gasses let into the chamber. When the gasses was let into the chamber, the pressure began to rise, and after 18 seconds, the pressure went outside some limit of the Plasmatherm, and the etch process was aborted.

The pressure was then raised to 100 mTorr (recipe G) instead, which worked fine for the Plasmatherm. The resulting structures had similar shape as for 10 mTorr (recipe C), but was smaller in size, which was also the case for Wohlfart et al. where the structure size decreased by increasing the chamber pressure [18].

Another attempt was made to etch at a lower pressure than 10 mTorr. The pressure that nearly worked (5 mTorr) was used, and the gas flow into the chamber was reduced by a half (recipe H) from the first attempt (recipe F). This process was able to run for the entire duration of 5 minutes. The resulting structures was similar to recipe C with doubled etch duration (10 minutes). Because both the chamber pressure and the gas flow was reduced compared to recipe C, the effect of reducing the gas flow was therefore investigated. This was done using the same settings as recipe C, but reducing the gas flow in four steps (recipe C^x). The gas flow is a fraction of the flow in recipe C: 1/2 for C^1, 1/4 for C^2, 1/8 for C^3, and 1/12 for C^4.

Because of the similarities of recipe G and H to other recipes (C for different etch duration), these recipes are not analyzed further in this chapter. An image of a G5 and a H5 sample is found in figure F.1 (in appendix F). The weight loss of the C^x recipes are displayed in table 3.12.

TABLE 3.12: Weight measurements of C^x5 samples. The scale used for the measurements has reproducibility of 0.1 mg.

Recipe	C^15	C^25	C^35	C^45
Before RIE [mg]	11.0	11.8	9.6	11.7
After RIE [mg]	10.4	11.0	9.2	11.0
Δm [mg]	0.6	0.8	0.4	0.7
$\%\Delta$m	5.5	6.8	4.2	6.0
Etch rate [nm/min]	273	339	208	299

3.8.1 SEM images and structure characterization

SEM images of the resulting structures from recipe C^x are shown in figure 3.27. $C^1$5 (a) has similar diameter and density of the structures as FEP etched by recipe C for 10-20 minutes. The appearance of the structures in the SEM images (compare figure 3.27a with figure 3.15b, 3.15c and 3.15d) is also looking the same. When the gas flow is reduced further (C^2, and especially C^3 and C^4), the appearance of the resulting structures change significantly. $C^3$5 and $C^4$5 appears much like the resulting structures from recipe E5 (compare figure 3.27e and 3.27f (imaged from above) with figure 3.24 (imaged at 45°)).

TABLE 3.13: Measured and calculated properties of FEP etched by C^x5 recipes. The diameter refers to the diameter of the structures on the surface. The density refers to the number of structures per square micro meter. Wetting properties are represented by calculated mean and standard deviation from five experiments by the tilted plate method, all with 70 µl drops of deionized water. *$C^2$5, $C^3$5 and $C^4$5 samples wetted the surface differently from FEP etched by recipe A-D and C^1, and the films could not be rinsed short time in advance of the experiments. This is described in more detail in the text of subsection 3.8.2.

	$C^1$5	$C^2$5	$C^3$5	$C^4$5
$\%\Delta m$	5.5	6.8	4.2	6.0
Etch rate [nm/min]	273	339	208	299
Diameter [nm]	100 ± 20	-	-	-
Density [μm^{-2}]	33	-	-	-
α_c [°]	63 ± 11	$73 \pm 7^*$	$54 \pm 4^*$	-
θ_a [°]	136 ± 4	$126 \pm 5^*$	$93 \pm 2^*$	-
θ_r [°]	25 ± 11	$20 \pm 5^*$	$10 \pm 3^*$	-
$\Delta\theta$ [°]	111 ± 12	$106 \pm 7^*$	$84 \pm 4^*$	-
F_{pin} [µN]	610 ± 60	$660 \pm 20^*$	$560 \pm 30^*$	-

3.8.2 Wetting properties

The way water wetted the surface of FEP etched by recipe $C^2$5, $C^3$5 and $C^4$5, is the same as experienced for FEP etched by recipe E5. For more details on this experience, see subsection 3.7.2. As the conduction of the experiments on these samples was difficult, and the method was changed at one point (not rinsing the films short time in advance of conducting the experiments), tilted plate experiments was not conducted for recipe $C^4$5, which appears much the same as E5 and $C^3$5 samples.

Measured wetting properties of C^x recipes etched for 5 minutes are shown in table 3.13. Just like the FEP etched by recipe $C^1$5 had the same appearance (shape and size) as FEP etched by recipe C10, C15 and C20, the measured wetting properties are quite similar. This is also the case for recipe C^3, having the same appearance as FEP etched by recipe E, and having a lot the same performance in the tilted plate experiments.

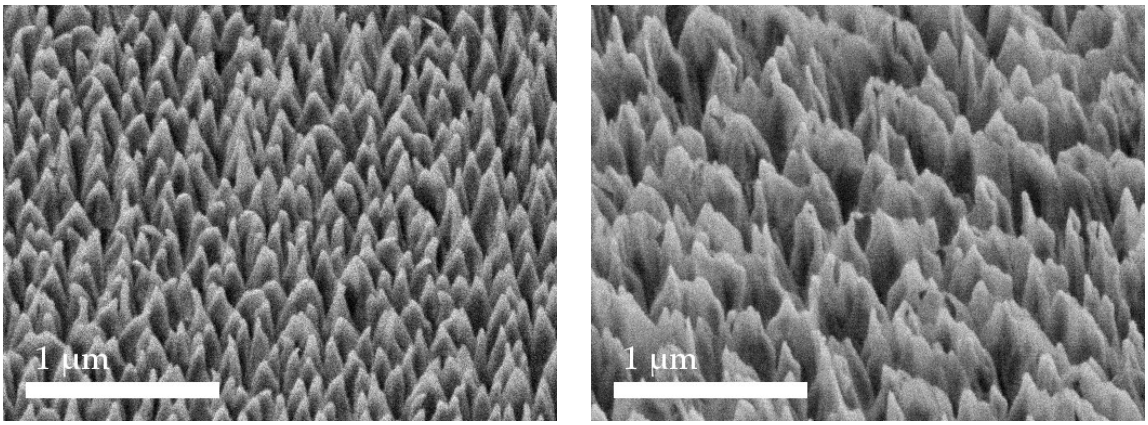

(a) Recipe $C^1 5$. (b) Recipe $C^2 5$.

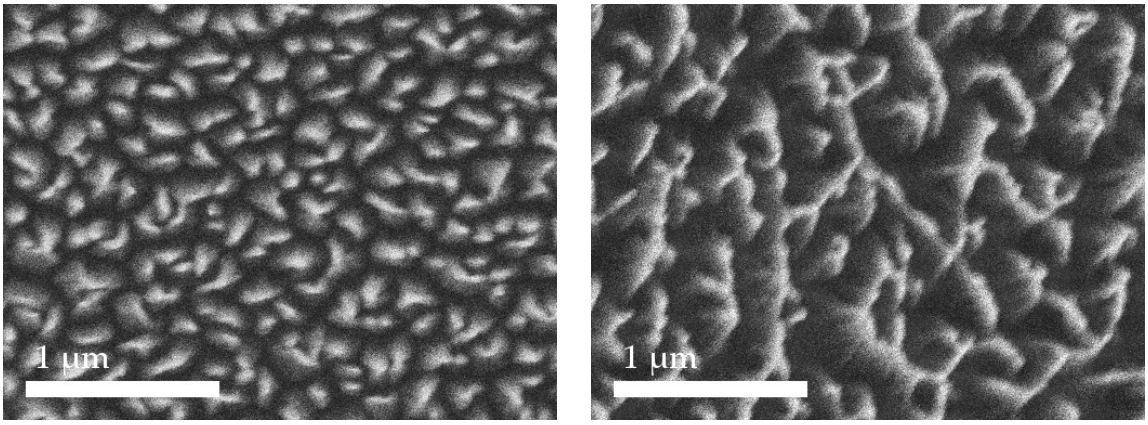

(c) Recipe $C^1 5$. (d) Recipe $C^2 5$.

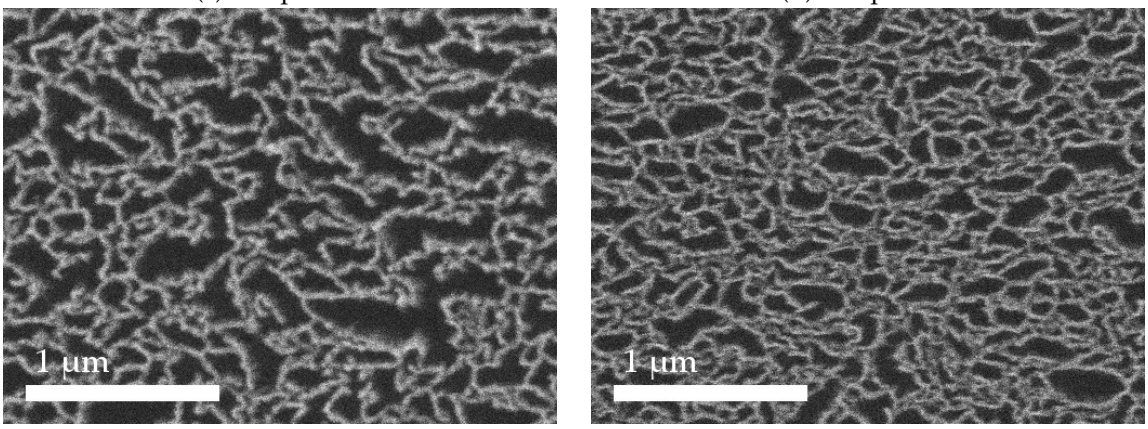

(e) Recipe $C^3 5$. (f) Recipe $C^4 5$.

FIGURE 3.27: SEM images of FEP etched by recipe C^x. (a) and (b) are captured at 45°.

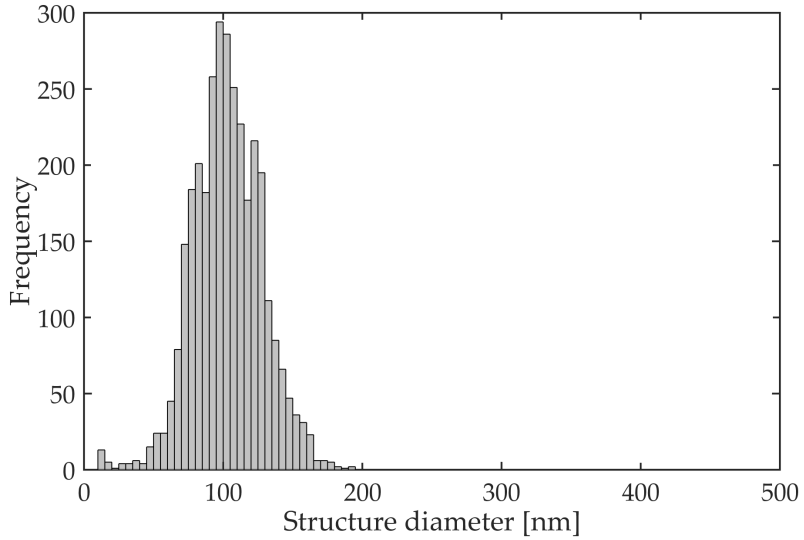

FIGURE 3.28: Diameter distribution of structures on $C^1$5 sample. d = 100 $\pm$ 20 nm.

3.9 Comparison of recipes

Until now, the etch recipes has been analyzed individually. In this section, they will be compared in different ways. Results from section 3.2 to 3.8 are summarized in table 3.14.

3.9.1 General observations

The FEP used for this work appears clear. After RIE treatment, most films are still clear. However, some films appear to have white stains or spots, like the films seen in figure 3.10b (inset image), 3.14a (inset image) and 3.25. Recall from section 3.5, that in areas with white stains or spots, it was found areas with larger structures than the majority of the FEP surface (observed by SEM). Areas with white spots were also wetted differently than clear areas (see figure 3.10). Different FEP films etched in the same process could end up differently, one film being mostly clear, another film being being partly covered in stains. No apparent condition, inducing spots on the FEP during etching, have been found. Yet, the FEP films not containing spots seems to get reproducible etch results.

3.9.2 Wetting on the nano-structured surfaces

The drop-surface adhesion force has been plotted for untreated and RIE treated FEP. F_{pin} has been calculated in two different ways. First, the adhesive force is calculated from analyzing the gravitational force acting on a drop at the critical angle (α_c) before it starts to roll or slide off the surface (equation 2.13). In addition, the adhesion force is calculated from the ACA and the RCA for a surface (equation 2.14). As seen in figure 3.29, the two methods conform quite well, even with the simplification of the drop width. As mentioned in the end of subsection 2.4.2, the actual drop width is not possible to measure with the experimental setup used during this work. Thus, the value used for w in equation 2.14 is the drop base diameter (*DBD*) before the sample is being tilted ($\alpha_c = 0°$). The large uncertainty for FEP etched by recipe E5 is due to the spreading of the measured ACA, RCA and ROA (see figure 3.26). As seen in figure 3.29, the drop-surface adhesion has increased by a factor of 5 - 6 for all the RIE treated surfaces.

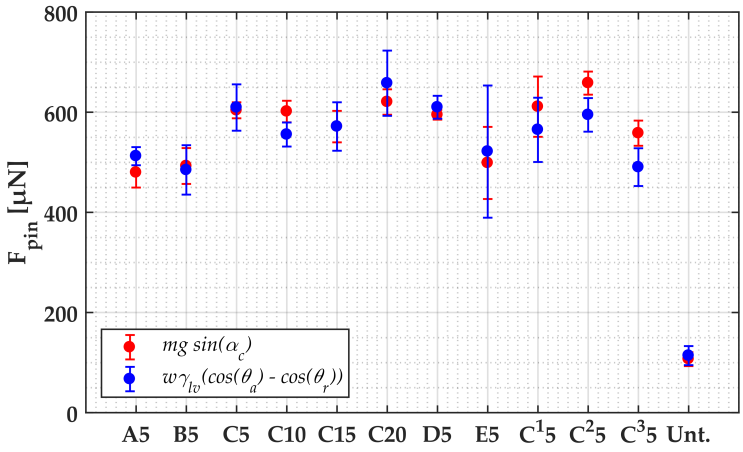

FIGURE 3.29: Adhesion force (F_{pin}) for untreated (Unt.) and RIE treated FEP (recipe name on x-axis). The red data are calculated from analyzing the gravitational forces acting on a pinned drop (equation 2.13). The blue data are calculated by means of CA measurements (equation 2.14).

When creating surface roughness (nano-structures) on FEP films, the CA was expected to increase and the ROA to decrease [7][35][36]. It was therefore unexpected that the nano-structured FEP films fabricated for this thesis work showed an increase in drop-surface adhesion. To better understand what could be the cause of the increased F_{pin}, this parameter has been plotted as a function of some different surface properties: as a function of the structure diameter (figure 3.30), structure density (figure 3.31) and of the CAH (figure 3.32).

There seem to be little correlation between the pinning force and the structure density in figure 3.30. However, the data points appears to be divided into two groups, one having $F_{\text{pin}} \approx 500$ μN (recipe A5 and B5), and the other group having $F_{\text{pin}} \approx 600$ μN. The first group is the films with structures looking like granules or spheres. The structure shape of the films having $F_{\text{pin}} \approx 600$ μN, are taller and more pointy, like hairs or cones. So, for the fabricated nano-structures in this work (only two categories of significant difference (spheres and hairs)), there seem to be a dependence for surface-drop adhesion on the shape of the structures.

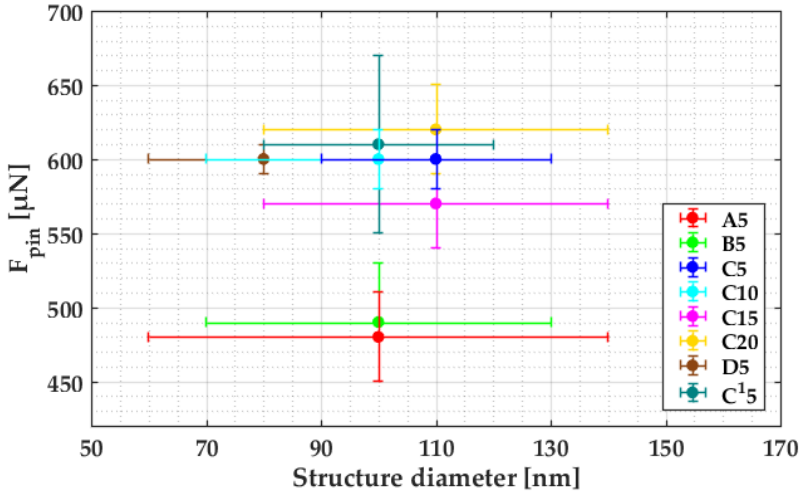

FIGURE 3.30: F_{pin} plotted as a function of the structure diameter for different etch recipes. The legend refers to the etch recipe used.

Also in figure 3.31, recipe A5 and B5 are found in their own area of the plot. For the rest of the recipes, F_{pin} is not changing much, even though the structure density ranges from 27 to 74 μm^{-2}.

In figure 3.32, F_{pin} is plotted as a function of CAH. The data points are a bit spread out, however, F_{pin} generally rises as CAH increases. This is especially obvious when paying attention to the position of untreated FEP, with much lower F_{pin} and CAH than the etched FEP films. One may also make a distinction between two groups of recipes. The first group of recipes resulting in structures with a shape like hair or spikes (C5-20, D5, $C^1$5 and $C^2$5). The second group resulting in structures looking like spheres (A5 and B5) and ditches or holes (E5 and $C^3$5). The first group has larger CAH and slightly higher F_{pin} than the second group.

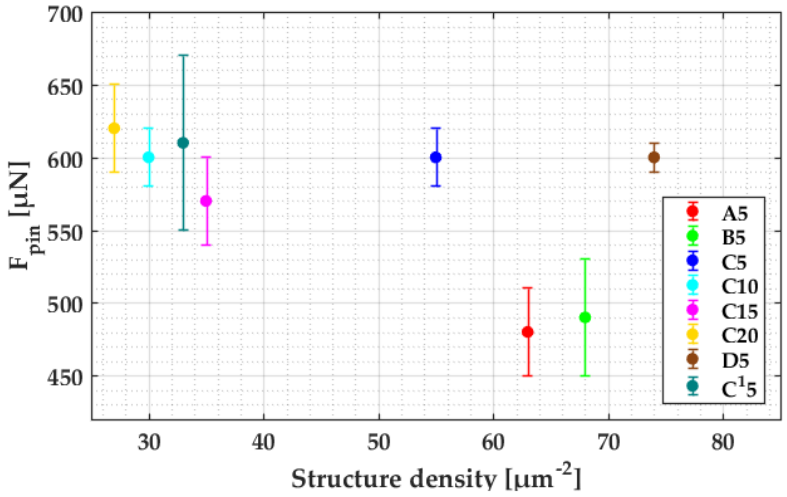

FIGURE 3.31: F_{pin} plotted as a function of the structure density for different etch recipes. The legend refers to the etch recipe used.

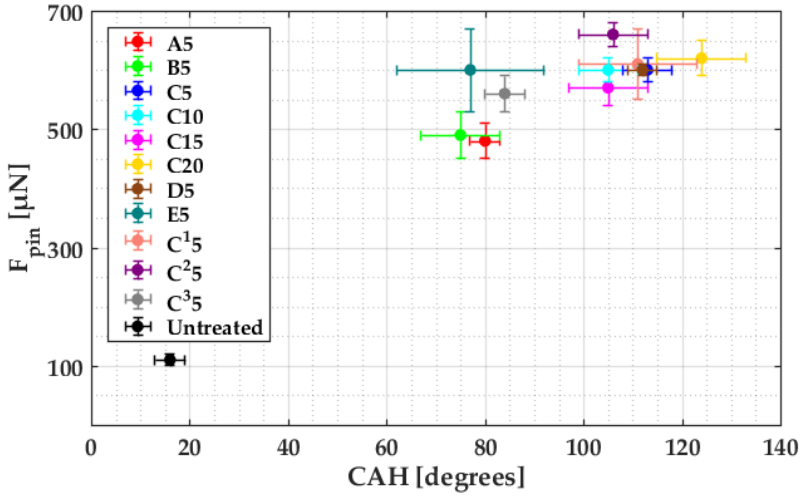

FIGURE 3.32: F_{pin} plotted as a function of the contact angle hysteresis (CAH) for different etch recipes. The legend refers to the etch recipe used.

TABLE 3.14: Measured and calculated properties for untreated (Unt.) and RIE treated FEP. $\%\Delta m$ is the percentage weight loss relative to weight before RIE treatment. ER is an abbreviation for etch rate. Weight measurements for recipe A5 and D5 are missing. The diameter (d) refers to the diameter of the structures on the surface. The density (ρ) refers to the number of structures per square micro meter. Etched material is presented as percentage weight loss from the RIE treatment. Wetting properties are represented by calculated mean and standard deviation from five experiments by the tilted plate method, all with 70 µl drops of deionized water. *Films could not be rinsed short time in advance of the experiments. This is described in more detail in subsection 3.7.2 and 3.8.2. [1] $F_{\mathrm{pin}} = mg\ sin(\alpha_{\mathrm{c}})$ (details in subsection 2.4.1). [2] $F_{\mathrm{pin}} = w\gamma_{\mathrm{lv}}(cos(\theta_{\mathrm{a}}) - cos(\theta_{\mathrm{r}})$ (details in subsection 2.4.2).

Recipe	Unt.	A5	B5	C5	C10	C15	C20	D5	E5	C(1)5	C(2)5	C(3)5
$\%\Delta m$	-	-	7.7	4.8	15.3	22.6	24.2	-	7.7	5.5	6.8	4.2
ER [nm/min]	-	-	385	242	381	377	303	-	385	273	339	208
d [nm]	-	100 ± 40	100 ± 30	110 ± 20	100 ± 30	110 ± 30	110 ± 30	80 ± 20	-	100 ± 20	-	-
ρ [µm^{-2}]	-	63	68	55	30	35	27	74	-	33	-	-
α_{c} [°]	9 ± 1	44 ± 4	46 ± 4	62 ± 3	61 ± 4	56 ± 5	65 ± 5	60 ± 2	$47 \pm 9^*$	63 ± 11	$73 \pm 7^*$	$54 \pm 4^*$
θ_{a} [°]	118 ± 2	131 ± 1	127 ± 2	132 ± 3	133 ± 2	129 ± 7	144 ± 5	129 ± 1	$90 \pm 14^*$	136 ± 4	$126 \pm 5^*$	$93 \pm 2^*$
θ_{r} [°]	102 ± 2	51 ± 2	52 ± 8	19 ± 4	28 ± 5	24 ± 2	20 ± 7	17 ± 2	$13 \pm 5^*$	25 ± 11	$20 \pm 5^*$	$10 \pm 3^*$
$\Delta\theta$ [°]	16 ± 3	80 ± 3	75 ± 8	113 ± 5	105 ± 6	105 ± 8	124 ± 9	112 ± 3	$77 \pm 15^*$	111 ± 12	$106 \pm 7^*$	$84 \pm 4^*$
F_{pin} [µN][1]	110 ± 10	480 ± 30	490 ± 40	600 ± 20	600 ± 20	570 ± 30	620 ± 30	600 ± 10	$500 \pm 70^*$	610 ± 60	$660 \pm 20^*$	$560 \pm 30^*$
F_{pin} [µN][2]	114 ± 19	512 ± 18	485 ± 49	609 ± 46	556 ± 24	571 ± 48	658 ± 65	610 ± 23	$522 \pm 132^*$	565 ± 64	$595 \pm 33^*$	$490 \pm 38^*$

Chapter 4

Discussion

This chapter contains discussion of the results and some reflections on relating work found in the literature. First, the reproducibility of the RIE treatment will be addressed. Then, the resulting structures of the RIE treatment will be discussed. Further, the altered wetting properties resulting from the generated nano-structures will be addressed, followed by some reflections on the CA measurement methods used. Last, some suggestions for further work is presented.

4.1 Reproducibility of RIE treatment

It is an important issue, when trying to measure the properties of the FEP films, to achieve high reproducibility of both measurements, but also the sample fabrication. In subsection 3.9.1, it was shown that some of the etched FEP films got white spots during etching, resulting in deviating structures and wetting properties. During the work of this project, several small pieces of FEP (approximately 15x15 mm^2 and 30x20 mm^2) have been etched for each recipe. Sometimes an etch process of multiple FEP films did not result in enough transparent films needed for the CA measurements to be performed. Thus, additional FEP films had to be fabricated. Since the fabrication sometimes gave different results, the reproducibility and quality of the etch results is something that is important to investigate. Such a study would be even more important if fabrication of nano-structured FEP films were to be done on a large scale.

4.2 Structure morphology

The structure morphology resulting from RIE treatment, was highly dependant on the gas composition of the plasma. When the plasma consisted of oxygen and argon (recipe C), or only oxygen (recipe D), the shape of the resulting structures was looking like hairs or cones. If CF_4 was introduced to the gas composition (recipe A and B), the resulting structures were looking more like granules or spheres. However, it is important to note that the size of the structures are still comparable to the structures resulting from the oxygen and argon plasma. Yet another transition is seen when going from a plasma consisting of oxygen and argon to argon only. FEP etched by argon seem to have ditches or voids into the surface, instead of freestanding structures (hairs/cones) like seen when etching with oxygen and argon (or oxygen alone).

Structure height measurements was only done for FEP etched by recipe C5 and C10. The distribution of diameter and height are shown in figure 3.16c and 3.16d respectively. The structure dimensions for FEP etched by recipe C10 were, h = 530 $\pm$ 70 nm and d = 120 $\pm$ 30 nm, i.e. an aspect ratio of about 5. When Wohlfart et al. obtained structures on PET

with aspect ratio of about 3, their structures became mechanically unstable and started to collapse, forming bundles of structures [18]. No such collapsing of structures were seen for any of the FEP samples fabricated during the work of this thesis.

4.3 Strong adhesion of water drops to nano-structured FEP

Introducing surface roughness to polymer films, was expected to increase the contact angle (CA) and reduce surface-drop adhesion [7, 8, 9, 10]. Nevertheless, the resulting wetting properties of the nano-structured FEP fabricated in the work of this thesis, are quite different from these expectations. As expected, the ACA increases a bit (by 10 to 20°) for the nano-structured FEP. The adhesion of water drops to the surface (F_{pin}) on the other hand, increased by a factor of approximately 6. FEP etched by oxygen and argon for 20 minutes (recipe C20) exhibit adhesion of, $F_{\mathrm{pin}} = 620 \pm 30$ μN, almost as much as Law et al. achieved by mimicking the nano-structures of rose petal leaves on polymers, $F_{\mathrm{pin}} = 684 \pm 15$ μN [29].

According to the work by Schmidt et al., there is a relation between the CA hysteresis (CAH) of a surface, and the adhesion of the surface. A surface with greater CAH, also has greater adhesion. And a surface with lower CAH, also has lower adhesion [31]. The same observations where done for the FEP films tested in the work for this thesis (see figure 3.32).

In Ref. [36] both a smaller ROA and CAH has been obtained by introducing micro-structures in addition to nano-structures, thus mimicking the surface of the lotus leaf. Like mentioned above, the irregular areas with structures of different shape and size are of a greater order of magnitude than the granule looking structures like seen in figure 3.7f and the light areas in figure 3.8b. This means there are structures present in both the micro- and nano-range. Yet, it is different from those in Ref. [36] which has micro-scale structures with nano-scale structures on top, distributed in an ordered fashion. The micro-scale structures on sample A is distributed in a more random and irregular order.

4.4 Contact angle measurement methods

Contact angle measurements has been conducted by two methods: sessile drop (needle in) and tilted plate. Due to large CAH for the nano-structured FEP, quite big drops were needed for the sessile drop (needle in) method, according to Korhonen et al. [26]. Since parts of the etched FEP films could have some spots (section 4.1) with deviating structures and wetting properties, using small drops during CA measurements were more convenient than using big drops. Also, during CA measurements during injection and withdrawal of big volumes ($V > 100$ μl), the measurement software had some trouble making a contour around the edge of the drop. When the contour does not fit the drop edge correctly, this results in incorrect measurements of the CA and the volume.

Another aspect of the CA measurements by the sessile drop (needle in) method is time. To avoid instability of the advancing and receding motion of the drop on the surface, the dosage rate should be kept low. When big drop volumes are used, this method becomes quite time consuming. For instance, if 140 μl of water is to be injected and withdrawn from a drop at 0.5 μl/s, this takes more than 9 minutes, resulting in one measurement of the ACA and the RCA. At a dosage rate of 0.1 μl/s, the same volume would take 47 minutes to inject and withdraw. These measurements may potentially be very time consuming, unless

investigations of the dispensing rate can show that injection and withdrawal can be done at higher rates, without introducing instability and errors to the measurements.

For the nano-structured FEP fabricated for this work, the tilted plate method turned out to be a more convenient choice. It was possible to use smaller drops, yet not much smaller than 70 µl. During a test with different volumes on a nano-structured FEP (recipe C5, see table 2.3), drops as big as 50 µl was pinned to the surface all the way to 90° tilt angle, which is the maximum tilt for the OCA 20L. The measurement time from the drop was placed to the drop rolled off was approximately 10 minutes, depending on how steep inclination the drops would pin to the surface. If there is no need for CA measurements at regular intervals before the drop rolls off the surface (only one measurement at the tilt angle the drop starts to roll), this will further reduce the time of each experiment significantly.

Another advantage of the tilted plate method, is that a direct measure of the surface adhesion is obtained from the ROA. Through analysis of the gravitational force pulling on a droplet on a tilted plate, one can calculate the pinning force that has to be greater than the gravitational force as long as the drop is pinned to the sample (for details, see subsection 2.4.1). However, Furmidge has presented a relation between the pinning force and the ACA and RCA of a surface, which does not include the ROA. The pinning force calculated with Furmidge's equation (equation 2.14) agree quite well with the method using the ROA, which can be seen in figure 3.29.

4.5 Further work

During the work of this thesis, FEP with nano-structures of some different shapes and sizes has been fabricated and tested. However, the variety of shape and size could have been more diverse. If the size of the structures had varied by some orders of magnitude, and a bigger span in aspect ratio (height/width) had been obtained, a better understanding of the effect of the structure's size and shape on the surface's wetting properties could have been obtained. For FEP etched by the instrument used in this thesis, an oxygen and argon plasma (recipe C) exhibited a decent etch rate and anisotropy. Fang et al. proposed a method where polymers are coated by a layer of metal nanoparticles through sputter coating. The coating is done prior to the plasma treatment. By altering the thickness of the metal layer and the etch duration, the density and length of the resulting nanowires are controlled [37]. The method by Fang et al. could be combined with etching of FEP with recipe C (section 3.5), for improved control of size and shape of the resulting nano-structures.

Rubbing Teflon with sandpaper has been done in order to promote hydrophobic properties for the surface. The Teflon improved from $\theta_a = 128°$ and $\Delta\theta = 50°$ untreated, to $\theta_a = 150°$ and $\Delta\theta = 4°$ for the sandpaper roughness resulting in best combination of high ACA and low CAH [38]. Rubbing with sandpaper introduces roughness on the micro scale. For further work, combining treatment of a polymer with both sandpaper and RIE should be done. If roughness on the micro scale (sandpaper) and on the nano scale (RIE), so called hierarchical structures [36] are obtained, superhydrophobic properties might be achieved. Superhydrophobic surfaces exercise a CA of $\theta > 150°$ and low CAH allowing droplets to roll off the surface at only a slight tilt, just like the lotus leaf [29].

Chapter 5

Conclusion

The objective of this work was to create nano-structures of different geometries on the surface of FEP by means of reactive ion etching (RIE). During this work, it was desired to get a better understanding of how changing different etch parameters affect the geometry of the resulting structures, and furthermore how the morphology altered the wetting properties of the surface. In order to study the wetting properties, suitable measurement methods must be researched and developed.

The FEP has been treated by RIE using a range of different etch parameters. Three parameters have been altered: gas composition, chamber pressure and etch duration. The gases used during etching have been different compositions of O_2, Ar and CF_4. By changing the gas composition, it was found that the shape of the resulting structures could change significantly. By lowering the chamber pressure, the etch rate increased. When the etch duration was increased, the structure density was reduced, structure height increased, and the structure diameter remained unchanged.

The resulting nano-structures from different gas compositions can be divided into three groups regarding morphology. The first group of structures look like granules or spheres (recipe A and B). The second group of structures look more like hairs or cones (recipe C, D and C^1). The third group looks like there are holes or ditches into the surface (recipe E and C^3). The structures in the first and second group all had a diameter between 80 ± 20 nm and 110 ± 30 nm. Structure height was measured for FEP etched by oxygen and argon (recipe C) for 5 and 10 minutes, resulting in $h = 230 \pm 40$ nm and $h = 530 \pm 70$ nm respectively.

The wetting properties of FEP changed significantly after nano-structuring the surface. For untreated FEP, the advancing CA (ACA), CA hysteresis (CAH) and adhesion for water drops on the surface are $\theta_a = 118 \pm 2°$, $\Delta\theta = 16 \pm 3°$ and $F_{pin} = 110 \pm 10$ μN respectively. For nano-structured FEP, the same values have been measured to be as large as, $\theta_a = 144 \pm 5°$ (recipe C20), $\Delta\theta = 124 \pm 9°$ (recipe C20) and $F_{pin} = 660 \pm 20$ μN (recipe $C^2$5). When the FEP with structures looking like ditches (recipe E and C^3) are compared to the rest of the nano-structured FEP, the pinning force were about the same, and the CAH was a little lower. ACA had decreased compared to the untreated FEP, $\theta_a \approx 90°$.

To measure CAs on the nano-structured FEP, the tilted plate method was found to be superior to the other techniques used, providing higher reproducibility of CA measurements. The tilted plate method also provides information about the adhesive force through the critical roll off angle (ROA) at which the drop rolls off the surface. It should be noted that Furmidge has made a good estimate of the pinning force by means of the ACA and the receding CA [30]. Due to the measurement data available through the experimental setup used, some simplification of Furmidge's equation had to be done. Nevertheless, the calculated pinning force agreed quite well with the pinning force calculated from the ROA.

References

[1] Romain Guigon et al. "Harvesting raindrop energy: experimental study". In: *Smart Materials and Structures* 17.1 (2008), p. 015039. URL: http://stacks.iop.org/0964-1726/17/i=1/a=015039.

[2] Zong-Hong Lin et al. "Harvesting Water Drop Energy by a Sequential Contact-Electrification and Electrostatic-Induction Process". In: *Advanced Materials* 26.27 (2014), pp. 4690–4696. ISSN: 1521-4095. URL: http://dx.doi.org/10.1002/adma.201400373.

[3] Robert Ehrlich. *Renewable Energy: A First Course*. 1st ed. Boca Raton, New York, Abingdon: CRC Press, 2013. ISBN: 978-1-4398-6115-8.

[4] L.E. Helseth and H.Z. Wen. "Evaluation of the energy generation potential of rain cells". In: *Energy* 119.Supplement C (2017), pp. 472 –482. URL: http://www.sciencedirect.com/science/article/pii/S0360544216319028.

[5] A.F. Diaz and R.M. Felix-Navarro. "A semi-quantitative tribo-electric series for polymeric materials: the influence of chemical structure and properties". In: *Journal of Electrostatics* 62.4 (2004), pp. 277 –290. URL: http://www.sciencedirect.com/science/article/pii/S0304388604001287.

[6] Yajuan Sun et al. "Using the gravitational energy of water to generate power by separation of charge at interfaces". In: *Chem. Sci.* 6 (6 2015), pp. 3347–3353. URL: http://dx.doi.org/10.1039/C5SC00473J.

[7] L.E. Helseth and X.D. Guo. "Fluorinated ethylene propylene thin film for water droplet energy harvesting". In: *Renewable Energy* 99 (Dec. 2016), pp. 845–851. URL: http://dx.doi.org/10.1016/j.renene.2016.07.077.

[8] Yong Han Yeong and Mool C. Gupta. "Hot embossed micro-textured thin superhydrophobic Teflon {FEP} sheets for low ice adhesion". In: *Surface and Coatings Technology* 313 (2017), pp. 17 –23. URL: http://www.sciencedirect.com/science/article/pii/S0257897217300270.

[9] Elena Celia et al. "Recent advances in designing superhydrophobic surfaces". In: *Journal of Colloid and Interface Science* 402.Supplement C (2013), pp. 1 –18. URL: http://www.sciencedirect.com/science/article/pii/S0021979713002865.

[10] Masashi Miwa et al. "Effects of the Surface Roughness on Sliding Angles of Water Droplets on Superhydrophobic Surfaces". In: *Langmuir* 16 (Mar. 2000), pp. 5754–5760. URL: http://pubs.acs.org/doi/abs/10.1021/la991660o.

[11] Sangwha Lee et al. "The Wettability of Fluoropolymer Surfaces: Influence of Surface Dipoles". In: *Langmuir* 24.9 (2008), pp. 4817–4826. URL: http://dx.doi.org/10.1021/la700902h.

[12] DuPont. *DuPont™ Teflon® FEP: fluoroplastic film*. 2013. URL: http://docs-europe.electrocomponents.com/webdocs/065a/0900766b8065a8bd.pdf (visited on 09/07/2017).

[13] DuPont. *Teflon® FEP: fluoropolymer resin*. URL: http://www.rjchase.com/fep_handbook.pdf (visited on 09/08/2017).

[14] Francis F. Chen. *Introduction to plasma physics*. New York and London: Plenum Press, 2012. ISBN: 978-1-4757-0461-7.

[15] Kazuo Nojiri. "Mechanism of Dry Etching". In: *Dry Etching Technology for Semiconductors*. Switzerland: Springer International Publishing, 2015, pp. 11–30. ISBN: 978-3-319-10295-5.

[16] Marc J. Madou. "Pattern Transfer with Dry Etching Techniques". In: *Fundamentals of Microfabrication : The Science of Miniaturization*. 2nd ed. Boca Raton, London, New York, Washington D.C.: CRC Press LLC, 2002, pp. 79–121. ISBN: 0-8493-0826-7.

[17] "Temperature Effect on Reaction Rate". In: *Chemical Kinetics and Reaction Dynamics*. Dordrecht: Springer Netherlands, 2006, pp. 46–54. ISBN: 978-1-4020-4547-9. URL: https://doi.org/10.1007/978-1-4020-4547-9_2.

[18] Ellen Wohlfart et al. "Nanofibrillar Patterns on PET: The Influence of Plasma Parameters in Surface Morphology". In: *Plasma Processes and Polymers* 8.9 (June 2011), pp. 876–884. URL: http://dx.doi.org/10.1002/ppap.201000164.

[19] Joseph Goldstein et al. *Scanning Electron Microscopy and X-Ray Microanalysis*. 3rd ed. New York: Springer, 2003. ISBN: 978-0-306-47292-3.

[20] Ludwig Reimer. *Scanning Electron Microscopy: Physics of Image Formation and Microanalysis*. 2nd ed. Berlin Heidelberg: Springer, 1998. ISBN: 3-540-63976-4.

[21] R. Flatabø et al. "A systematic investigation of the charging effect in scanning electron microscopy for metal nanostructures on insulating substrates". In: *Journal of Microscopy* 265.3 (2017), pp. 287–297. URL: http://dx.doi.org/10.1111/jmi.12497.

[22] Wayne Rasband. *ImageJ*. 2017. URL: https://imagej.nih.gov/ij/index.html (visited on 09/04/2017).

[23] Yuehua Yuan and T. Randall Lee. "Contact Angle and Wetting Properties". In: *Surface Science Techniques*. Ed. by Gianangelo Bracco and Bodil Holst. Berlin Heidelberg: Springer, 2013, pp. 3–34. ISBN: 978-3-642-34243-1.

[24] Thomas Young. "An Essay on the Cohesion of Fluids". In: *Philosophical Transactions of the Royal Society of London* 95 (1805), pp. 65–87. URL: http://www.jstor.org/stable/107159.

[25] Jacob N. Israelachvili. *Intermolecular and Surface Forces*. 3rd ed. San Diego: Academic Press, 2011. ISBN: 978-0-12-391927-4.

[26] Juuso T. Korhonen et al. "Reliable Measurement of the Receding Contact Angle". In: *Langmuir* 29.12 (2013), pp. 3858–3863. URL: http://dx.doi.org/10.1021/la400009m.

[27] A.W Neumann et al. "An equation-of-state approach to determine surface tensions of low-energy solids from contact angles". In: *Journal of Colloid and Interface Science* 49.2 (1974), pp. 291 –304. URL: http://www.sciencedirect.com/science/article/pii/0021979774903658.

[28] G. Macdougall and C. Ockrent. "Surface energy relations in liquid/solid systems I. The adhesion of liquids to solids and a new method of determining the surface tension of liquids". In: *Proceedings of the Royal Society of London A: Mathematical, Physical and Engineering Sciences* 180.981 (1942), pp. 151–173. URL: http://rspa.royalsocietypublishing.org/content/180/981/151.

[29] Jaslyn Bee Khuan Law et al. "Bioinspired Ultrahigh Water Pinning Nanostructures". In: *Langmuir* 30.1 (2014), pp. 325–331. URL: http://dx.doi.org/10.1021/la4034996.

[30] C.G.L Furmidge. "Studies at phase interfaces. I. The sliding of liquid drops on solid surfaces and a theory for spray retention". In: *Journal of Colloid Science* 17.4 (1962), pp. 309 –324. URL: http://www.sciencedirect.com/science/article/pii/0095852262900119.

[31] Donald L. Schmidt et al. "Contact Angle Hysteresis, Adhesion, and Marine Biofouling". In: *Langmuir* 20.7 (2004), pp. 2830–2836. URL: http://dx.doi.org/10.1021/la035385o.

[32] L. E. Helseth and X. D. Guo. "Contact Electrification and Energy Harvesting Using Periodically Contacted and Squeezed Water Droplets". In: *Langmuir* 31.10 (Mar. 2015), pp. 3269–3276. URL: http://pubs.acs.org/doi/abs/10.1021/la503494c.

[33] Geon Hwee Kim et al. "Bioinspired Structural Colors Fabricated with ZnO Quasi-Ordered Nanostructures". In: *ACS Applied Materials & Interfaces* 9.22 (2017), pp. 19057–19062. URL: http://dx.doi.org/10.1021/acsami.6b15892.

[34] Kiyoshi Miyamoto and Akinori Kosaku. "Cuticular Microstructures and Their Relationship to Structural Color in the Shieldbug Poecilocoris Iewisi Distant". In: *Forma* 17 (2002), pp. 155–167. URL: http://www.scipress.org/journals/forma/pdf/1702/17020155.pdf.

[35] Masashi Miwa et al. "Effects of the Surface Roughness on Sliding Angles of Water Droplets on Superhydrophobic Surfaces". In: *Langmuir* 16.13 (2000), pp. 5754–5760. URL: http://dx.doi.org/10.1021/la991660o.

[36] Kerstin Koch et al. "Fabrication of artificial Lotus leaves and significance of hierarchical structure for superhydrophobicity and low adhesion". In: *Soft Matter* 5 (7 2009), pp. 1386–1393. URL: http://dx.doi.org/10.1039/B818940D.

[37] Hao Fang et al. "Controlled Growth of Aligned Polymer Nanowires". In: *The Journal of Physical Chemistry C* 113.38 (Sept. 2009), pp. 16571–16574. URL: http://dx.doi.org/10.1021/jp907072z.

[38] Michael A Nilsson et al. "A novel and inexpensive technique for creating superhydrophobic surfaces using Teflon and sandpaper". In: *Journal of Physics D: Applied Physics* 43.4 (2010), p. 045301. URL: http://stacks.iop.org/0022-3727/43/i=4/a=045301.

[39] Arvid Erdal. *Elementær innføring i sannsynlighetsregning og problemløsninger ved analyse av måleresultater*. Bergen: Alma Mater, 1997. ISBN: 82-419-0229-8.

[40] John P. Bentley. *Principles of Measurement Systems*. 4th ed. Harlow: Pearson, 2005. ISBN: 0-13-043028-5.

[41] WolframAlpha. URL: http://www.wolframalpha.com/input/?i=gravitation+in+bergen,+norway (visited on 09/13/2017).

Appendix A

Estimating measurement uncertainty

When performing measurements, one needs to be aware of uncertainties associated with the results of the measurement. Uncertainties may be introduced through the method of measurement, a_M, and through the physical property being measured, a_E. The total uncertainty of the measured value is given by [39]

$$a_T = \sqrt{a_E^2 + a_M^2} \tag{A.1}$$

If one of the to kinds of uncertainty is much greater than the other, the least one's contribution to the total uncertainty will be negligible. I.e. if $a_E \ll a_M$

$$a_T = a_M \tag{A.2}$$

To estimate the uncertainty related to a property being measured, multiple measurements should be done to reduce errors from each measurements. In a set of measurements of the same property, the mean value is given by

$$\bar{x} = \frac{1}{N}\sum_{i=1}^{N} x_i \tag{A.3}$$

From the same set of measurements, an approximation of the standard deviation may be calculated as a measure of the uncertainty

$$s = \sqrt{\frac{1}{1-N}\sum_{i=1}^{N}(x_i - \bar{x})^2} \tag{A.4}$$

In certain situations, this term is not so convenient to use. A simpler estimate of the uncertainty has proven to be adequate in many situations, even though it requires relatively few measurements. It is named the "max-min" estimate as it uses only the greatest and smallest value to estimate the uncertainty. For a set of $3 \leq N \leq 11$, the uncertainty can be expressed as

$$s \approx \frac{x_{max} - x_{min}}{\sqrt{N}} \tag{A.5}$$

This estimation requires a Gaussian distribution. But even for a distribution deviating a bit from a Gaussian distribution, this estimate gives a decent estimate of the uncertainty [39].

When dealing with a function of multiple quantities, each with an individual uncertainty, the uncertainty of the function may be found by error propagation. For a function,

$f(x, y)$, x and y with uncertainty s_x and s_y. The uncertainty of the function will be [40]:

$$s_{f(x,y)} = \sqrt{\left(\frac{\partial f(x,y)}{\partial x} s_x\right)^2 + \left(\frac{\partial f(x,y)}{\partial y} s_y\right)^2} \tag{A.6}$$

A.1 Example: Error propagation for the pinning force

The background of the pinning force (F_{pin}) is found in section 2.4.

Given the expression in equation A.7, all three parameters (m, g and α) included in the expression contribute to the error of F_{pin}.

$$F_{\text{pin}} = -mg\ sin(\alpha_{\text{c}}) \tag{A.7}$$

ROA measurements of a FEP etched by recipe C5 will be used as an example (table A.1). The origin of m is found in appendix C. g in Bergen (the place where the experiments were conducted) is according to Ref. [41], g = 9.82541 m/s^2. As g is presented with 5 decimal digits, an assumption was made that the uncertainty of g must be lower than 10^{-4} m/s^2. To avoid operating with an uncertainty too small, 10^{-4} is used for the calculations below.

TABLE A.1: Parameters used for calculation of $s_{F_{\text{pin}}}$.

α_{c}	$62 \pm 3°$ (1.07 ± 0.05 rad)
m	69.9 ± 0.3 mg
g	9.82541 ± 0.0001 m/s^2

The uncertainty of F_{pin} is calculated by error propagation:

$$s_{F_{pin}} = \sqrt{\left(\frac{\partial F_{pin}}{\partial m} s_m\right)^2 + \left(\frac{\partial F_{pin}}{\partial g} s_g\right)^2 + \left(\frac{\partial F_{pin}}{\partial \alpha_{\text{c}}} s_{\alpha_{\text{c}}}\right)^2} \tag{A.8}$$

$$s_{F_{pin}} = \sqrt{\left(g\ sin(\alpha_{\text{c}}) s_m\right)^2 + \left(m\ sin(\alpha_{\text{c}}) s_g\right)^2 + \left(mg\ cos(\alpha_{\text{c}}) s_{\alpha_{\text{c}}}\right)^2} \tag{A.9}$$

No information about the uncertainty of the tilting unit is provided by DataPhysics. It is assumed that it is less than the standard deviation of α_{c} ($4°$ for this case, the smallest for any sample is $1°$). The standard deviation is therefore used as the uncertainty of ROA when calculating $s_{F_{pin}}$. α_{c} is used in radians to avoid trouble with the units. Each term inside the root of equation A.9, is calculated separately in equation A.10, A.11 and A.12, then put into equation A.13.

$$\begin{aligned}\left(g\ sin(\alpha_{\text{c}}) s_m\right)^2 &= \left(9.82541\ \text{m/s}^2\ sin(1.07)\ 0.0000003\ \text{kg}\right)^2 \\ &= 6.646 \cdot 10^{-12} (\text{kg} \cdot \text{m/s}^2)^2\end{aligned} \tag{A.10}$$

$$\begin{aligned}\left(m\ sin(\alpha_{\text{c}}) s_g\right)^2 &= \left(0.000069\ \text{kg}\ sin(1.07)\ 10^{-4}\ \text{m/s}^2\right)^2 \\ &= 3.642 \cdot 10^{-17} (\text{kg} \cdot \text{m/s}^2)^2\end{aligned} \tag{A.11}$$

$$\begin{aligned}\left(mg\ cos(\alpha_c)s_{\alpha_c}\right)^2 &= \left(0.000069\ \mathrm{kg}\ 9.82541\ \mathrm{m/s^2}\ cos(1.07)\ 0.05\right)^2 \\ &= 2.649 \cdot 10^{-10}(\mathrm{kg \cdot m/s^2})^2\end{aligned} \tag{A.12}$$

$$\begin{aligned}s_{F_{pin}} &\approx \sqrt{(6.646 \cdot 10^{-12} + 3.642 \cdot 10^{-17} + 2.649 \cdot 10^{-10})(\mathrm{kg \cdot m/s^2})^2} \\ &\approx 20\ \mu\mathrm{N}\end{aligned} \tag{A.13}$$

Appendix B

SCA20 setup and functionality

The software (SCA20) supplied by DataPhysics to control the OCA 20L instrument is rather complex with many options, thus the operator should have some basic knowledge about the software. The setup used for the experiments by the tilted plate method will be explained in the following paragraphs.

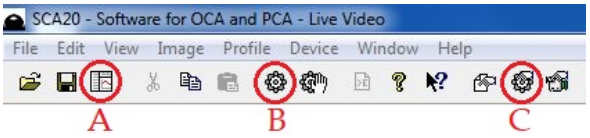

FIGURE B.1: Menu buttons in SCA20. Open Result window (A), open device controls (B) and open device preferences (C).

By clicking *Device preferences* (C in figure B.1), one can chose what syringe is used in the experiment. For all experiments conducted in this work, a B. Braun 1 ml disposable syringe is used. This is supplied by DataPhysics. This way, the dispenser unit knows how much water the syringe contains relating to the position of the plunger. This information is also essential in order to inject/withdraw the amount of water one intends to. The accuracy of the dispenser unit has been measured, the interested reader is referred to appendix C.

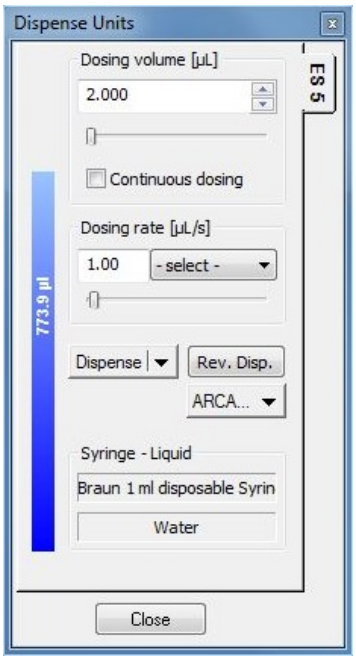

FIGURE B.2: Dispense unit control in SCA20.

The controls needed for the experiments are opened by first clicking *Device controls* (B in figure B.1). The controls of interest are *Dispense units* and *TBU90e* (tilt motor). The functionality of the controls are addressed after the preliminary setup.

By clicking *Dispense units*, a control window opens as seen in figure B.2. For the sessile drop (needle in) method, the *ARCA* function is preferable. This way one can set a series of actions by the dispenser unit, injected volume, withdrawn volume, a pause between injection and withdrawal if desired, and how many times these steps should be repeated. For the tilted plate, the main dispense unit window is sufficient, where simply one drop is to be dispensed on the sample surface. A dosing rate of 0.5 µl/s seemed suitable for relatively large drops (70 µl), and was used for all experiments. More details on the choice of drop volume is found in subsection 2.4.1.

A *Live video window* is open when the software is started. The live video window during a sessile drop (needle in) experiment is shown in figure B.3. In the upper left corner (A), a drop down menu lets the operator select what kind of measurement is supposed to be done. During *Sessile drop (needle in)*, four horizontal lines are present in the image. Between line 1 and 2, the software is expecting to see the needle. The drop is to be found below line 3, and the drop baseline is at line 4. All the lines are adjustable in height, and should be positioned to comply with the expectations just mentioned. By clicking *Start Recording* (B in figure B.3), the software starts recording the drop, which can be played and analyzed afterwards. *Calculation* (C in figure B.3) executes one *CA* measurement. *Magnification* (D in figure B.3) manually sets the magnification of the image (pixels/mm). Before doing this, it is important to enter the diameter of the needle in the *Result* window, in the *M-Info* tab. By pressing *Tracking* (E in figure B.3), continuous measurements are started.

If *Sessile drop* is chosen in the drop down menu (A in *Live Video* window), there are only two horizontal lines. The lower one should be at the baseline of the drop, while the other one should be above the top of the drop, and below other objects in the image, e.g. the tip of the needle. Now, the software is not expecting a needle in it's measurement area, and setting the magnification of the image should be done prior to the experiment. This is done by placing the two lines such that the needle is crossing both lines, and pushing *Magnification*. As the button is pushed, the magnification, *Mag [pixel/mm]*, in the result window in the *M-Info* tab will update (default is 100.000). Afterwards, the lines are placed at their correct positions.

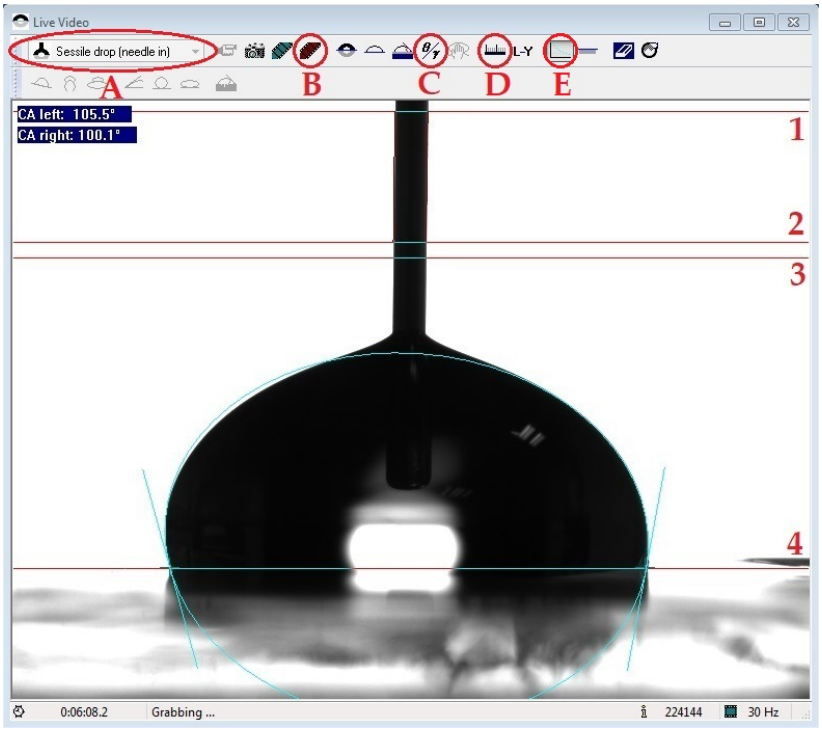

FIGURE B.3: *Live Video* window in SCA20. In the drop down menu (A), the kind of experiment is selected. Important buttons are *Start Recording* (B), *Calculation* (C), *Magnification* (D) and *Tracking* (E). Between line 1 and 2, only the needle should be present. Between line 3 and 4, only the drop should be present, while line 4 is placed on the baseline of the drop.

Some parameters depend on the instrument being calibrated correctly. When the drop

base diameter and drop volume is estimated, the shape and size of the drop in the live video image is analyzed by the software. To know what physical distance a number of pixels correspond to, one need to enter the outer diameter of the syringe needle. The outer diameter of the syringe needle was measured to be d = 0.505 mm (details on this estimate is found in appendix C). In the result window, the diameter was enter into *Ref. - Size [mm]* in the *M-Info*-tab, where the default value is 2.0000.

When the needle diameter i entered, the calibration can be done. To do this, the needle must cross line 1 and 2 (for *Sessile drop (needle in)*, see figure B.3). When *Sessile drop* is selected, there are only two horizontal lines, these must be positioned like line 1 and 2 for *Sessile drop (needle in)*. Now, *Magnification* (D in figure B.3) can be clicked, updating the *Mag* field in the *M-Info* tab in the result window. This is done automatically when using *Sessile drop (needle in)* from the drop down menu in the *Live Video* window (A in figure B.3).

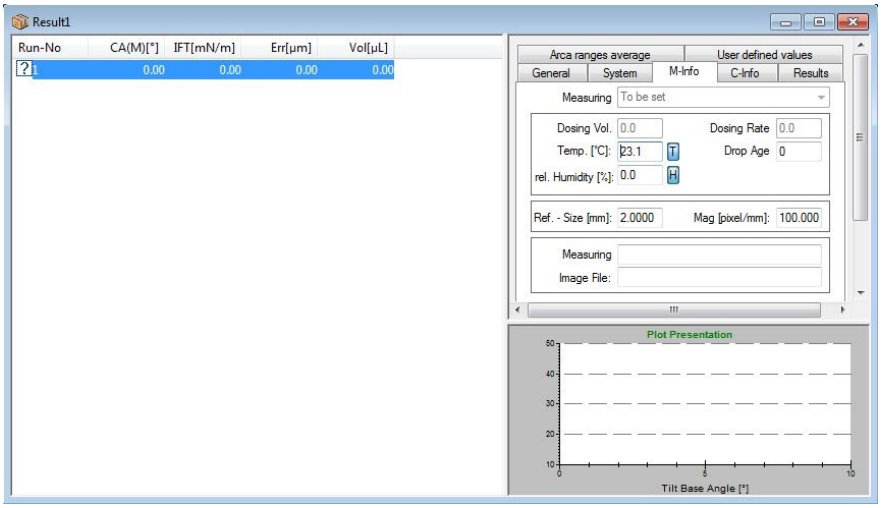

FIGURE B.4: Result window in SCA20. Magnification of the image can be set in the *M-Info* tab, and is crucial for volume estimates among other parameters.

To be able to store the measurements performed, a *Result* window like the one in figure B.4 must be opened. This is done by clicking the *Open result window* (A in figure B.1). To change the parameters to display, right click in the area where the parameters are displayed, and click *Options*. In the tab, *Display Columns* and *Export Columns*, there is a list of parameters that can be displayed. For the tilted plate method, there are especially three parameters of interest: left *CA*, right *CA* and the tilt angle. When doing the sessile drop (needle in) method, the following parameters were used: drop age, mean *CA*, drop base diameter and drop volume.

The *C-Info* tab in the *Result* window lets one select what algorithm to be used to estimate the contact angle. The methods that seemed most convenient for the measurements done for this thesis is *Ellipse Fitting* and *Polynom Fitting*. As the drop is laying on a flat surface, it is relatively symmetrical, and *Ellipse Fitting* works well as the drop has an elliptical shape. When the tilted plate method is used, the drop shape is no longer symmetrical, and *Polynom Fitting* seemed like a better choice. Generally, the *Polynom Fitting* gives a bit larger *CA* (in the range 5-10°) than the *Ellipse Fitting*, thus *CA* measurements estimated by two different methods should be avoided.

Appendix C

Accuracy of dispenser unit on DataPhysics OCA 20L

The instrument (OCA 20L by DataPhysics) used for contact angle (CA) measurements has a motorized dispensing unit. The accuracy of the drop volume dispensed was investigated by measuring the weight of twenty drops. This was done by dispensing 70 µl of deionized water (same as used in the CA experiments) on a plastic boat, the boat was then placed on a scale and weighted. The scale was an ABT 220-4M produced by Kern. It has a reproducibility of 0.1 mg and a weighing range of 10 mg to 220 g. The weight of the boat was 801.5 $\pm$ 0.1 mg, which was tared (scale with empty boat showed 0.0 mg). 20 water drops of 70 µl was weighted, the results are displayed in table C.1. Calculated mean drop weight with standard deviation was, $\bar{m}$ = 69.9 $\pm$ 0.3 mg (by equation A.3 and A.4 respectively).

TABLE C.1: Weight measurements of 20 drops dispensed by a dispenser unit on an OCA 20L produced by DataPhysics. An ABT 220-4M scale produced by Kern is used to measure the weight of the drops. It has a reproducibility of 0.1 mg.

n	m [mg]	n	m [mg]
1	69.3	11	69.2
2	70.3	12	70.1
3	70.2	13	70.1
4	70.2	14	69.9
5	70.4	15	69.8
6	70.2	16	69.7
7	69.7	17	69.8
8	69.9	18	69.8
9	69.6	19	70.1
10	69.8	20	70.0

Appendix D

Syringe needle diameter

The syringe and needle used are provided by DataPhysics, and produced by Nordson EFD. According to the needle container label, the outer diameter should be d_o = 0.51 mm, and the inner diameter, d_i = 0.525 mm. The name of the needles are *SNS-D 051/025*, which might indicate that the inner diameter should have been 0.025 mm, not 0.525 mm, like seen on the container label in figure D.1. The outer diameter was measured to make sure the correct diameter was used for calibrating the instrument.

FIGURE D.1: Syringe needle container.

D.1 Measurements by vernier caliper

The outer diameter of the needle was measured with a vernier caliper with 0.05 mm resolution. Ten measurements of the syringe needle (at different places) was done. Calculating mean and standard deviation by equation A.3 and A.4 respectively gives, $\bar{d}$ = 0.49 $\pm$ 0.02 mm. Since the standard deviation is less than the resolution of the vernier caliper, the resolution is used as error, $\bar{d}$ = 0.49 $\pm$ 0.05 mm.

TABLE D.1: Measurements of the needle diameter. A vernier caliper was used with resolution of 0.05 mm.

n	d [mm]	n	d [mm]
1	0.50	6	0.45
2	0.50	7	0.50
3	0.50	8	0.50
4	0.45	9	0.50
5	0.50	10	0.50

D.2 Measurements by micrometer

Prior to *CA* measurements by the tilted plate method, a syringe and needle was replaced by a new one. The outer diameter of the needle was measured with a micrometer with 0.005 mm resolution. First, the micrometer was tightened, showing 0.005 mm. Afterwards, ten measurements of the syringe needle (at different places) was done, all ten measurements was, d = 0.505 mm after the offset was subtracted. In this case, the resolution of the micrometer is the most significant source of error, thus d = 0.505 $\pm$ 0.005 mm.

Appendix E

Measurements in ImageJ

Diameter and height of structures has been measured in ImageJ for some samples. Images with measurement lines drawn are shown in the figure E.1-E.4. The length of each line in the images are saved to file, afterwards the values are used for making histograms of size distribution (like in figure 3.16c and 3.16d) and calculation of mean and standard deviation from equation A.3 and A.4.

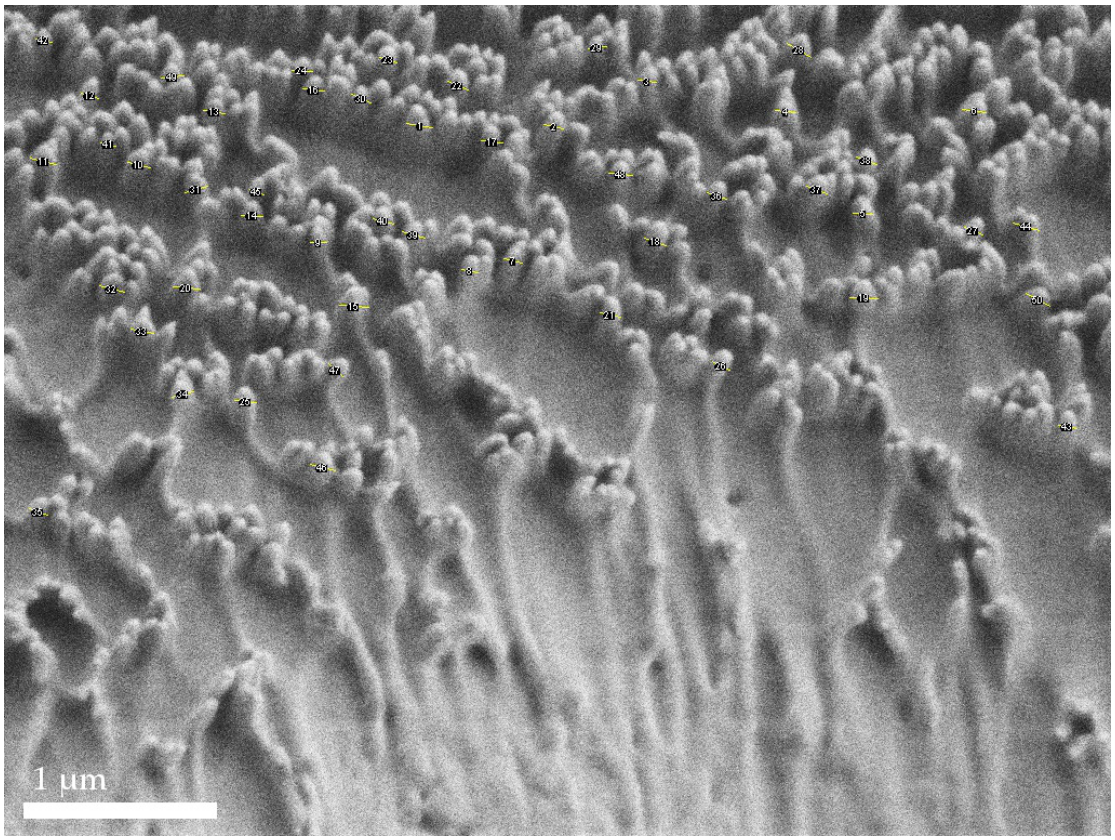

FIGURE E.1: Diameter measurements of 50 structures on C5 sample.

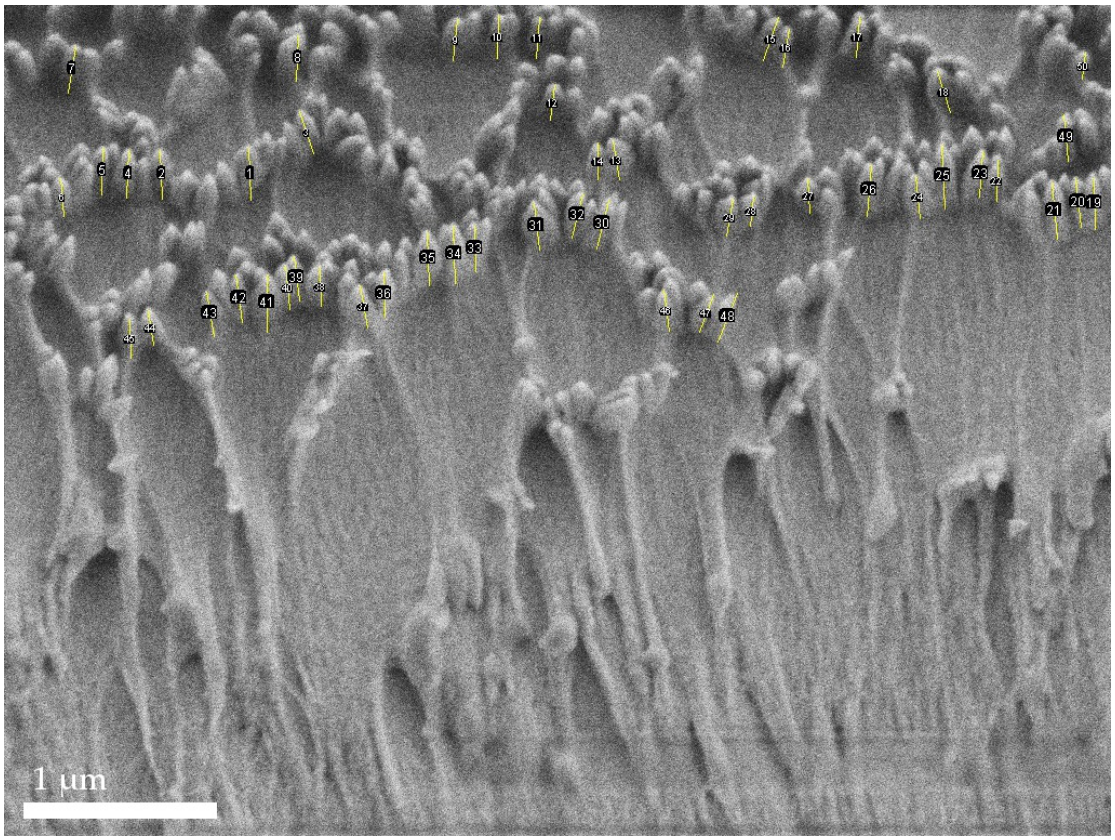

FIGURE E.2: Height measurements of 50 structures on C5 sample.

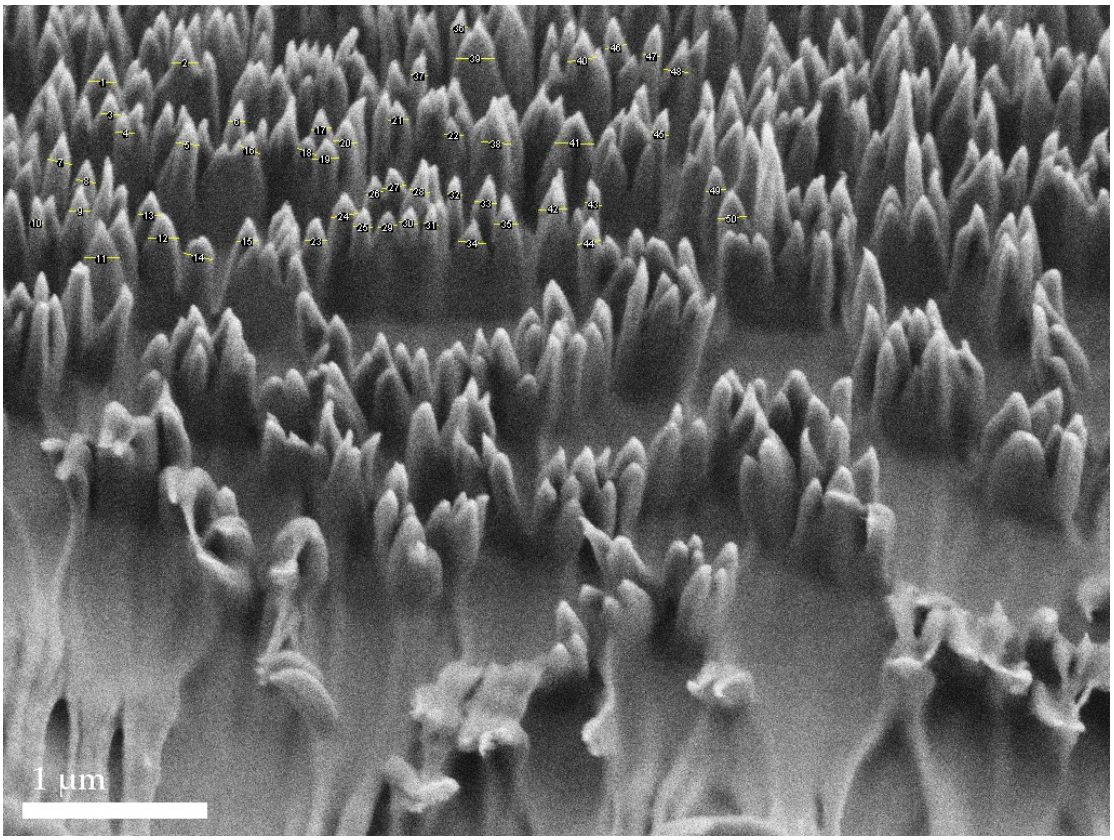

FIGURE E.3: Diameter measurements of 50 structures on C10 sample.

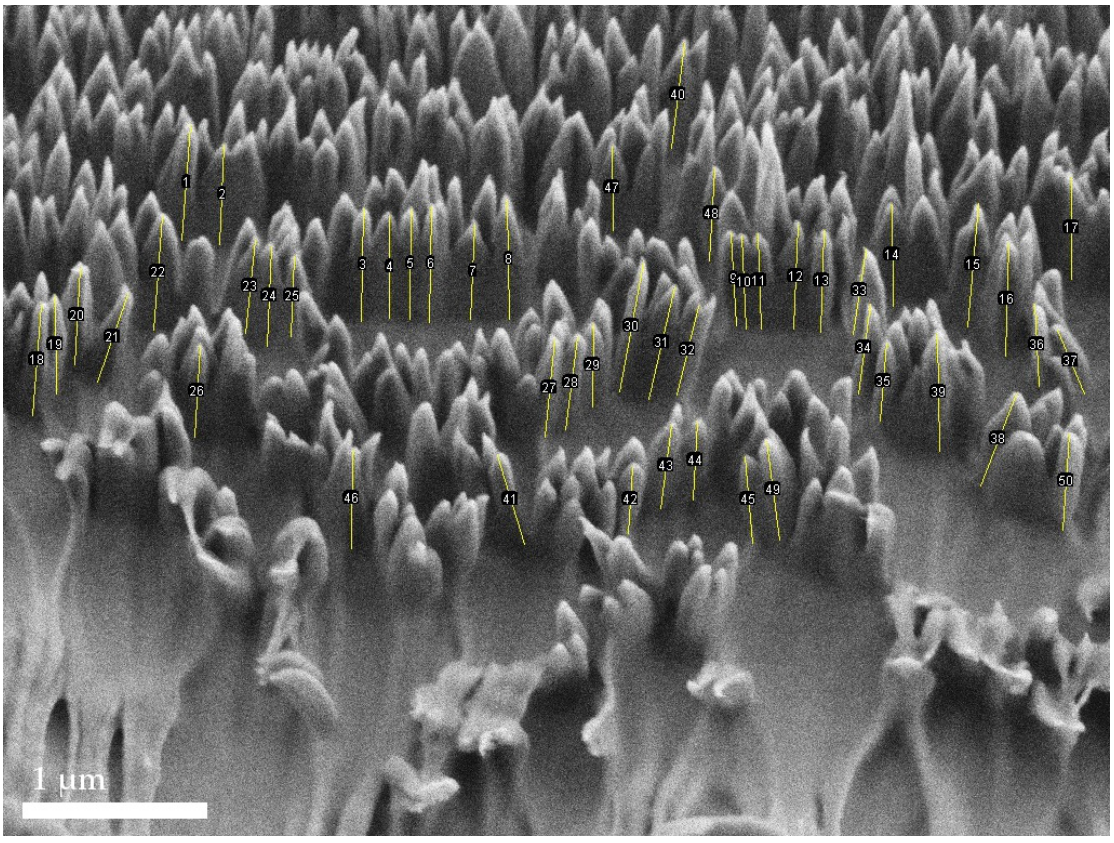

FIGURE E.4: Height measurements of 50 structures on C10 sample.

Appendix F

Supplementary SEM images

This appendix contains supplementary SEM images. Figure F.1 are SEM images of recipe G and H, which are not included in chapter 3. Some structures deviating from the general appearance of the FEP films after RIE treatment is shown in figure F.2-F.4.

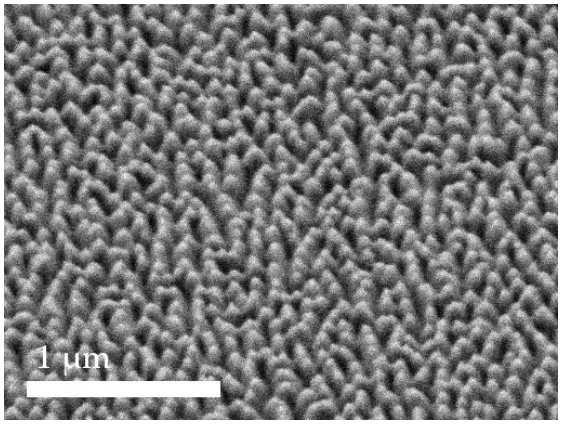

(a) Recipe G5.

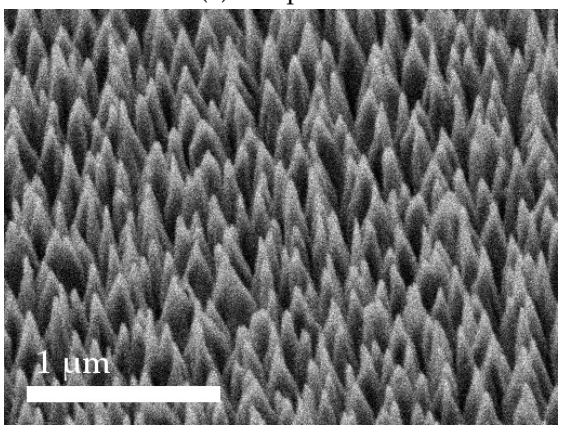

(b) Recipe H5.

FIGURE F.1: SEM images captured at 45°.

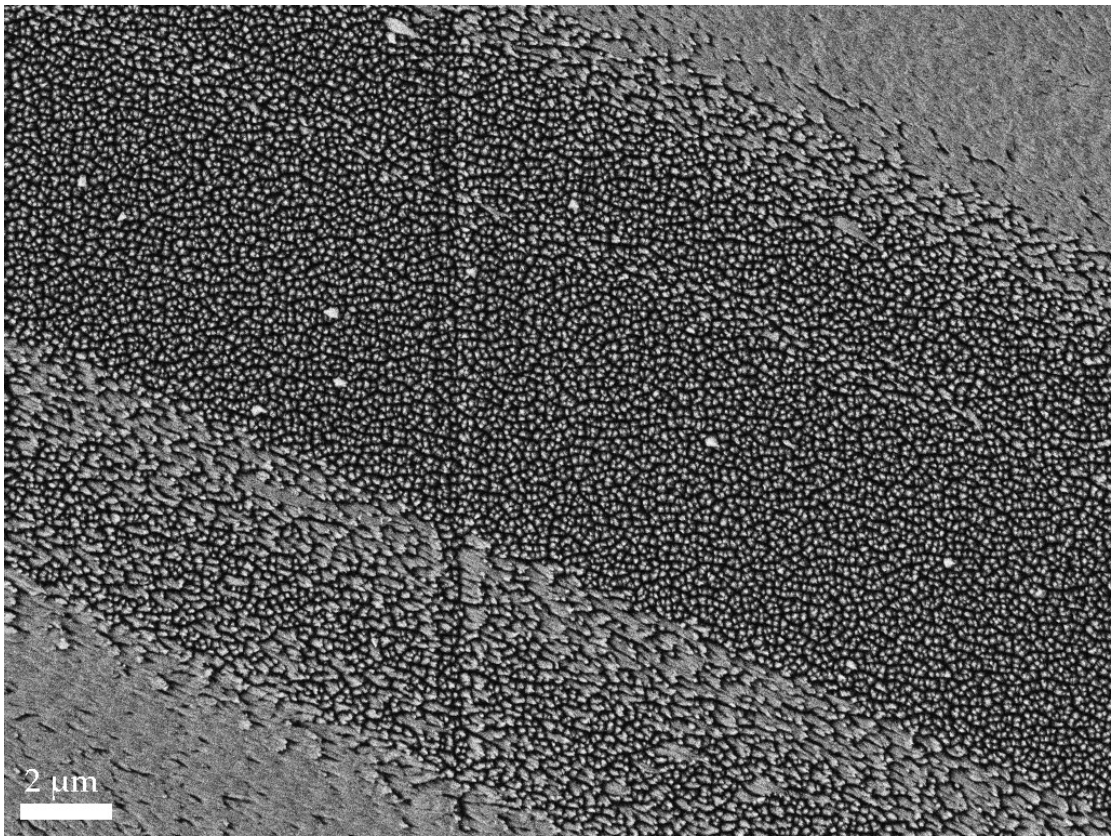

FIGURE F.2: Deviating structures on C15 sample imaged by SEM.

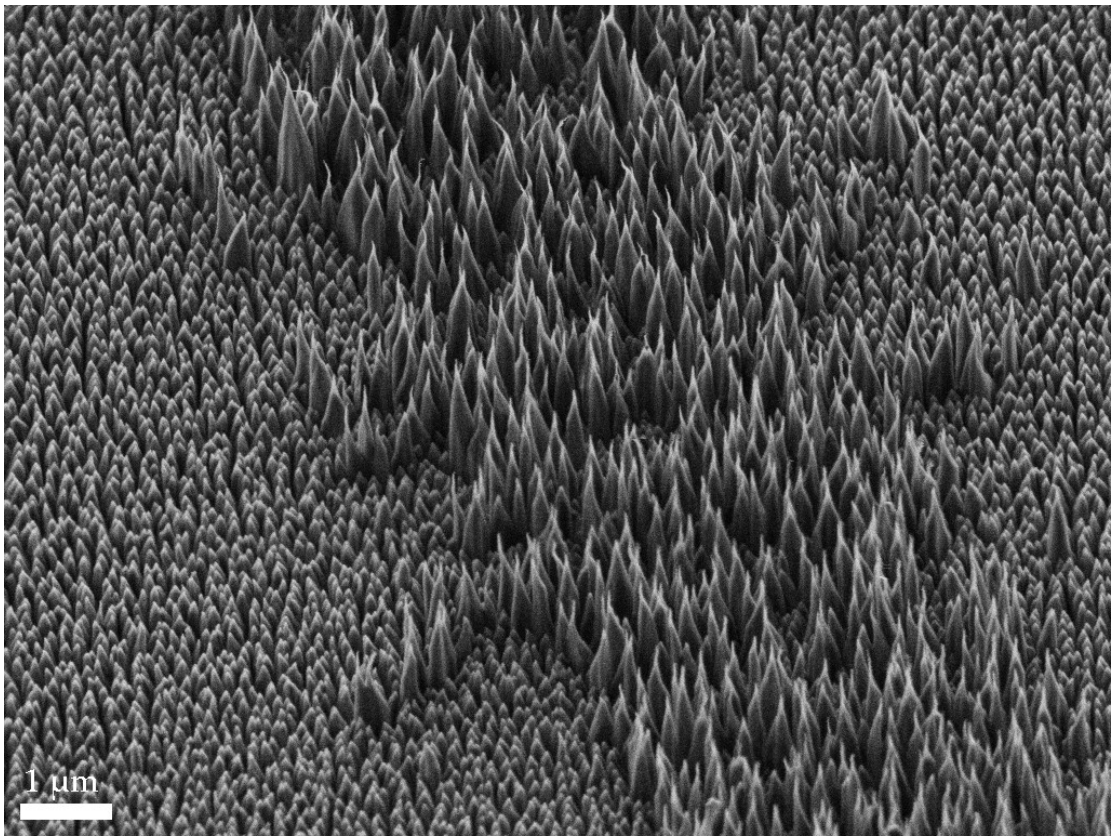

FIGURE F.3: Deviating structures on C15 sample imaged by SEM at 45 °.

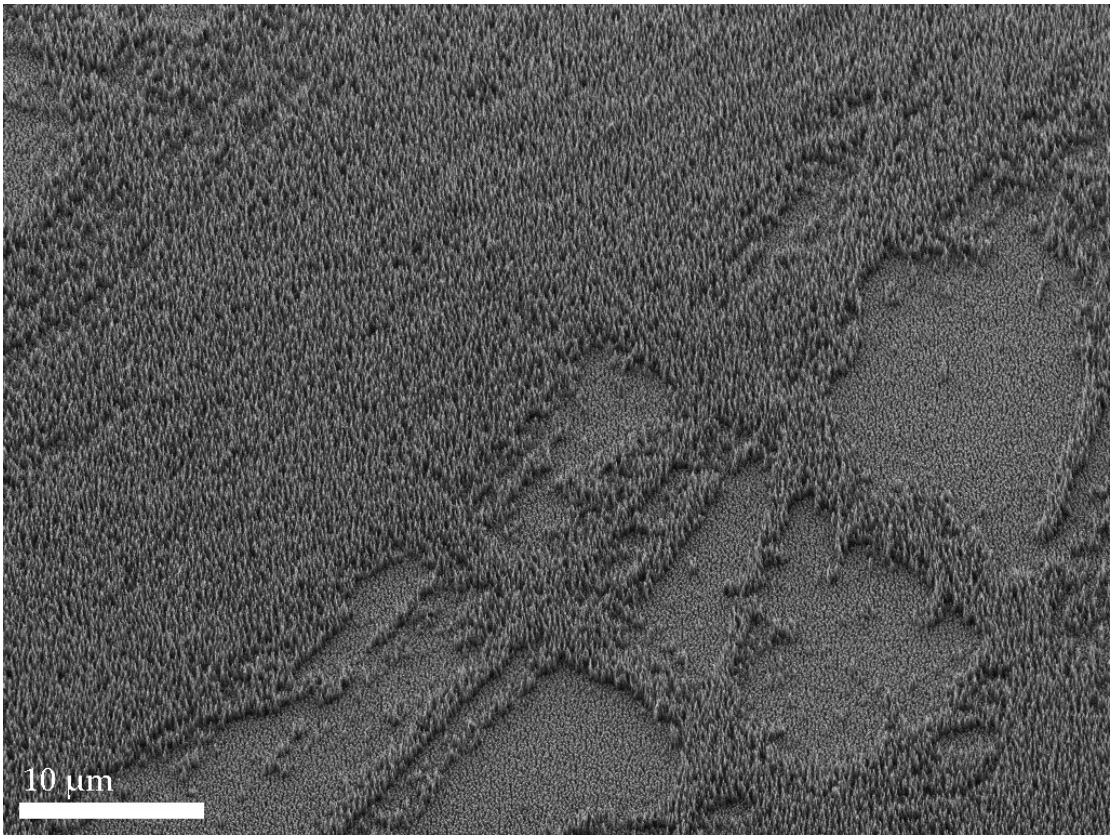

FIGURE F.4: Deviating structures on C15 sample imaged by SEM at 45 °.

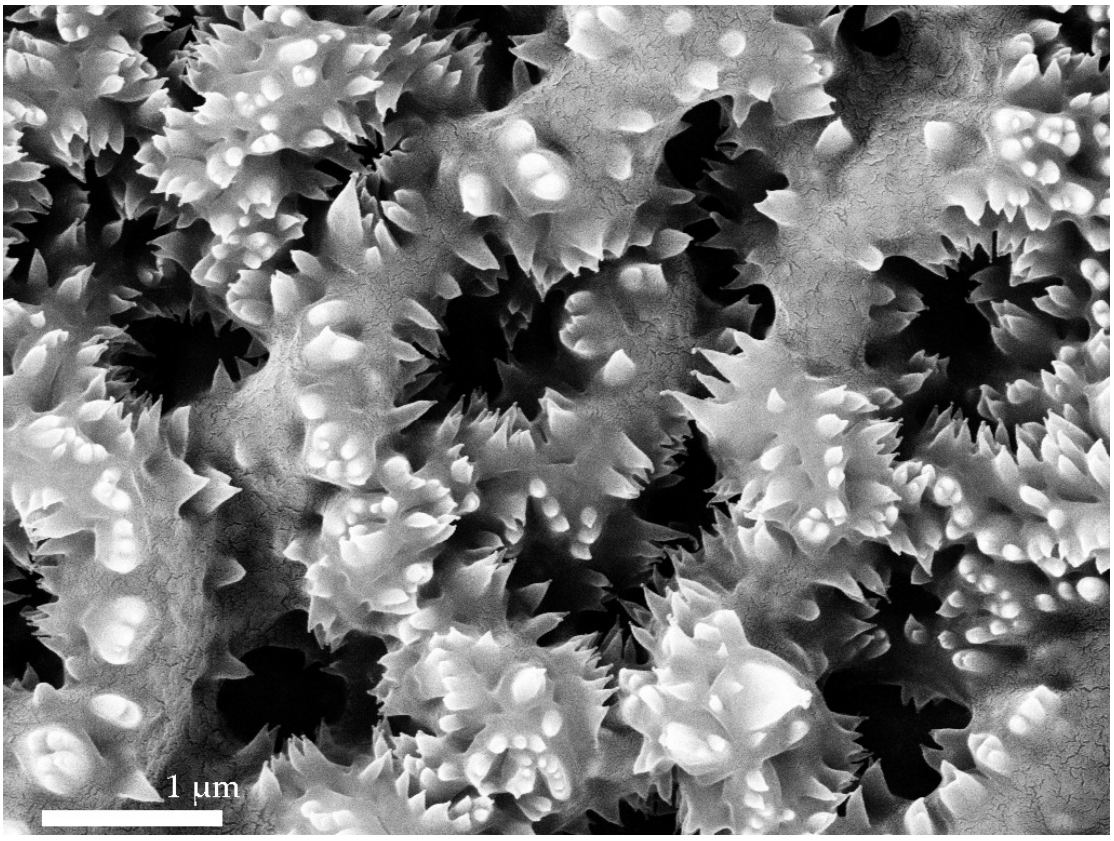

FIGURE F.5: SEM image of FEP etched by recipe A3. The sample was sputter coated by Au and Pd before it was imaged.